Master's thesis

NTNU
Norwegian University of Science and Technology
Faculty of Natural Sciences
Department of Chemistry

Erik Pieter de Vries

Understanding the effect of porosity and presence of silver in Cu:SAPO-34 as an HC-SCR catalyst, using propene or isobutane in a wet feed

Master's thesis in MLREAL
Supervisor: Karina Mathisen
Co-Supervisor: Guro Sørli
June 2019

NTNU
Norwegian University of
Science and Technology

Erik Pieter de Vries

Understanding the effect of porosity and presence of silver in Cu:SAPO-34 as an HC-SCR catalyst, using propene or isobutane in a wet feed

Master's thesis in MLREAL
Supervisor: Karina Mathisen
Co-Supervisor: Guro Sørli
June 2019

Norwegian University of Science and Technology
Faculty of Natural Sciences
Department of Chemistry

NTNU
Norwegian University of
Science and Technology

Acknowledgements

This master thesis was written at the department of chemistry (IKJ) at the Norwegian University of Science and Technology (NTNU). Sasol North America is acknowledged for providing the structural chemistry lab with free pseudo boehmite used for synthesis of the main material of this thesis.

Writing a master thesis has been one of the most challenging things I have done in my life. It has been an interesting journey, and one I could not have completed without the help from my supervisors. I would first like to thank my supervisor Vice Dean Dr. Karina Mathisen, for her guidance, help, feedback and not in the least patience with me through this difficult and busy last year of my education. Your support, insight, passion and ability to always make your students see new angles to approach their research, and always pushing them on to improve themselves, is truly inspiring. As a person who is about to step into the shoes of a teacher himself, you have been and are an important role model. Thank you!

I also want to thank my co-supervisor and good friend Phd. candidate Guro Sørli. In my endless stream of worries and uncertainties, not just this last year, but the last half of my education, you have been a rock I could always rely on. Thank you for all the good talks we have had, and for always cheering me up and pushing me on in the right direction when I needed it, because that happened often. Thank you for the countless feedback you have given me and for always being patient with me through my slow learning process. You have been a source of inspiration and motivation for me, and someone I really look up to.

I want to thank Phd. candidate Daniel Ali for providing me with the SEM images of my two main samples used in this thesis. Thank you for the good talks and advice during our job as assistants this autumn and during this last semester.

Thanks also goes to Msc. candidate Sigurd Botten and Phd. candidate Guro Sørli for their work in making a model for the bypass value of the NO_x instrumental setup. To all the other members of the structural chemistry group, thank you for your help in showing me around in the lab, good advice and fun times with fun music during lab work! It made the long hours all the better!

Last, but absolutely not least, I would like to thank my family in Norway and the Netherlands for always being there for me. My parents for their unending support, believing in me and always reminding me that there are other things in life than work and studies. I would like to

thank my brothers, Arild and Niels for always being patient with me, teasing me and goofing around with me whenever we were together. It really lifted my spirits and motivation, and I know I have not been the easiest person to deal with at times. Thanks also goes to my friends Espen Johnsen, Lisa Leganger Landfald. Elisabeth Sveen and May Britt Rian for the many fun and hard-working moments we have had during our time at NTNU.

Trondheim, June 2019

Erik Pieter de Vries

Abstract

The effect of porosity and presence of silver in Cu:SAPO-34 as an HC-SCR of NO_x catalyst was investigated, using propene and isobutane as hydrocarbons in a wet feed. Own conventional and hierarchical SAPO-34 samples were synthesized, varying different factors during mixing of the synthesis gel and crystallisation. The phase pure samples were ion exchanged with Ag^+ and Cu^{2+} separately and simultaneously, 4 times for each sample. Mechanically mixed samples were prepared using equal amounts of Ag^+ and Cu^{2+} samples. The phase purity and crystallinity were characterized by XRD and porosity by BET surface analysis before and after ion exchange. The metal content inside the samples was determined by ICP-MS, with an increase from 1 round to 4 rounds of ion exchange. The NO_x conversion of the samples was measured by a chemiluminescence NO_x analyser, after the first and fourth round of ion exchange.

Cu:SAPO-34 samples were active for both the conventional and hierarchical samples, while Ag:SAPO-34 samples were inactive. Simultaneously exchanged AgCu:SAPO-34 samples showed lower activity than their Cu:SAPO-34 counterparts, but with much lower copper content, suggesting a synergistic effect with silver. All of these had an increase in NO_x conversion after 3 additional rounds of ion exchange. The mechanically mixed silver and copper samples were only run for the silver and copper samples after 4 rounds of ion exchange, showing higher maximum NO_x conversion than the copper samples. This was not over an as wide temperature range, but with half the amount of copper present suggesting a synergistic effect with silver here as well. The highest obtained conversion of NO_x was obtained by the conventional mechanically mixed sample with 60 % at 500 °C.

Metal content seemed to have a bigger effect on the NO_x conversion than the porosity of the samples, as there was increase in conversion despite the gradual loss in porosity of the samples after 4 rounds of ion exchange. Porosity was however important for the mechanically mixed samples. No activity was obtained using isobutane, suggesting low concentration of active sites present inside the possible mesopores of the hierarchical sample and the external surface of both the hierarchical and conventional samples.

Sammendrag

Effekten av porøsitet og sølv i Cu:SAPO-34 som en HC-SCR av NO_x katalysator ble undersøkt, ved bruk av propen og isobutan som hydrokarboner i våt føde. Egne konvensjonelle og hierarkiske SAPO-34 prøver ble syntetisert, ved variering av ulike faktorer under miksing av syntese gelen og krystalliseringen. De fase rene prøvene ble ionebyttet med Ag^+ og Cu^{2+} separat og samtidig, 4 ganger for hver prøve. Mekanisk miksede prøver ble også laget ved bruk av lik mengde sølv og kopper prøve. Fase renheten og krystalliniteten til prøvene ble karakterisert med røntgendiffraksjon (XRD) og porøsiteten med BET overflate analyse før og etter ionebytting. Metallinnhold i prøvene ble bestemt med ICP-MS, med en økning ifra første til fjerde runde med ionebytting. NO_x omdanning for de analyserte prøvene ble målt med en chemiluminescence NO_x analyser, etter første og fjerde runde med ionebytting.

Cu:SAPO-34 prøvene var aktive for både de konvensjonelle og hierarkiske prøvene, men Ag:SAPO-34 prøvene var inaktive. Prøvene som ble ionebyttet samtidig med sølv og kopper viste lavere aktivitet enn sine Cu:SAPO-34 motstykker, men med mye lavere kopper innhold som kunne bety en synergisk effekt med sølv. Alle disse prøvene hadde en økning i NO_x omdanning ifra første runde til fjerde runde med ionebytting. De mekanisk miksede prøvene ble kun kjørt for sølv og kopper prøvene etter 4 runder med ionebytting og viste høyere maks NO_x omdanning enn kopper prøvene. Dette var ikke over et like bredt temperaturintervall, men likevel med halvparten av kopper tilstede som kunne bety en liknende synergisk effekt ifra sølv. Maks omdanning ble oppnådd av den konvensjonelle mekanisk miksede prøven og var 60 % ved 500 °C.

Metall innhold så ut til å ha en større effekt på NO_x omdanningen enn porøsiteten av prøvene, siden en økning i NO_x omdanning tok sted til tross av tap i porøsitet i prøvene etter ionebytting. Porøsitet var viktig for de mekanisk miksede prøvene. Ingen aktivitet ble registrert ved bruk av isobutan, som antydet lav konsentrasjon av aktive seter i de mulige mesoporene av den hierarkiske prøven og på den eksterne overflaten til krystallittene av både den hierarkiske og konvensjonelle prøven.

Table of contents

List of Figures

List of Tables

Abbreviations

AlPO – Alumino phosphates

AN – Ammonium nitrate (NH_4NO_3)

AP – “As prepared”, the first stage after synthesis and before the calcination of a sample

A-I – Aluminium isopropoxide (aluminium source)

BET – Brunauer Emmett Teller – theory for surface area

Cal – Calcinated sample

CCP – Close cubic packed crystal structure

CHA – Chabazite crystalline structure

DPF – Diesel particulate filter, part of a typical diesel emission control system

HC – Hydrocarbon

HC-SCR – Selective catalytic reduction with hydrocarbons as reducing agents

ICP-MS – Inductively coupled plasma – mass spectrometry

IE – Ion exchange

Meso-SDA – Structure directing agent for introducing meso-sized pores and channels inside the zeolite/zeotype during crystallisation

µm - Micrometers

MTO – Methanol to olefin reaction

M:SAPO34 – Ion exchanged SAPO-34 where M is either ammonium, silver, copper or both silver and copper (AgCu) (co-ion exchange)

NH_3-SCR – Selective catalytic reduction with ammonia as reducing agent

nm – Nanometers

NO_x – Nitrogen monoxide and nitrogen dioxide mixture

PBU – Primary building unit

PPM – Parts per million

PSD – Pore size distribution

P-B – Pseudo boehmite (aluminium source)

PV – Total pore volume of a porous material

SAPO – Silico aluminophosphate

SBU – Secondary building unit

SCR – Selective catalytic reduction

SDA – Structure directing agent (For synthesis of zeolites and zeotypes)

SEM – Scanning electron microscopy

SSA – Total specific surface area of a porous material

TEAOH – Tetraethyl ammonium hydroxide

TEA – Triethyl amine

TPOAc – 3-(trimethoxysilyl)propyl octadecyldimethylammonium chloride

TWC – Three way converter catalyst employed in larger transport vehicles

XRD – Powder x-ray diffraction

ZSM-5 – Zeolite Socony Mobil-5

Zeolite Y – Faujasite zeolite structure

Å – Ångstrøm

1.0 Introduction

Copper (Cu) containing zeolites and zeotypes based on the microporous chabazite (CHA) framework, such as the Cu:SSZ-13 framework have high activity in important reactions. Reactions such as the selective catalytic reduction of NO_x towards N_2 using hydrocarbons (HC-SCR), and the methanol to olefin (MTO) reaction.[1-3] These frameworks have superior hydrothermal stability in realistic conditions than larger pored frameworks due to more rigid and closely packed structures.[2-6] Hydrothermal treatment at temperatures greater than 500 °C however, reduces the activity of the aluminosilicate Cu:SSZ-13 material.[7] This is disadvantageous where the diesel particulate filter (DPF) in a diesel engine is periodically heated to temperatures greater than 650 °C, to burn off the particulate matter.[8] Because of these materials' rigidity and pore openings smaller than the pores themselves, they suffer from diffusion limitations and as a result large intermediates clogging up the pores.[7, 8] In time the active sites inside the frameworks are blocked by the stuck intermediates, and the catalyst becomes deactivated.[7, 8] Reducing diffusion limitations of reactants and products in and out of the CHA framework, and increasing its hydrothermal stability are important aspects to improve for the material's longevity as a catalytic framework.

The microporous silicon based zeotype SAPO-34 with the same CHA framework containing copper, has received much attention due to its similar activity in the same reactions. It has better stability for temperatures > 650 °C in wet conditions than Cu:SSZ-13, but its conventional structure struggles with the same diffusion limitations.[9] In recent years, a lot of work has been dedicated into synthesizing so-called hierarchical framework versions of the conventional frameworks of zeolites and zeotypes.[10] The idea is the conventional framework as a basis, where mesopores and channels (> 2 nm and < 50 nm) are connected to the external surface of the material's crystallites, very similar to a Swiss cheese.[11-15] Introducing mesopores and channels, is either done in-situ by adding mesosized organic molecules as scaffolding for the conventional framework to build around, or by post-synthesis treatment such as etching.[16] Hierarchical frameworks have had a great impact on reducing diffusion limitations, as the larger pores increase diffusion into the crystallites utilizing more of the internal surface.[10-15] Reducing the crystallite size would make more of the total surface area external and available for catalysis as well.[11-15] In this thesis however, the former description of mesopores and channels in the conventional structure, is the hierarchical version sought after.

Even though SAPO-34 has good thermal (> 650 °C) stability in wet conditions at higher temperatures, it is sensitive to moisture at temperatures below 100 °C.[2, 3, 5, 17-23] Direct aqueous ion exchange (IE) of silver (Ag) and copper species into the framework leads to irreversible hydrolysis of the hydrophile Brønsted acid sites in the structure, from which Botne's samples completely collapsed.[2, 3, 5, 17-24] By employing a two-step ion exchange, first with ammonium nitrate (NH_4NO_3) followed by the metal species, the crystallinity is conserved much better where the ammonium ion (NH_4^+) protects against hydrolysis.[20, 22, 23] The Ag^+ ion is reported to have the same protective effect as the ammonium ion and increases catalytic activity for HC-SCR of NO_x at lower temperatures as well.[2, 3, 5, 17-23] How well the samples in this thesis perform in the HC-SCR of NO_x will not be the main focus, but rather what the results from the reaction and characterization techniques used can tell about the samples' own structural characteristics.

This master's thesis was a continuation of Botne and Schjetlein, 2 earlier members in the same research group as the author, also using HC-SCR of NO_x.[24, 25] HC-SCR of NO_x was used as a model reaction with regards to the synthesized SAPO-34 samples, to investigate the effect of the different porosities in the samples and the presence silver had on the conversion of NO_x. Ag^+ was present in 2 ways, through simultaneous ion exchange of Ag^+ and Cu^{2+} into the framework, or by mechanically mixing two separate samples, one containing Ag^+ and the other Cu^{2+}.[5, 26-28] Locating where the active single sites of ion exchanged Ag^+ and Cu^{2+} species resided within the frameworks was investigated by using hydrocarbons of different sizes.[29, 30] Propene and isobutane were used as hydrocarbons where propene fitted through the pore openings of the conventional SAPO-34 framework, while isobutane did not.[29, 30]

Before the HC-SCR of NO_x could be used however, several aspects of the synthesized samples had to be characterized and in place beforehand. The synthesized samples had to be phase pure SAPO-34, and conventional and hierarchical samples were needed in order to investigate the effect of porosity. The porosity and crystallinity of the samples had to be preserved during ion exchange with Ag^+ and Cu^{2+} and the resulting metal content in the samples had to be characterized. When these were in place, the HC-SCR of NO_x could be used to further investigate the effect of porosity and presence of silver in the samples as described above.

2.0 Theory

This section introduces with the characteristics of the conventional SAPO-34 zeotype, and why it is such an interesting and promising material for catalysis. From here, the possible hierarchical versions will be introduced and which one is the desired version, and how to synthesize the material hydrothermally. This is followed by how copper and silver can be introduced into the structure as single sites by ion exchange. Afterwards, the role of these species in the SCR of NO_x until this day is considered, followed by how the reaction can be used as a model reaction using differently sized hydrocarbons as reductants. Finally, theory on the characterization techniques used to investigate the crystallinity, phase purity, porosity and metal content in the structure is presented.

2.1 SAPO-34

2.1.1 Conventional SAPO-34

Silicoaluminophosphate-34 (SAPO-34) is an ordered microporous structure belonging to the silicon based zeotype family of SAPO structures.[31, 32] In general, the chemical formula for SAPOs is $Si_xAl_yP_zO_2$ where the sum of x, y and z is 1.[31] The ratio between Al and P is 1:1, where Si is substituted into some of the Al and P sites of the framework.[31] Together with oxygen, these 3 elements referred to as T-atoms make up the primary building units (PBUs) of the framework.[31, 33] These are so called TO_4 tetrahedrals, where a T atom is in the center of the tetrahedra made up of 4 surrounding oxygen atoms (Figure 2.1.a).[31, 33]

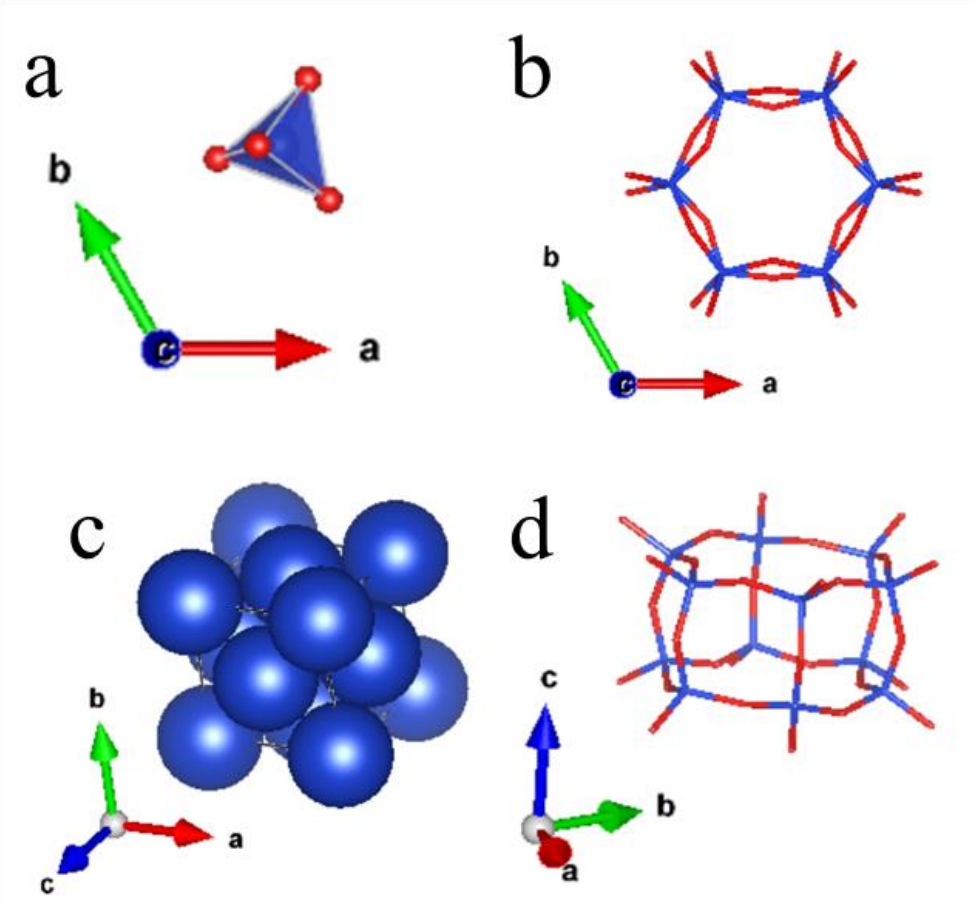

Figure 2.1:a) TO_4 tetrahedral (PBU) where T=Al,Si,P. b) Double 6-membered ring of CHA framework (SBU), watched along the c direction. c) CCP structure in which the SBU lay in an ABCABC pattern. d) SBU. Reproduced with permission from VESTA Crystal information files from the international database of zeolites.[32, 34]

The PBUs in turn link together by the corners to make up secondary building units (SBUs).[31, 33] In the case of SAPO-34, 6 PBUs link together to make a 6-membered ring, where 2 such rings link together on top of each other, making up the SBU (Figure 2.1.b and d).[32] The conventional SAPO-34 structure is built up of these SBUs lying in an ABCABC layered pattern, as in a close cubic packed (ccp) structure, adopting the framework of the chabazite (CHA) zeolite (Figure 2.1.c and 2.2.a).[32] By the arrangement of the SBUs, also 4- and 8-membered rings are part of the structure (Figure 2.2.a and b).[32]

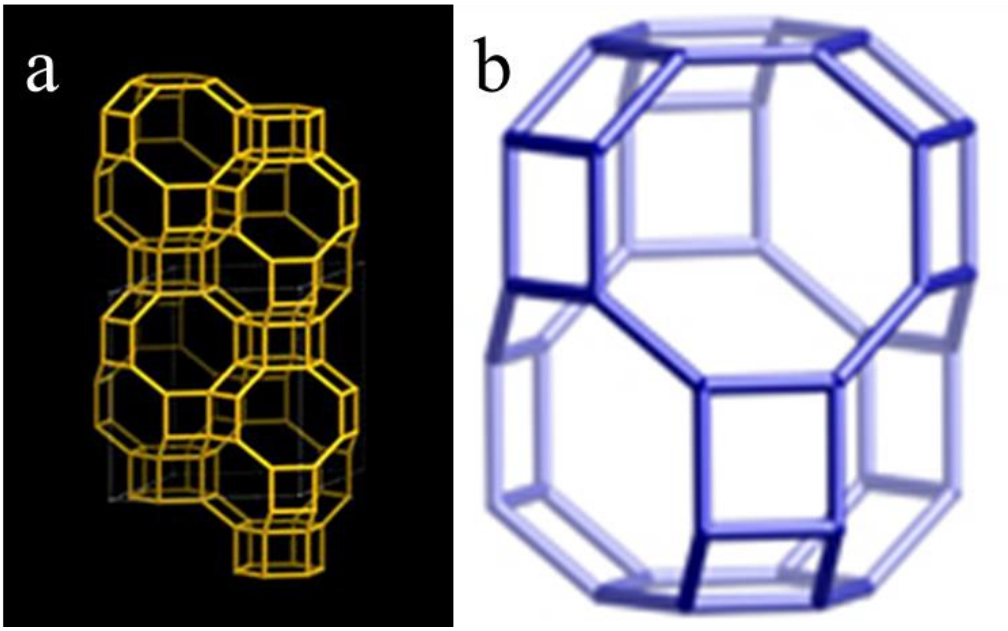

Figure 2.2: a) 3D image of the CHA framework illustrating the ABCABC pattern of the SBUs, which in turn make out the additional 4-membered and 8-membered rings. b) Illustrates the CHA cage unit of the SAPO-34 microporous framework. Reproduced with permission from the international database of zeolites.[32]

SAPO-34 is known for its repetitive CHA cage unit (Figure 2.3.b), where the diameter of the 8-membered ring (3.8 Å), is smaller than the inner diameter of the cage unit (9.4 Å).[12, 32, 35] Both sizes are in the microporous range (< 2 nm) of porous inorganic materials.[12, 32]

With a description of the SAPO-34 framework established, the following section presents the properties of the material making it an interesting and versatile catalytic material.

2.1.2 SAPO-34 in catalysis

Conventional SAPO-34 hosts many properties that make it an excellent framework for catalysis. Because of the double 6-membered ring structure (SBU) that is arranged in a ccp structure described in section 2.1.1, the material has high thermal stability (> 650 °C), also in wet conditions.[2, 3, 5, 17-23] It has a high internal surface area of theoretical value 550 m^2/g, important for all catalytic material as the value reflects how much of it is unavailable bulk material, and how much is available interface for reacting species to interact with.[36] The central active sites on the available interface important for this thesis are the inhabitant Brønsted acid sites inside the microporous framework, further explained in section 2.2. SAPO materials are in general based upon analogous alumino phosphate (AlPO) frameworks, where silicon is present as T atom as well along with Al and P.[37] When silicon occupies a phosphorus site in the AlPO framework, a formal negative charge is established.[11, 37, 38] Neutral charge is restored by a cation bonding onto one of the 4 oxygen bridges directly bonded to the silicon atom, becoming a Brønsted acid site in case the cation is a proton (Figure 2.3).[11, 38]

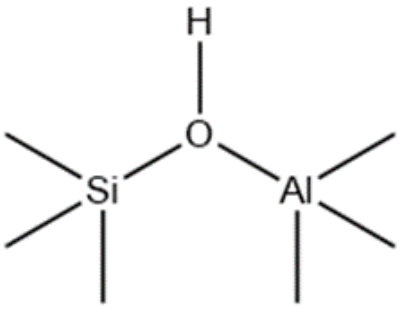

Figure 2.3: Silicon in the T position of phosphorus, giving the structure a net negative charge. The neutral charge is restored by a bonding proton on 1 of the 4 oxygen bridges directly bonded to the silicon atom, creating a Brønsted acid site.[39]

The Brønsted acidity can be controlled by adjusting the Si:Al ratio, and is important for the methanol to olefin (MTO) reaction.[12] Here, the acid sites convert the methanol to olefins by acidic catalysis, and are in part responsible for the high selectivity (> 80 %) for the lighter olefins ethylene and propylene.[12, 40] The other part responsible is the material's unique CHA cage (Figure 2.2.b) where the largest 8-membered ring opening into the cage (3.8 Å) is smaller than the cage itself (9.4 Å).[12, 32, 35] This provides the material with a native shape selectivity, with both positive and negative effects explained below.

Teketel et al. describes 3 shape selectivities inherent in a zeolitic catalyst, depending on the stage of the reaction.[35] First is the reactant shape selectivity, where in case of SAPO-34, reactants must be small enough to diffuse through the 8-membered ring to reach the active sites inside the CHA cage.[35] Second is the restricted transition state selectivity, where the pore restricts a transition state to a certain size towards the product formation.[35] Finally is the product shape selectivity, where only small enough products can exit the pores.[35]

The CHA cage functions as a cavity allowing for product formation larger than the pore opening.[12, 32, 35] The product will have to react further into smaller species in order to be able to leave the CHA cage.[35] As such, the shape selectivity of the CHA cage becomes a double-edged sword, where it provides high selectivity for smaller products, but just as well can get clogged if the intermediates inside grow too big.[12, 40] Coking in MTO and SCR of NO_x is an example of this, where organic intermediates too large to exit the CHA cage block the active sites for further use, deactivate the material gradually and have to be burnt off.[12, 40] Also because of the small pore openings, conventional SAPO-34 already suffers from diffusion limitations, rarely utilizing the active sites in the center of its crystallites. Here, the gradual clogging of its micropores will further increase the diffusion limitations. [11-15, 35]

At this point, the characteristics, high suitability and limitations of conventional SAPO-34 in catalysis have been established. In the next section the hierarchical version of SAPO-34 is introduced as an approach to reduce the limitations of the conventional version.

2.1.3 Hierarchical SAPO-34

In order to reduce the diffusion limitations the conventional SAPO-34 suffers from, 2 main approaches can be taken to utilize more of the active sites in the bulk of the crystallites. One is to reduce the crystallite size of the conventional material, converting more of the internal surface area into available external surface area.[12, 40] The other is by hollowing out the microporous crystallites introducing larger pores and channels in the mesosize range (> 2 nm and < 50 nm) connected to the surface of the crystallites.[12, 13, 15] This approach will result in crystallites containing pores in both the microporous (< 2 nm) and mesoporous (> 2 nm and < 50 nm) size range.[12, 13, 15] Figure 2.4 clearly illustrates the effect of mesopores in the conventional structure for catalysis, where the reactant concentration remains constant through the whole bulk of the material making use of all active sites. Frameworks consisting of both micro- and mesopores are called hierarchical frameworks.

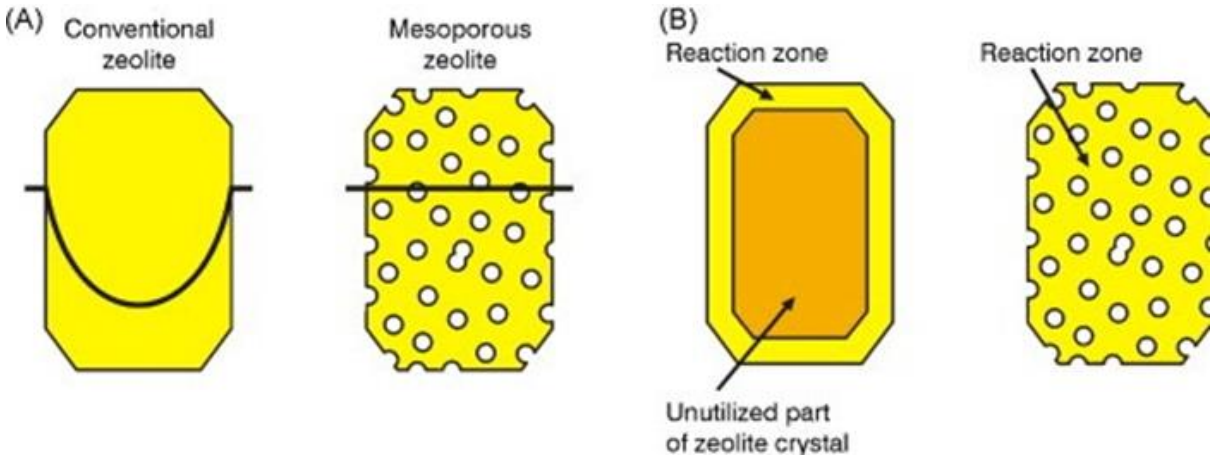

Figure 2.4: a) Concentration profile of reactants throughout a conventional and hierarchical molecular sieve respectively, illustrating the diffusion limitations of the conventional material. b) Illustration of the active reaction zones in the conventional and hierarchical materials respectively in catalysis. The hierarchical material utilizes most of its surface area, while the conventional material is only utilizing the outer surface. Reproduced with permission from Elsevier.[9]

Introducing mesopores and channels into the conventional crystallites, can be done by adding templates/structure directing agents (SDAs) in the meso range (meso-SDAs), further described in section 2.1.4.[14] These mesopores can be intracrystalline voids surrounded by the conventional framework (Figure 2.5 and 2.6.c), while the first approach of reduced crystallite size will be intercrystalline voids between smaller randomly oriented conventional crystallites (Figure 2.6.b).[15] Both systems are considered hierarchical, but the intracrystalline version was the desired version in this thesis where meso-SDAs were actively added to the synthesis gel.[15]

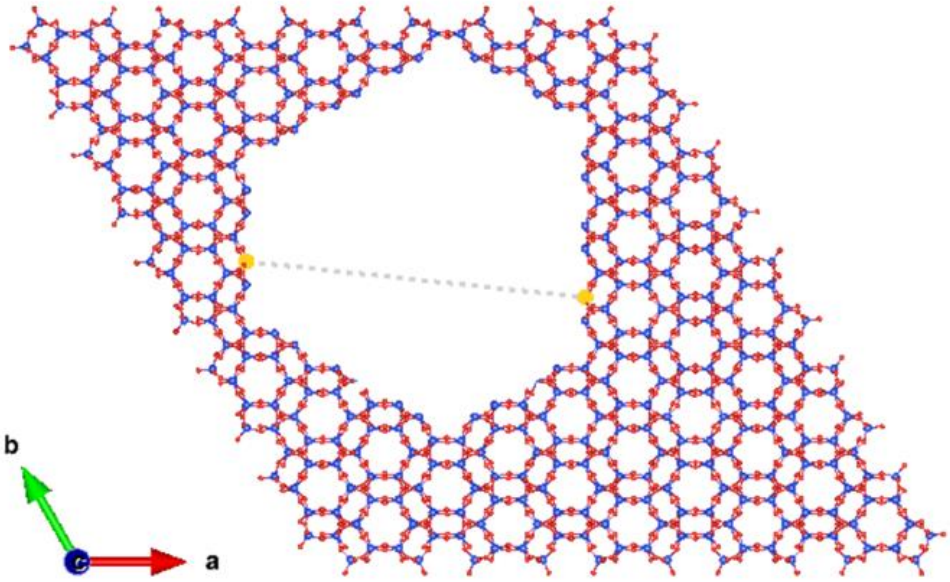

Figure 2.5: Example of a mesoporous void or channel through the microporous framework along the c direction. Figure produced with the software program VESTA.[34]

Figure 2.6.d illustrates the undesired outcome of an encapsulated mesopore not able to function as a "highway" for diffusing species. The conventional framework has built around it and encapsulated it completely, leaving no mesoporous openings at the outer surface of the crystallite.[15]

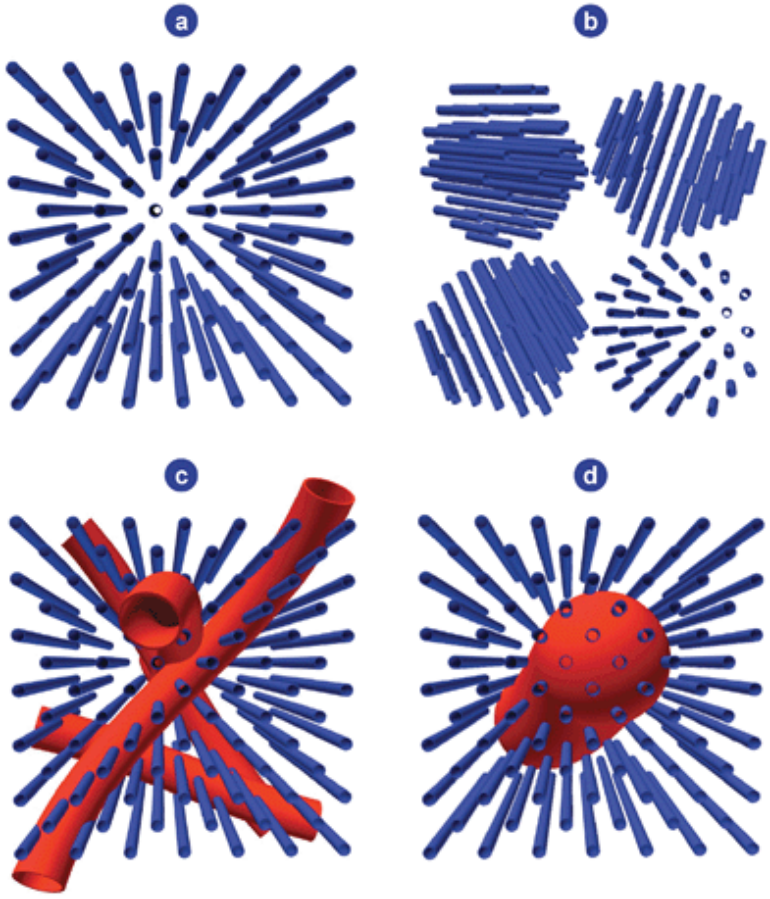

Figure 2.6:a) Microporous channels of a general zeolite/zeotype framework. b) Several microporous crystallites of the same zeolite/zeotype framework with inter crystalline meso sized voids. c) Meso sized channels or "highways" leading reactants and products to and from active sites residing with the micropores. d) Encapsulated meso void unable to function as "highway".[15] Reproduced with permission from Elsevier.

The characteristics of the conventional SAPO-34 and its hierarchical version have been established, along with its suitability for catalysis. In the next section, the challenges in hydrothermal synthesis of SAPO-34 and introducing mesopores will be described.

2.1.4 Synthesis of conventional and hierarchical SAPO-34

Developing synthesis routes for conventional and hierarchical SAPO-34 always giving phase pure results is important, as competing phases such as SAPO-5 with the AFI zeolite framework favour similar synthesis conditions.[11, 31] Hydrothermal synthesis is a common technique for making conventional SAPO-34 and was employed by the author in this thesis.[11, 31, 41] For promoting mesoporosity into the conventional framework, 2 different meso-SDAs (Figure 2.7) have been added as soft templates to the synthesis gel as an in-situ bottom-up approach.[41]

Several factors during mixing of the synthesis gel and crystallisation, play important roles for the phases present after crystallisation.[11, 31, 41] Below, a short description of the hydrothermal synthesis and effect of varying different factors during the synthesis is given. These factors were varied in this thesis in order to see how well the results overlapped with results from the literature used, and whether the first goal of synthesizing phase pure conventional and hierarchical SAPO-34 was reached.

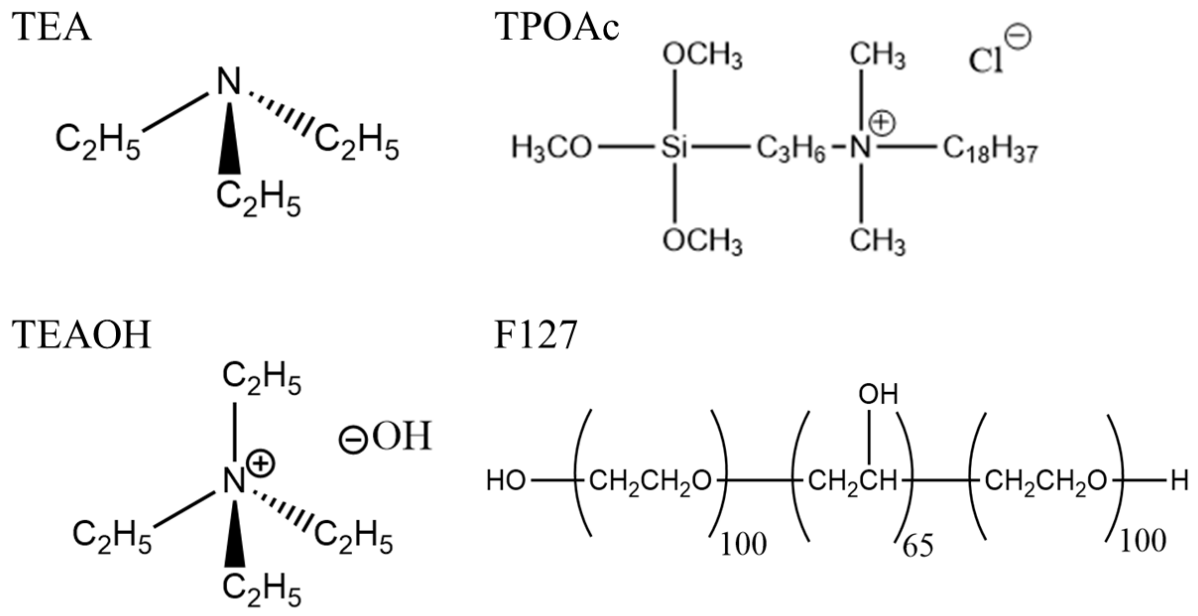

Figure 2.7: SDAs TEAOH and TEA commonly used for hydrothermal synthesis of the SAPO-34 framework, and the meso-SDAs commonly used for promoting mesopores inside the crystallites, TPOAc and Pluronic F127.

In hydrothermal synthesis, the synthesis gel consists of water as a continuous medium, with hydroxide as the main mineralizing agent, and a source for each main component, silicon, aluminium and phosphorous.[11, 42] SDAs are added as scaffolding for the components to

nucleate around, constructing the microporous framework.[11] Crystallisation occurs inside a sealed Teflon liner encapsulated by an autoclave, at temperatures in the range of 150-220°C.[41] Common SDAs for SAPO-34 are triethylamine (TEA) and tetraethyl ammonium hydroxide (TEAOH) illustrated in Figure 2.7, along with the common meso-SDAs Pluronic F127 and TPOAc (3-(trimethoxysilyl) propyl octadecyl dimethyl ammonium chloride).[11]

Askari et al. performed a study on the effect of SDA concentration, crystallisation time and temperature, to determine the favouring conditions for SAPO-34.[11] The AFI framework (SAPO-5) (Figure 2.8) is the main competing phase during the synthesis process, due to its similar structure and synthesis conditions.[11, 32] Askari et al. found that high temperature (200 – 220 °C), at crystallisation time (24 h) and increased SDA concentration of TEA (Al:TEA 1:3) favoured SAPO-34.[11] High temperature led to the preferred thermally stable 6-membered double ring structure of SAPO-34 rather than the 12-membered ring of SAPO-5 (Figure 2.8).[11]

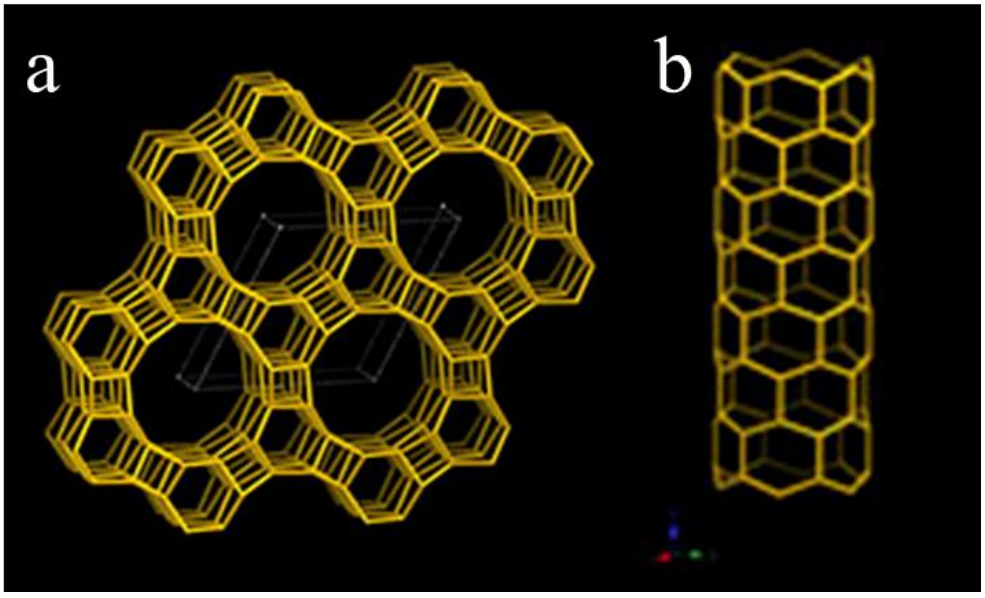

Figure 2.8:a) 1 Dimensional framework of AFI displaying the 12-membered ring channels along the c direction. b) The 12-membered ring channel of the AFI structure viewed from the side. Reproduced with permission from the international database of zeolites [32]

According to Sun et al., catalysts synthesized using both TEA and TEAOH with a ratio of 0.1, resulted in phase pure SAPO-34 with higher surface area, catalytic activity and smaller crystallite size, than when only 1 SDA was used.[11, 12, 43] With regards to silicon source used, the smaller the particles in the silicon source, the more favoured was the SAPO-34 structure according to Izadbakhsh et al.[38] Emrani et al. informs of silica gel providing larger crystallites with smaller size distribution, contrary to the organic precursor for silicon, tetraethyl

orthosilicate (TEOS), giving smaller crystallites, but with a larger size distribution.[44] The Si:P ratio cannot be too large as the SAPO structure would revert back to the silicon structure on which it is based. It can neither be too small as the silicon will not be completely distributed into the framework, and AlPO – phases will emerge in areas of the final crystallised sample.[44] As such, the ratio lies between 0.1 and 1 normally, and has been between 0.1 and 0.5 in this thesis.[38] Aluminium hydroxide and aluminium isopropoxide (A-I) are inorganic and organic sources for aluminium respectively, where Emrani et al. states the organic source provides a more homogeneous reaction precursor.[44] Both were used in this thesis, where pseudo boehmite (72.8 wt%) was used as inorganic source.

Pluronic F127 and TPOAc illustrated in Figure 2.7, are so-called soft templates and were used as organic meso-SDAs in this thesis.[45, 46] Pluronic F127 can act as both meso-SDA and growth inhibitor, regulating the size of the crystallites forming during crystallisation.[47, 48] Sun et al. used TPOAc in hydrothermal synthesis of hierarchical SAPO-34, resulting in agglomerates composed of nanosized crystallites.[46] Here the mesoporosity is present in the form of mesovoids illustrated in Figure 2.6.b.[46] Using a quaternary ammonium organosilane surfactant as meso-SDA shows much promise as the species can act as both silicon source and meso-SDA, preventing phase separation between the crystallizing microporous framework and the meso-SDA, which can occur with F127.[49]

2.2 Introduction of silver and copper into SAPO-34

There are in general 3 main methods of integrating silver and copper single sites into the framework of zeotypes, which are ion exchange (IE), incorporation and impregnation.[50] Incorporation is understood by directly replacing T-atoms in the framework with either silver or copper, by adding these components before crystallisation.[50] Impregnation consists of letting nanosized clusters of silver and/or copper either diffuse into the porous framework and settle inside the micropores, or let the framework build around them during crystallisation.[51] These 2 methods were not performed in this thesis, which focused on the ion exchange of Ag^{+} and Cu^{2+} species into the SAPO-34 framework.[50]

2.2.1 Ion exchange in SAPO-34

As introduced in section 2.1.2, silicon replacing phosphorus as T-atom results in a net negative charge of the framework. This charge becomes neutral again by a cation bonding to 1 of the oxygen bridges directly bonded to the silicon atom. When this cation is a proton, the oxygen bridge becomes a Brønsted acid site.[11, 38] As these protons can dissolve into water, they can naturally be exchanged with metallic cations as well (Figure 2.9) such as Ag^{+} and Cu^{2+}.[52, 53] The possibility of exchanging different metallic species into the framework as single sites makes it even more versatile in catalysis, where silver and copper have high activity in SCR of NO_x (90-100 % conversion).[23, 54]

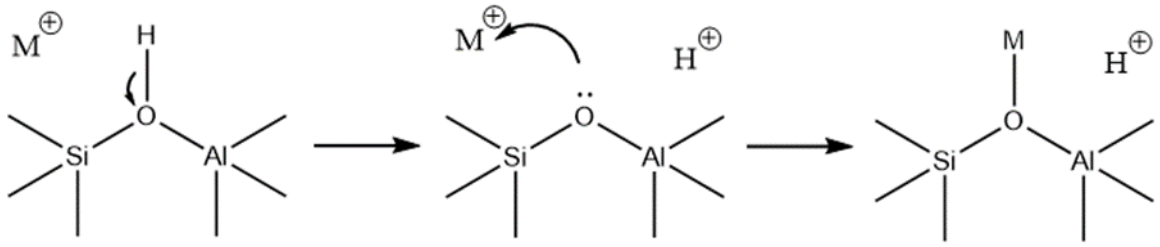

Figure 2.9: Ion exchange of a metallic cation onto an oxygen bridge directly linked to the silicon atom, exchanging the proton and restoring neutral charge to the framework at that specific site.

With aqueous ion exchange, Cu^{2+} and Ag^{+} content inside the porous framework can in theory be controlled by changing either the amount of solution or molarity of the solution used, independent of metal salt used. [19, 52, 53] In this thesis, $AgNO_3$ and $Cu(NO_3)_2x3H_2O$ were used exclusively as salts for ion exchange. The desired metal loading for both silver and copper in this thesis' samples is at least close to what Botne and Schjetlein reached (ca. 3-4 wt% for

copper and over 5 wt% for silver) in order to compare the conversion of NO_x obtained in this thesis during the selective catalytic reduction (SCR) with propene or isobutane.[24, 25] Botne used a dry feed during the HC-SCR of NO_x. In case the metal loading was too low after the first round of ion exchange, consecutive rounds of ion exchange were performed in order to increase the metal content inside the framework.

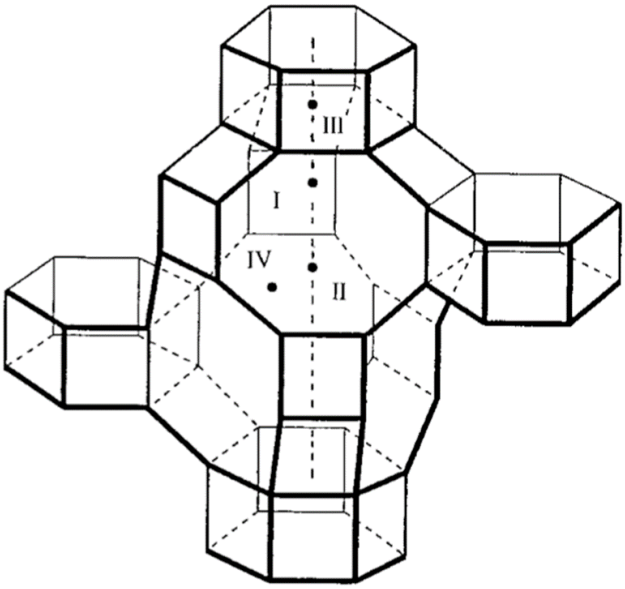

Figure 2.10: Possible positions for introduced metal cations to occupy. Preferred position of Cu^{2+} and Ag^{+} is (III), (IV) at increased metal content.[55] Reproduced with permission from ACS Publications.

Figure 2.10 illustrates the cage unit of the CHA structure, and which positions introduced metal species are most likely to occupy. Deka et al. prepared conventional SAPO-34, introducing Cu^{2+} by aqueous ion exchange.[56] The ion exchanged catalysts had high catalytic activity in NO_x conversion and high selectivity towards N_2. [56] Here, the exchanged and isolated Cu^{2+} ions mainly occupied the sites at the 6-membered ring of the CHA structure (position III, Figure 2.10).[2-4, 17, 56-58] Fickel et al. also confirmed this, stating that the isolated copper species coordinated to 3 oxygen atoms in the 6-membered ring were the active sites of the Cu:SSZ-13 framework in HC-SCR of NO_x.[2-4, 17, 56-58] The presence of the copper species in these positions, also further contributes to the high hydrothermal stability (> 650 °C) of the CHA framework.[3-6, 59, 60] When copper content is increased further (> 3 wt%), sites at the 8-membered ring of the CHA structure (position IV, Figure 2.10), will also become occupied.[4, 17, 61] Cu^{2+} in this site also contributes to the high temperature hydrothermal stability, but also leads to undesired hydrocarbon oxidation in the HC-SCR of NO_x reaction.[4, 17, 61]

2.2.2 Two-step ion exchange method

As stated earlier, the CHA framework of the SAPO-34 structure has good high temperature (> 650 °C) hydrothermal stability, further increased with the introduction of Cu^{2+} species in the 6- and 8-membered rings.[3-6, 59, 60] Although having high stability (> 650 °C) in wet conditions, the calcined SAPO-34 structure, free of organic SDAs is less stable in wet conditions at lower temperatures (< 100 °C).[2, 3, 5, 17-21] Exposure towards water over several days can cause partial structural collapse.[2, 3, 5, 17-21] The collapse is due to the irreversible hydrolysis of the bridge hydroxyl groups, present at the oxygen bridge between aluminium, and silicon substituted into the phosphorus sites, in other words the Brønsted acid sites (Figure 2.11).[2, 3, 5, 17-21] Increased crystallite size will increase resistivity towards hydrolysis, as the diffusion of water into the bulk of the crystallites is slowed down.[60, 62] This will mean ion exchange mostly occurring at the surface of the crystallites.[60, 62]

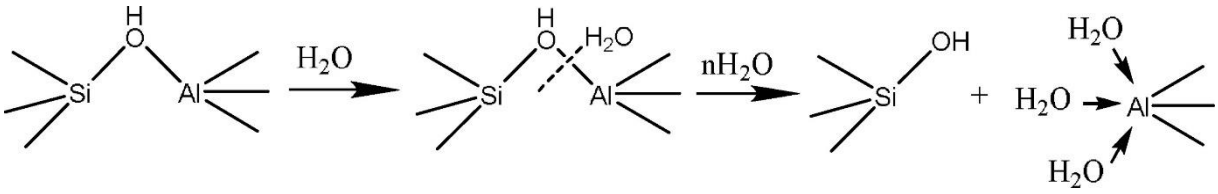

Figure 2.11: General hydrolysis reaction of zeotype frameworks. Reproduced with permission from Elsevier.[20]

Direct aqueous ion exchange presents challenges regarding introduction of metal ion single sites into the microporous framework of zeotypes, because of the hydrolysis occurring at the Brønsted acid sites.[18, 63, 64] Several research groups have performed a so-called two-step ion exchange method, where ammonium (NH_4^+) species first are exchanged into the framework before the metal cations.[2, 3, 17-21] Xu et al. performed an extensive research on the presence of the ammonium species in the Brønsted acid sites of SAPO-34.[20, 22, 23] Here, they found that the adsorbed, hydrophile ammonia shields the Al-OH-Si bridge from hydrolysis.[20, 22, 23] NH_4^+ introduced through liquid ion exchange provided most monodentate NH_4^+ species, which in turn promoted Cu^{2+} as dispersed single sites through the microporous framework, during the second round of aqueous ion exchange.[20] The presence of remaining NH_4^+ species after ion exchange with metal species in the second round will further protect the framework from low-temperature (<100 °C) hydrolysis.[20, 22, 23] Ag^+ was found to have a similar protecting effect as the NH_4^+ species on the Brønsted acid sites towards hydrolysis by Xiang et al, when ion exchanging both Ag^+ and Cu^{2+} simultaneously into the framework.[5]

At this point, the conventional and hierarchical SAPO-34 frameworks and their suitability for catalysis have been described, and how Ag^{+} and Cu^{2+} species can be introduced as single sites into the framework by the two-step ion exchange method. Botne's samples completely collapsed when using the direct ion exchange method of Ag^{+} and Cu^{2+}, but still had high NO_x conversion for the copper samples (ca. 60 %), and very high (83 %) for the simultaneously exchanged AgCu:SAPO-34 conventional sample.[24] The following section will look more into the role of silver and copper in HC-SCR of NO_x.

2.3 Copper and silver containing SAPO-34 in HC-SCR of NO_x

This section starts with a description of the HC-SCR of NO_x, providing the main reactions occurring during the reduction towards N_2. Afterwards the roles of Ag^+ and Cu^{2+} as active single sites inside SAPO-34 for the HC-SCR of NO_x are described, and finally how the HC-SCR of NO_x can be used as a model reaction to further characterize the samples.

2.3.1 Selective catalytic reduction with hydrocarbons (HC-SCR) of NO_x

HC-SCR of NO_x is a promising alternative instead of NH_3-SCR of NO_x. Here, the excess hydrocarbons already present in lean-burn diesel exhausts are used as reducing agents in excess oxygen, instead of NH_3 in the form of urea in a separate tank.[1, 21, 65-67] Chen et al. reports that HC-SCR active catalysts also perform well as NH_3-SCR catalysts, as NH_3 is formed as an intermediate in the reaction mechanism of NO_x reduction.[60, 68-71]

In order to successfully reduce NO_x towards N_2, oxidizing NO towards NO_2 as an intermediate is an important step in the reaction mechanism before further reducing NO_2 towards N_2.[54, 72] Catalysts must therefore have a high selectivity for NO_2 at the oxidative site of the catalyst (equation 2.1)[71], rather than the undesired intermediate N_2O.[54, 72]

$$2NO + O_2 \rightarrow 2NO_2 \qquad 2.1$$

Equation 2.2 displays the desired reduction of NO_2 by use of hydrocarbons (propene in this case), however equation 2.3 displays the possible unwanted direct oxidation of the hydrocarbons with oxygen.[28, 71]

$$4NO_2 + 2C_3H_6 + 5O_2 \rightarrow 2N_2 + 6CO_2 + 6H_2O \qquad 2.2$$

$$2C_3H_6 + 9O_2 \rightarrow 6CO_2 + 6H_2O \qquad 2.3$$

Propene and isobutane have been used as hydrocarbons in this thesis, but before looking at the effect of using different sized and shaped hydrocarbons, the role of silver and copper in HC-SCR of NO_x will be presented below.[28, 71]

2.3.2 Cu:CHA in HC-SCR

Copper containing CHA-based catalysts, prepared through the two-step ion exchange method are reported to have excellent N_2 selectivity and conversion of NO_x between 90 % – 100 % in the temperature range of 200 – 550 °C according to Xie et al.[23] The oxidation state and position of copper inside the CHA-framework has a lot to say for the material's catalytic activity. As mentioned earlier, Cu^{2+} in either the 6- or 8-membered ring position provides the framework with additional high temperature (> 650 °C) hydrothermal stability, but the 6-membered ring position is recognized as the active site for HC-SCR of NO_x.[3-6, 23] Cu^{2+} located on the 8-membered rings are more prone to oxidize hydrocarbons directly in SCR, despite providing hydrothermal stability.[5] CuO species can also form inside the CHA framework, which are prone to directly oxidize hydrocarbons.[5]

The Cu^{2+} species as active sites in zeolites perform a complete redox cycle to Cu^{+} and back to Cu^{2+} during the HC-SCR of NO_x, forming the important NO_2 intermediate.[73, 74] The species responsible for reducing and oxidizing the copper site has several suggestions from the literature.[73, 74] Liu et al. suggests a full redox cycle where propene adsorbs on Cu^{2+}, forming a Cu^{+}-allylic species which is oxidized again by NO and O_2, forming N_2, H_2O and CO_2.[73] Liu et al. states the importance of rich O_2 conditions to avoid formation of coke, supported by Moreno-González et al. also stating the importance of O_2 to avoid too much reduction of the Cu^{2+} single sites.[73, 74] Moreno-González et al. suggests the Cu^{+} species forms $Cu^{2+}NO_3^{-}$ with NO and O_2, which reacts with ammonia to form N_2 and H_2O, and the Cu^{2+} is reduced back to Cu^{+} by propane.[74]

2.3.3 Silver in HC-SCR

Xiang et al. reports of Ag:SAPO-34 having NO_x conversion less than 10 % below 250 °C, just like Cu:SAPO-34 below 250 °C.[5] Ag:SAPO-34 does have higher stability towards hydrolysis than Cu:SAPO-34 by maintaining higher crystallinity from x-ray diffraction (XRD) diffractograms, due to the protective effect of the Ag^+-ions, mentioned earlier.[5] Azizi et al. describes the importance of the silver(I)oxide in alumina frameworks (Ag_2O/Al_2O_3) for HC-SCR activity, while metallic silver clusters instead will lead to the combustion of the hydrocarbons.[72] Clusters of Ag^+ inside the Al_2O_3 framework were crucial for the reduction of NO_x, where Halasz et al. suggests the silver species having low activity for oxidizing NO towards NO_2.[72, 75, 76]

Mathisen, et al. proposes Ag^+ ion exchanged into the ZSM-5 and SAPO-5 forms reduced silver nanoparticles using propene as hydrocarbon in the HC-SCR of NO_x.[77] Here, the metallic Ag nanoparticles are in turn suggested to be oxidized to Ag^+ again by NO, although not fully redispersed as single sites.[77] The degree of metallic silver formed is suggested to be closely related with the activities of Ag:SAPO-5 and Ag:ZSM-5 in HC-SCR of NO_x, as Ag^+ is reduced more effectively in the former.[77]

2.3.4 Simultaneously exchanged silver and copper containing SAPO-34 in HC-SCR

Xiang et al. reports that addition of silver into Cu:SAPO-34 (AgCu:SAPO-34) has no apparent effect on the SCR activity of Cu:SAPO-34, in the temperature range of 120 – 550 °C.[5] Due to the low activity of Ag:SAPO-34 below 250 °C, this makes sense, however Ag^+ exchanged into Cu:SAPO-34 does increase the framework's stability towards hydrolysis at temperatures below 250 °C, as the activity of AgCu:SAPO-34 did not decline as moisture was added into the reaction feed, during NO_x reduction analysis.[5] Botne however experienced an increase of 20 % from Cu:SAPO-34 to AgCu:SAPO-34, where the latter had a conversion of 83 % in a dry feed with 2 % O_2, 2000 ppm NO and 1200 ppm propene.[24] Botne suggested due to the short diffusion length of the species between the Cu^{2+} and Ag^+ sites, a synergestic effect arose contributing to the increased NO_x conversion compared to the Cu:SAPO-34 sample.[24]

According to Delic the simultaneous ion exchange of Ag^+ and Cu^{2+} into Zeolite Y required a molar ratio of 4:1 respectively between them by mass in the solutions, to yield a 1:1 ratio between them of 0.7 wt% inside the zeolite.[78] Botne and Delic both suggested simultaneously exchanged species could take up different positions inside the CHA cage than when ion exchanged singularly.[24, 78]

2.3.5 Mechanically mixed silver and copper containing SAPO-34 in HC-SCR

How well the mechanical mixing of conventional Cu:SAPO-34 and conventional Ag:SAPO-34 performs as a catalyst in the HC-SCR of NO_x, has not been widely explored yet to the best of the author's knowledge. The same applies for the hierarchical version, and these are the 2 explored in this thesis. The separate activities of the copper and silver species in HC-SCR of NO_x discussed in section 2.3.2 and 2.3.3 are in theory combined this way.[24] Here, Cu:SAPO-34 provides NO_2 species for Ag:SAPO-34 to reduce to N_2, where propene will act as reducing agents for the active sites, completing the redox cycle for both metal species.[24, 28] Botne performed HC-SCR of NO_x for these samples in a dry feed, obtaining 25 % conversion at the highest for the hierarchical and 3 % for the conventional.[24] The low conversions were suggested to be most likely due to longer diffusion paths from the copper active sites towards the silver active sites, than with the simultaneously exchanged samples.[24] For the latter both silver and copper species were in theory present inside the same CHA cage, where the conventional AgCu:SAPO-34 sample had a maximum NO_x conversion of 83 %.[24]

Mechanical mixing of different metal containing molecular sieves in general, and how they perform in HC-SCR of NO_x has been explored much more.[26-28, 79-82] A common version explored is for 2 different molecular sieves with differently sized pores (one microporous and the other mesoporous), and containing a different metal specie each.[26-28, 79-82] The strategy is restricting access to the hydrocarbons from being directly oxidized at the oxidizing sites in the micropores but allowing them participation in the reduction of NO_x at the reducing sites in the mesopores.[26-28, 79-82] This strategy is referred to as the dual pore concept, but has not been explored in this thesis.[26-28, 79-82]

Seeing how pores containing active sites can manipulate which reactant species can approach them by the size of their openings, the effect of the size and shape of hydrocarbons in the HC-SCR of NO_x can be investigated. By turning this around, using hydrocarbons of known different size and shape (propene and isobutane in this thesis), the whereabouts of the active sites for the HC-SCR of NO_x inside the SAPO-34 samples can be determined. As such, the HC-SCR of NO_x is used as a model reaction and is described in the section below.

2.3.6 Effect of HC size and shape

From section 2.2, several sources confirm the III position from Figure 2.10 to be the active site for HC-SCR of NO_x, where the Brønsted acid sites in this position are most prone to be exchanged by the Ag^+ and Cu^{2+} species.[2-4, 17, 56-58, 83] Reactant and product species (mainly propene or isobutane, NO, NO_2, CO_2, O_2, N_2 and H_2O) must therefore diffuse in and out respectively of the CHA cage in order to reach the active sites at either the top or bottom of the CHA cage.[2-4, 17, 56-58, 83] All but isobutane are small enough to diffuse in and out through the 8-membered ring opening (3.8 Å), but coking intermediates can also grow too big inside the CHA cage blocking the active sites for further use.[73, 84] Here the 3 described shape selectivities come into play described earlier in section 2.1.2, where the reactants (propene, O_2, NO_x), intermediates (coke, NO_2) and products (CO_2, N_2, H_2O) must pass their respective selectivities of the CHA cage.[12, 32] In this thesis propene was used as hydrocarbon fitting through the pore opening of the CHA cage (Figure 2.12.a).[21, 24, 29] The kinetic diameter of isobutane is 4.9 Å however, so will in theory not be able to reach the known active sites inside the microporous CHA cage (Figure 2.12.b), and reach a conversion of NO_x similar to propene.[85]

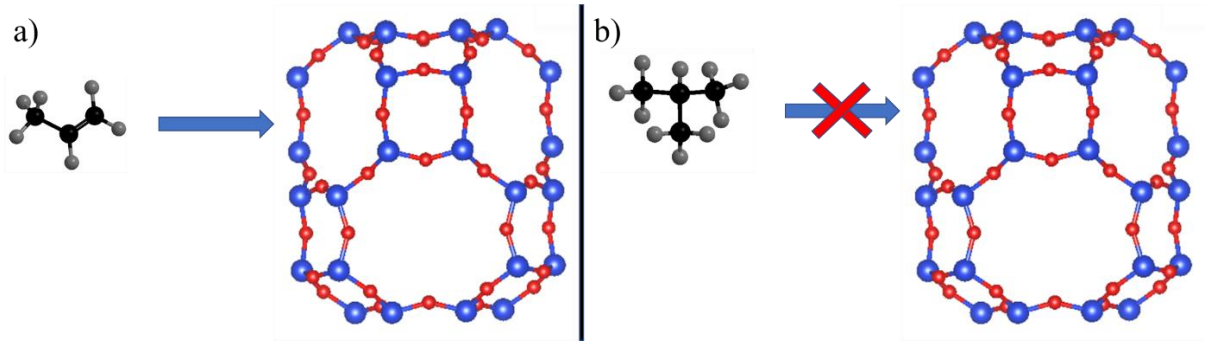

Figure 2.12: a) Propene diffusing into the CHA cage through the 8 membered ring, passing the reactant shape selectivity. b) Isobutane physically unable to diffuse into the CHA cage because of its size, failing the reactant shape selectivity.[35]

The presence of Brønsted acidity inside the micropores is well-established and known.[2-4, 17, 56-58, 83] The degree of Brønsted acidity inside the mesopores and on the external surface of the hierarchical SAPO-34 crystallites however can become clearer using isobutane.[86] Isobutane does fit inside pores of the meso range (> 2 nm and < 50 nm) and the external surface of the crystallites, available to react with the possible active sites present here.[86] Depending on the conversion of NO_x reached with either isobutane or propene, an indication of the number of active sites inside the micropores compared to the mesopores and the external surface of the crystallites can be established.[86] The same applies to the degree of Brønsted acidity on the

external surface of the crystallites for conventional SAPO-34, compared to inside its micropores.

From this section a description of how the HC-SCR of NO_x can be used as a model reaction to characterize the whereabouts of the Brønsted acid sites was given, for both inside the conventional and hierarchical frameworks of SAPO-34. The other characterization techniques used in this thesis are presented in the next section.

2.4 Characterization techniques

Crystallinity, phase purity and type of porosity in the synthesized samples must be confirmed and investigated before ion exchange with Ag^{+} and Cu^{2+}. After ion exchange, the state of these properties must be reconfirmed and the metal content inside the samples must be established, before used in HC-SCR of NO_x. Various characterization techniques confirming these properties are presented below, briefly explaining the property the technique investigates and how it works. Calcination and ion exchange were the major treatments performed on the samples in this thesis, where changes that may follow in their properties are briefly described as well.

2.4.1 Powder X-ray diffraction (XRD)

XRD is a characterization technique used for verifying crystallinity and crystalline phase identity of inorganic materials.[87] In powder XRD, samples contain a large number of randomly oriented crystallites, typically between 0.1 and 10 μm, that are illuminated by x-rays.[87] The many x-rays are diffracted by the sample's crystallites and merge together to form a cone of diffraction, measured by a detector.[87] Peaks with varying intensity will arise with constructive interference at specific incidence angles, resulting in the sample's diffractogram.[87] All crystalline phases have their own unique diffractogram used to verify which phase(s) are present in a sample.[37, 87]

Figure 2.13 presents the diffractogram of the CHA (SAPO-34) and its main competing phase the AFI (SAPO-5) framework.[32] Both the crystallinity and phase purity of a sample has to be verified before further treatment is performed on them.[11] Calcination and ion exchange can have an invasive effect on the structure due to removal of organic templates and the hydrolysis respectively.[2, 3, 17-21] This can lead to a reduction in crystallinity and change in phase purity of the samples, so the presence of these properties must be reconfirmed after each treatment.[87] The hierarchical and conventional samples will have the same diffractograms, so the presence of mesopores cannot be confirmed with this technique.[37]

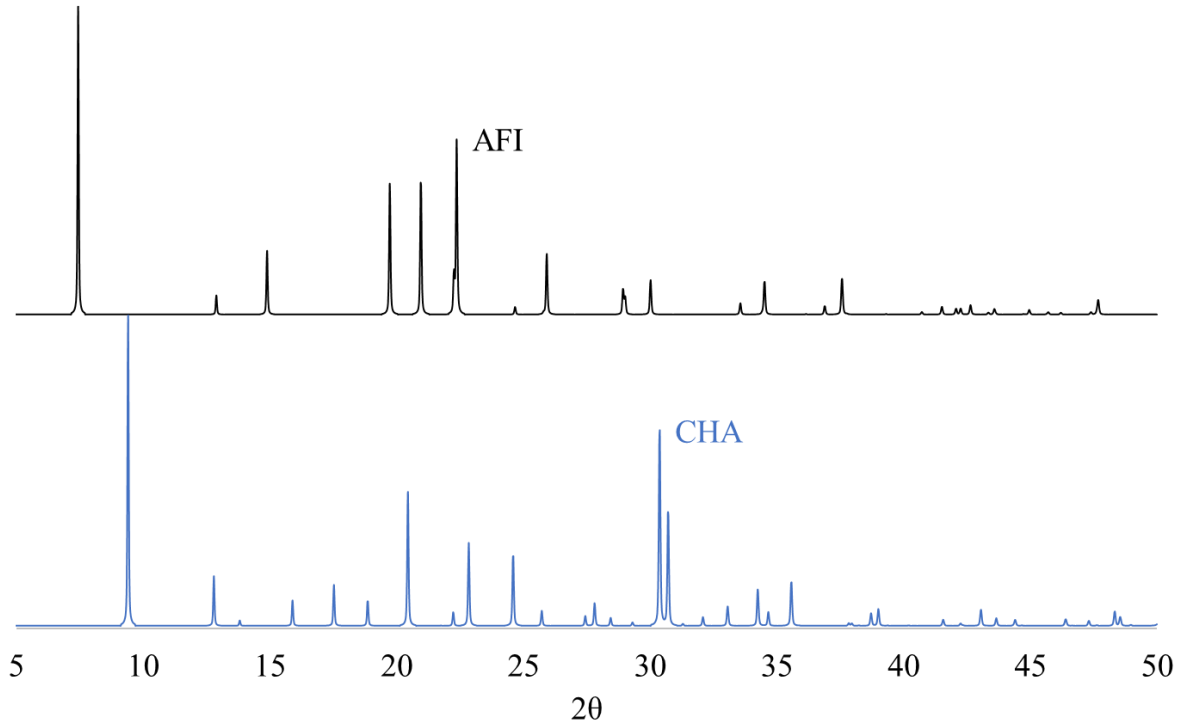

Figure 2.13: Powder x-ray diffractograms of the CHA and AFI frameworks.[32]

2.4.2 BET and BJH analysis

BET analysis measures the multilayer adsorption of nitrogen (N_2) as a function of relative pressure (P/P_o), providing a precise specific surface area evaluation.[88] Both external and pore surface area and volume are evaluated providing values for the total specific surface area and pore volume per gram of a sample.[88] The isothermal adsorption curve is one of the results of the analysis where depending on its shape, information about the pore size range and shape is found by comparing it with the different possible adsorption isotherms (Figure 2.14 and 2.15).[89-91] For conventional SAPO-34 the type I adsorption isotherm for microporous materials is expected while for hierarchical SAPO-34, the type IV adsorption isotherm with hysteresis indicating mesoporosity is expected (Figure 2.14). Figure 2.15 presents the possible type IV hysteresis isotherm shapes and their corresponding pore shapes.[89-91] BJH analysis determines pore specific surface area and specific pore volume by adsorption and desorption of nitrogen, characterizing the pore size distribution (PSD) of the sample independent of external area due to the sample's particle size.[88]

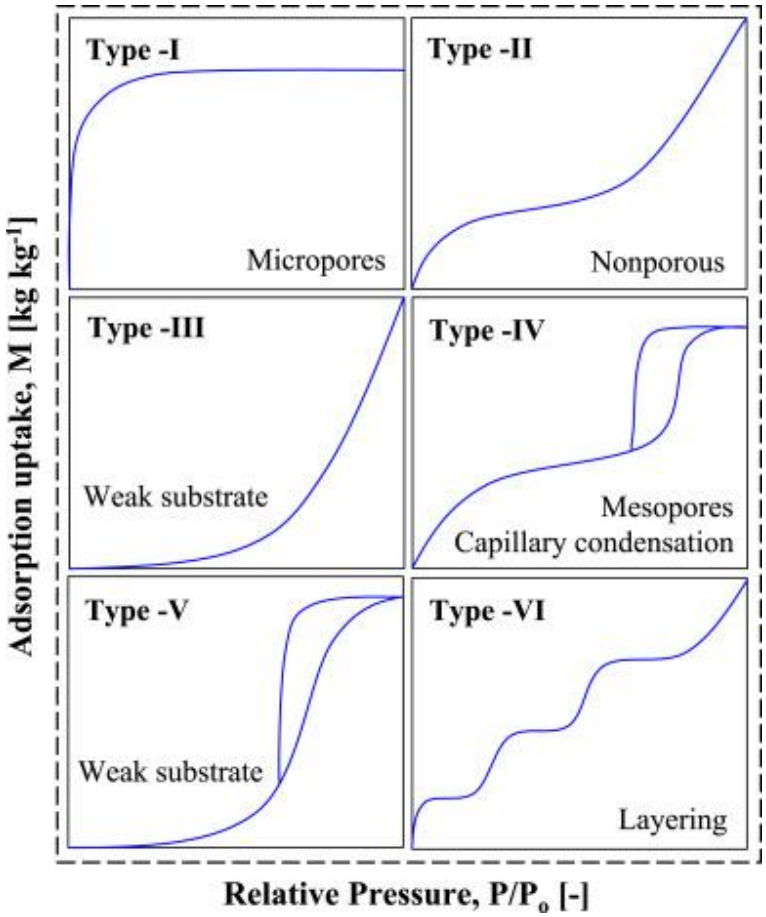

Figure 2.14: Types of adsorption isotherms possible depending on the material's porosity. Reused with permission from Elsevier.[89-91]

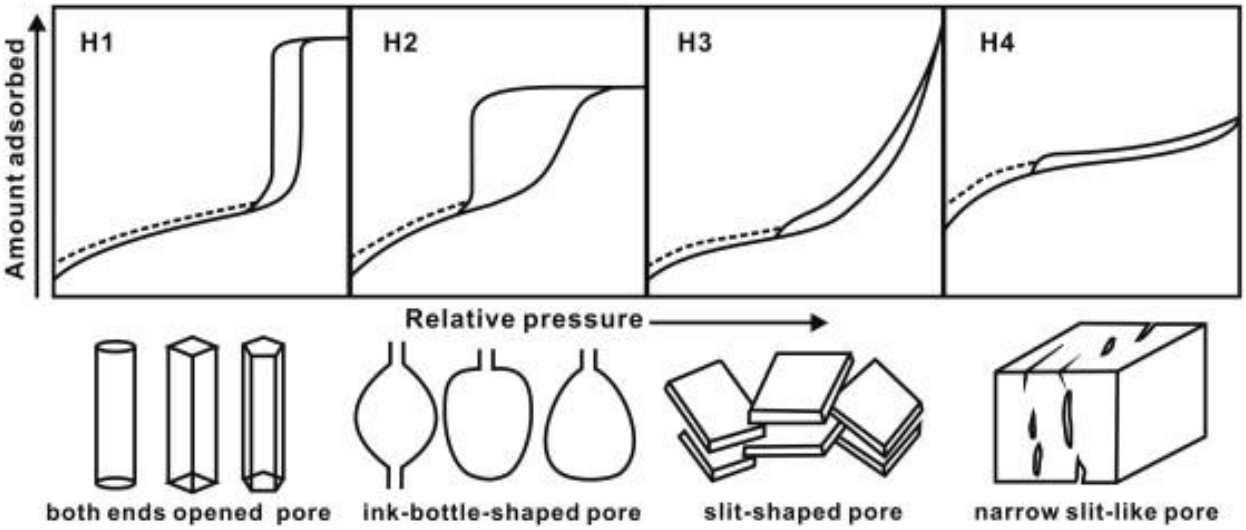

Figure 2.15: Different possible type IV hysteresis curves depending on the pore shape of the material. Reused with permission from Elsevier.[89-91]

2.4.3 Inductively coupled plasma mass spectrometry (ICP-MS)

ICP-MS is a widely used technique, able to accurately determine the elemental composition of a sample for over 70 elements in a few minutes.[92] An inductively coupled plasma composed of high temperature argon ions serves as an ionizer for the elements present in a sample.[92, 93] The ionized elements of the sample are then separated by their mass to charge (m/z) ratio by a quadrupole before being detected by the mass spectrometer.[92] In this thesis ICP-MS is used to determine silver and copper content (weight percentage (wt%)) inside the ion exchanged samples.

2.4.5 Scanning electron microscopy (SEM)

To get a first-hand visual look on the particle sizes and shapes of the synthesized samples that are used for the catalytic analysis, SEM is employed. In SEM a high energy beam of electrons accelerated by a voltage, bombard and penetrate a sample by a few microns, producing secondary and backscattered electrons and characteristic x-rays.[94] These are collected by various detectors and produce images of the sample.[94] Depending on the shape, size and degree of agglomeration of the particles, an impression on whether specific surface area other than the microporous part is external or mesoporous can be made.

3.0 Experimental

The following section starts by introducing the synthesis route used for both conventional and hierarchical SAPO-34, and variation of parameters to study what results in phase pure samples. A description of the two-step ion exchange method used on the phase pure samples, and the characterization instruments to confirm their crystallinity, porosity and metal content follows. Finally, the method for sample preparation and catalytic testing along with the instrumental setup to measure NO_x conversion is presented.

3.1 Synthesis of SAPO-34

Synthesis of SAPO-34 was done hydrothermally, illustrated in Figure 3.1 and inspired by Askari and Tafjord et al. among others.[11, 95] LUDOX colloidal silica (40 wt%, SiO_2, Sigma Aldrich) was used as silicon source. Orthophosphoric acid (85 wt%, H_3PO_4, Merck) was used as phosphorus source. Pseudo-boehmite (P-B) (71.8 wt%, AlO(OH) (assumed Al_2O_3), Sasol North America) or aluminium-isopropoxide (A-I) (98 wt%, $AlO_3C_9H_{21}$, Sigma Aldrich) were used as aluminium sources. Water was used as continuous medium and mineralizing agent. Both Triethylamine (TEA) (NC_6H_{15}, Acros Organics) and Tetraethyl ammonium hydroxide (TEAOH) ($NC_8H_{20}OH$, 40 wt%, Sigma Aldrich) or only TEAOH were used as micro-SDAs for both conventional and hierarchical SAPO-34. Pluronic F127 (HO-$(C_2H_4O)_{100}(C_2H_3OH)_{65}(C_2H_4)_{100}$-H, Sigma Aldrich) or TPOAc (42 wt% in methanol, $C_{26}H_{58}ClNO_3Si$, Sigma Aldrich) were used as meso-SDAs for hierarchical SAPO-34.

A stepwise method was used to produce the synthesis gel, illustrated in Figure 3.1. Here, the synthesis gel was stirred continuously as each component was added. After adding a new component, the gel was left to stir for ½ h, before a new component was added. The addition order of components was water and orthophosphoric acid, the aluminium source, the silicon source, the micro-SDAs and finally the meso-SDAs (in the case of hierarchical SAPO-34). When all components were added, the gel continued to stir until homogeneous and was transferred to the Teflon liner of the autoclave up to 2/3 of the liner's volume. The liner was sealed inside the autoclave's metal jacket and placed inside an oven, crystallising at temperatures of 170 – 190 °C for 24 – 72 h.

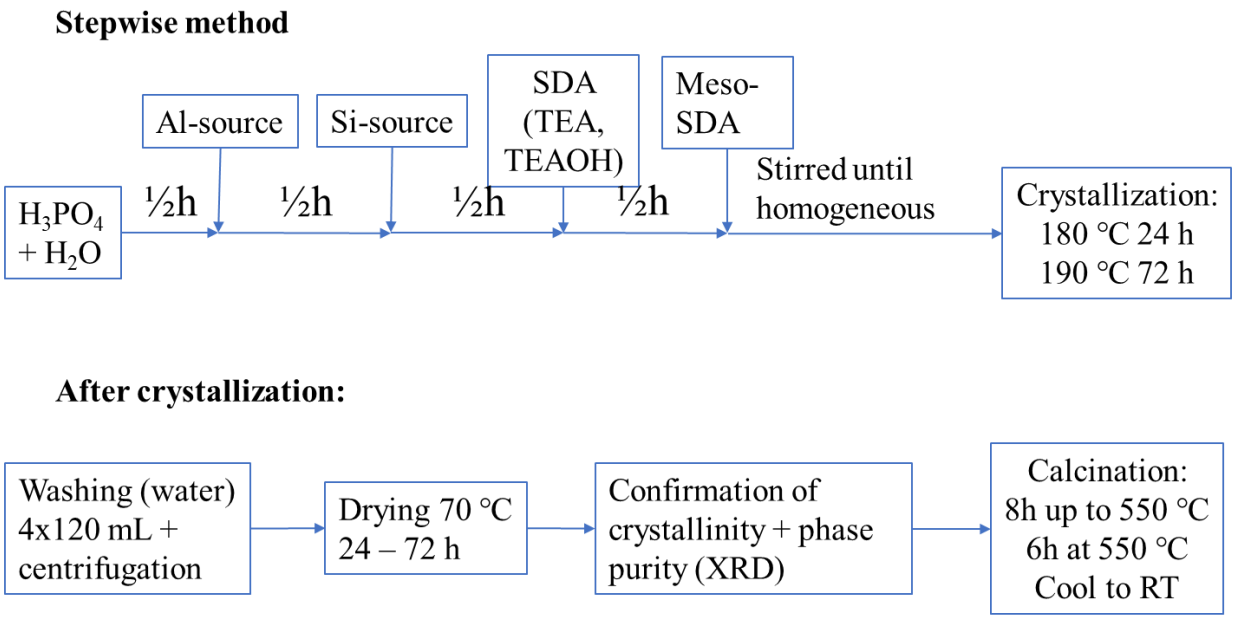

Figure 3.1: Synthesis route for SAPO-34 describing the individual steps chronologically, from gel production to calcination of crystalline and phase pure samples

Table 3-1 and 3-2 present the synthesis conditions and component molar ratios used for the as prepared (AP) conventional and hierarchical samples in this thesis.

Table 3-1: Overview of synthesis conditions and component molar ratios used for the conventional SAPO-34 syntheses. The red row presents the sample acting as a basis for the other samples, where one condition is varied at a time. The cell presenting the changed condition is coloured blue. The last 2 samples use a different aluminium source, and here several conditions are changed.

Sample	H_2O	P	Al	Si	TEA	TEAOH	Dur. (h)	Temp. (C°)
C-24h P-B	24	1	1 P-B	0.5	1	0.1	24	180
C-48h P-B	24	1	1 P-B	0.5	1	0.1	48	180
C-20h	24	1	1 P-B	0.5	1	0.1	20	180
C-170 °C	24	1	1 P-B	0.5	1	0.1	24	170
C-0.3Si A-I	28	1	1 A-I	0.3	0	0.9	72	190
C-0.5Si A-I	28	1	1 A-I	0.5	0	0.9	72	190

Table 3-2: Overview of synthesis conditions and component molar ratios used for the hierarchical SAPO-34 syntheses. The red row presents the sample acting as a basis for the other samples, where one condition is varied at a time. The cell presenting the changed condition is coloured blue. The last 2 samples use a different aluminium source, and here several conditions are changed.

Sample	H_2O	P	Al	Si	TEA	TEAOH	F127	TPOAc	Dur. (h)	Temp. (C°)
H-24h P-B	24	1	1 P-B	0.5	1	0.1	$4*10^{-5}$	-	24	180
H-48h P-B	24	1	1 P-B	0.5	1	0.1	$4*10^{-5}$	-	48	180
H-1g F127	24	1	1 P-B	0.5	1	0.1	$8*10^{-5}$	-	24	180
H-2g F127	24	1	1 P-B	0.5	1	0.1	$16*10^{-5}$	-	24	180
H-3g F127	24	1	1 P-B	0.5	1	0.1	$24*10^{-5}$	-	24	180
H-4g F127	24	1	1 P-B	0.5	1	0.1	$32*10^{-5}$	-	24	180
H-0.1Si P-B	24	1	1 P-B	0.1	1	0.1	$4*10^{-5}$	-	24	180
H-0.3Si P-B	24	1	1 P-B	0.3	1	0.1	$4*10^{-5}$	-	24	180
H-0.4Si P-B	24	1	1 P-B	0.4	1	0.1	$4*10^{-5}$	-	24	180
H-TPOAc	24	1	1 P-B	0.5	1	0.1	-	0.05	24	180
H-0.3Si A-I	28	1	1 A-I	0.3	0	0.9	$4*10^{-5}$	-	72	190
H-0.5Si A-I	28	1	1 A-I	0.5	0	0.9	$4*10^{-5}$	-	72	190

After crystallization, the samples were extracted, washed and centrifuged with distilled water until the wash water was clear and transparent (ca. 4 times) and dried at 70 °C for 24 h – 72 h. The samples were calcined in air at 550 °C for 6 h using a ramp rate of 65.6 °C h^{-1} from room temperature. The samples were left to cool to room temperature afterwards at ambient conditions.

3.2 Ion exchange of SAPO-34

For ion exchange of the synthesized SAPO-34 samples, the two-step ion exchange method from section 2.2.2 was employed, shown in Figure 3.2. In the first step, the samples were ion exchanged with ammonium (NH_4^+) in 0.1 M ammonium nitrate (NH_4NO_3, Sigma Aldrich) solution, for 2 h at 80 °C. Here, $5.4*10^{-3}$ mol NH_4^+ per gram SAPO-34 sample was used. The ion exchanged powder was extracted, washed and centrifuged with distilled water, until the wash water was clear and transparent (ca. 3 – 4 times) and dried at 70 °C for 24 h – 72 h.

For the second step, the NH_4^+:SAPO-34 samples were divided in 3 batches. One batch was ion exchanged with 0.134 M copper nitrate ($Cu(NO_3)_2x3H_2O$, Sigma Aldrich) solution. Another batch was ion exchanged with 0.134 M silver nitrate ($AgNO_3$, VWR Chemicals) solution. The last batch was ion exchanged with both solutions simultaneously. Each batch was ion exchanged for 2 h at 80 °C, and washed and dried as described above.

Ion exchange temperature and duration for both steps were inspired by the NH_4NO_3 ion exchange performed by Xu et al.[20] Xu et al. however, performed 2 rounds of ion exchange of 1 h each with 1.0 M NH_4NO_3 at 80 °C, with washing and drying between the rounds.[20] The concentrations for the Ag^+ and Cu^{2+} solutions were the same as Delic used for ion exchange with Ag^+ and Cu^{2+}.[78] For ion exchange with only Ag^+ or Cu^{2+}, $5.4*10^{-3}$ mol cations per gram SAPO-34 sample was used. For simultaneous ion exchange, $1.08*10^{-3}$ mol Cu^{2+} and $4.32*10^{-3}$ mol Ag^+ per gram SAPO-34 sample was used. These values were derived from Delic, resulting in ca. 40 mL solution per gram sample.[78]

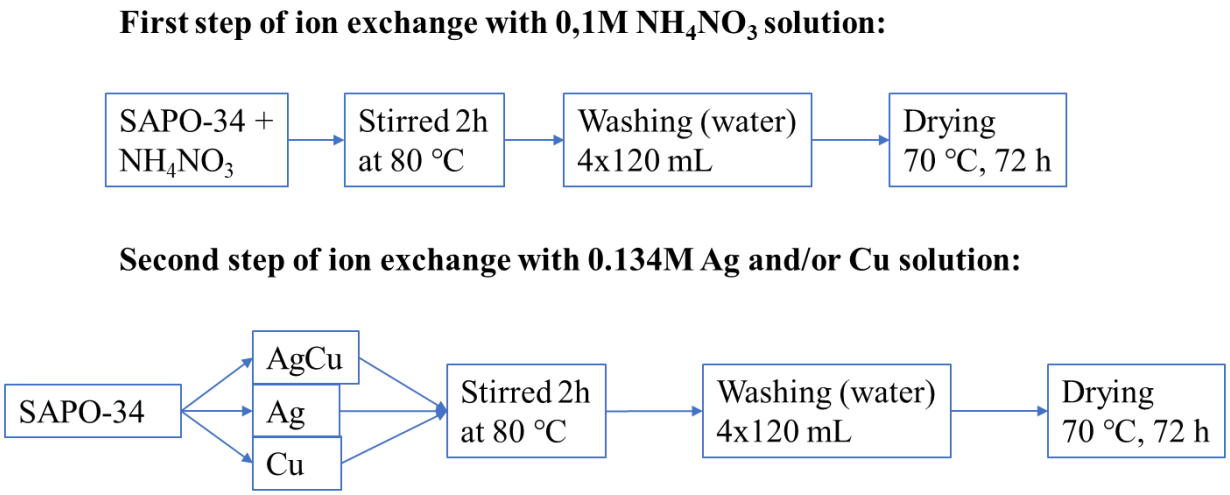

Figure 3.2: Overview of the two-step ion exchange method

The samples H-0.5Si A-I and C-0.5Si A-I were used for NO_x conversion analysis described in section 3.7. Here the samples underwent the analysis after 1 round of ion exchange and 4 rounds of ion exchange. For the 4 rounds of ion exchange, 3 additional ion exchange rounds were performed on the samples just like the first round with $Ag(NO_3)$ and/or $Cu(NO_3)_2$ as explained above.

3.3 Powder XRD instrumentation

For powder XRD, a Bruker D8 A25 DaVinci X-ray Diffractometer with CuKα radiation and a LynxEye™ SuperSpeed Detector was used. The divergence slit opened automatically keeping a length of 6 mm constantly illuminated on the sample. From here, a program of 15 minutes was performed on the samples, where the range of 2θ values scanned was between 5 degrees and 60 degrees, with a step size of ca. 0.013 °/step. Standard sample holders of diameter Ø 25 mm and Ø 10 mm, and height 8.5 mm were used for the XRD diffractograms.[96]

3.4 BET instrumentation

For isotherm N_2 adsorption analysis, a sample was first weighed out (160 mg). Then, a Micromeritics Tri Star 3000 Degas sample dryer was used to remove adsorbed species from the samples' surface overnight (18 h) by vacuum. A Micromeritics Tri Star 3000 Surface Area and Porosity Analyzer was then used for adsorption measurements, using N_2 as adsorptive gas. The instrument was fully automated and provided an N_2 adsorption isotherm, total specific pore surface area and volume and pore size distribution (PSD).[97]

3.5 ICP-MS instrumentation

All samples were decomposed before analyzed by the instrument. Each sample was weighed out (30 mg – 50 mg) and transferred to a Teflon tube (25 mL). Concentrated nitric acid (1.5 mL) and hydrofluoric acid (40 %, 0.5 g) was added to the samples and left for 1 h to decompose. The decomposed samples were diluted with deionized water up to 213 g – 240 g in a larger Teflon container. Teflon tubes (16 mL) containing the diluted samples during the elemental analysis were first rinsed 3 times with the diluted samples, before filled a fourth time with the sample for analysis. 3 blank samples were run in addition to the actual samples in order to eliminate the background noise.

Syverin Lierhagen (IKJ) was responsible for performing elemental analysis at the department of chemistry (IKJ), and used an Agilent - 8800 ICP-MS Triple Quad to verify the metal content in the ion exchanged samples.

3.6 SEM images

SEM images were taken of the phase pure samples used for NO_x analysis, to get a visual impression of the particle shapes, particle size (PS) and particle size distribution. SEM images were taken by Daniel Ali (IKJ) using a Hitachi S-3400N. Gold was vapor deposited for approximately 2 minutes at 0.15 atm using an Edwards Sputter Coater (S150B) running at a current and voltage of 20 mA and 2.0 kV respectively. Gold vapor deposition was performed to avoid charging effects and for sharp images.

3.7 Catalysis

This section starts with a description of the instrumental set-up for the NO_x conversion analysis, and conditions used. A description of the sample preparation follows, and after this the implementation of the reaction itself with the temperature program used. A description of the NO_x conversion calculation and how the bypass NO ppm value varies and can be modelled through the duration of the reaction, is provided in Appendix F: NO_x conversion calculation.

3.7.1 Instrumentation for catalytic measurement

In this project, the instrumental setup for measuring the change in NO_x concentration was almost identical to the setup used by Botne.[24] This project used a wet feed instead of a dry one, and used either propene or isobutane as hydrocarbons (HC) for HC-SCR of NO_x. All gases used during catalytic testing were provided by AGA, consisting of NO (1 vol% in He), O_2 (10 vol% in He), propene (2 vol% in He), isobutane (2 vol% in He) and argon. Water was included in the feed (10 vol%) by keeping it constantly at 47 °C and bubbling argon gas through it, before the gas mixture entered the reactor tube as illustrated in Figure 3.3. A CLD 62 Eco-Physics Chemiluminescence NO/NO_x Analyzer was used for detecting NO_x concentration changes. Water was removed from the feed before it entered the analyser. A Nabertherm R50/250/12 tube furnace with a C450 controller was used for the temperature program described and illustrated in section 3.7.3.[24]

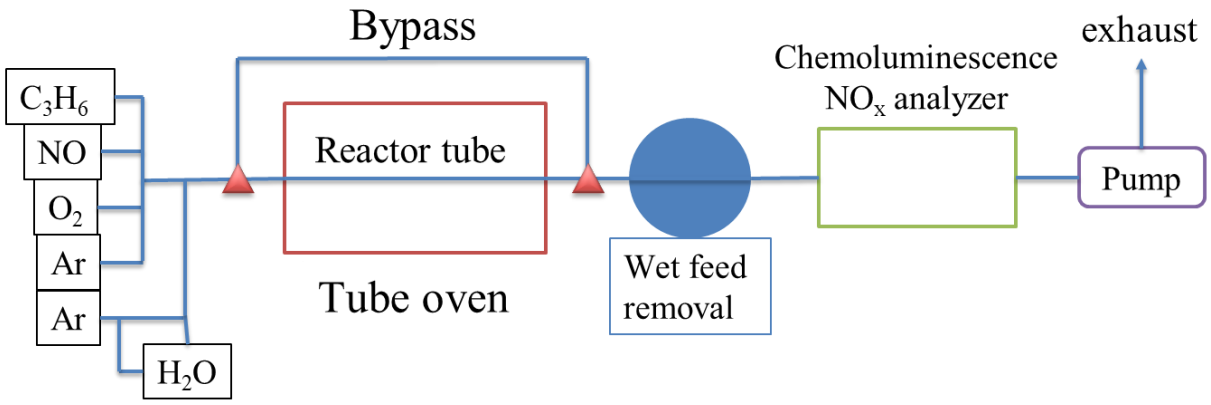

Figure 3.3: Schematic of the instrumental setup for the catalytic measurement of NO_x conversion

3.7.2 Sample preparation

For the catalytic measurement, the conventional and hierarchical Ag:SAPO-34, Cu:SAPO-34 and AgCu:SAPO-34 samples were pressed to a pellet, ground down in size by mortar and pestle, and finally sieved so that the particle size of each sample was between 212 µm and 425 µm. 120 mg of each sample was weighed out and used for catalytic measurement (Figure 3.4). In the case of mechanically mixing Ag:SAPO-34 and Cu:SAPO-34, 100 mg of each was weighed out and mixed thoroughly by mortar and pestle before being prepared identically as the unmixed samples for catalytic measurement. The prepared samples were situated in the middle of the reactor tube and fixed in place by quartz wool from both ends of the reactor tube (Figure 3.4).

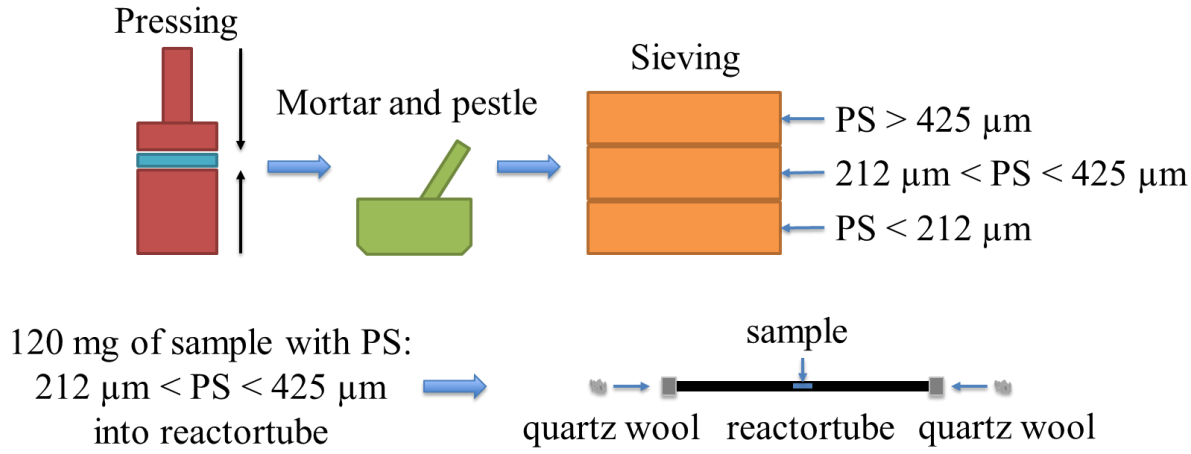

Figure 3.4: Sample preparation for catalytic measurement. The sample powder was pressed, ground and sieved until 120 mg of the sample in the desired particle size range was produced. The sample was then fixed in the middle of the reactor tube with quartz wool from both ends.

3.7.3 Catalytic measurement

Figure 3.5 illustrates the temperature programme used for the catalytic measurement of the samples' catalytic activity of NO_x conversion, mirroring the work of Botne (except for additional wet feed).[24] Only NO_x conversion was measurable with the instruments used, not the selectivity towards N_2.[24] First, the sample was heated to 500 °C overnight, before activated in 2 vol% O_2 balanced in Ar for 60 minutes, in a total gas feed of 80 mL/min.[62] For the catalytic measurement, the total gas feed of 140 mL/min consisted of 2 vol% O_2, 2000 ppm NO and 1200 ppm propene or isobutane, all balanced in Ar. Ar also bubbled through water kept constantly at 47 °C, for a wet feed (10 vol%).[25] This gas mixture was first led through the bypass tube (Figure 3.3), until the ppm value of NO stabilized, verifying a stable concentration of NO at the starting temperature of 500 °C.

After the stabilization of NO at 500 °C, the ppm value was registered as the BypassStartvalue explained in Appendix F: NO_x conversion calculation, before the gas flow was turned on the reactor tube. NO ppm values were then measured for 20 minutes at constant temperature values, with 25 °C intervals from 500 °C – 275 °C, including 500 °C and 275 °C, as illustrated in Figure 3.5. The last NO ppm value for each temperature was taken as the representative value, as the value was considered stable at this point, and used for calculating the NO_x conversion ability of the sample at that temperature. Halfway in the temperature programme at 400 °C, the gas feed was turned on the bypass for 20 min until the NO ppm value stabilized and was registered. Afterwards the gas feed was turned on the reactor tube again, and the catalytic measurement continued towards the end of the temperature program. Appendix F: NO_x conversion calculation, further describes why this halfway bypass measurement was registered. Three bypass measurements were performed through the temperature program where the green and red striped lines in Figure 3.5 mark the beginning and end respectively of these measurements for all 3 times. The bypass value was given 20 minutes for stabilization for all 3 times, and the value at the end of the 20 minute interval (red striped line) was the registered bypass value. In Appendix F: NO_x conversion calculation, the weighted bypass method Botne used for finding the NO_x conversion is further described. Here, a method for modelling the bypass value during the temperature program using the 3 bypass measurements is provided as well.

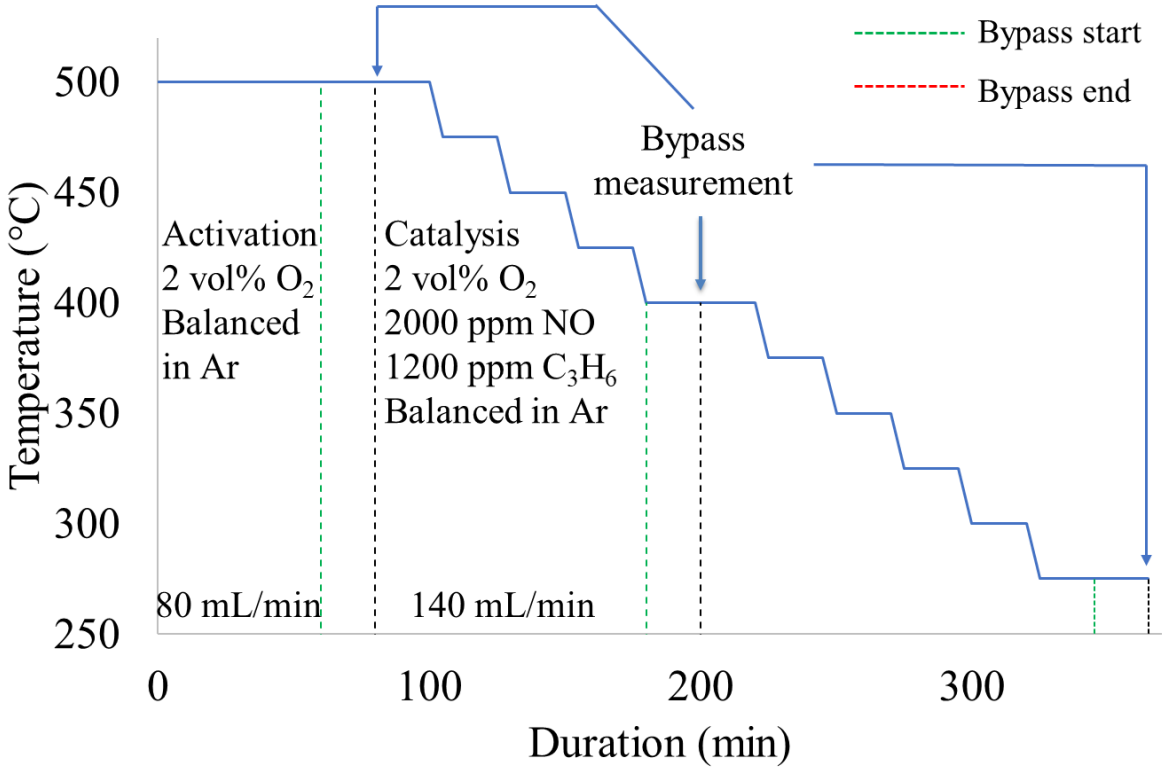

Figure 3.5: Temperature programme performed by the Nabertherm R50/250/12 tube furnace, and gas feed composition before and during catalytic measurement. A bypass measurement was performed at 500 °C, halfway in the temperature programme at 400 °C, and at the end at 275 °C. The green striped line marks the point in time where the gas feed was turned on the bypass tube, and the black striped line where it was turned back on the reactor tube. The correct bypass value was at the black striped line, where the NO_x ppm value had stabilized.

4.0 Results

This section presents relevant results for whether the goals of synthesizing phase pure conventional and hierarchical SAPO-34 were obtained, and if their structure survived the two-step ion exchange method. The metal content along with the performance of the samples in the HC-SCR of NO_x using propene and isobutane as hydrocarbons in a wet feed is presented afterwards.

4.1 Confirming phase purity of the samples

In total there were 6 samples without meso-SDA and 12 samples with meso-SDA synthesized (Table 4-1), where the variations in molar ratio and synthesis conditions used and their respective XRD results are presented below. Molar ratios of aluminium (Al) and phosphorus (P) were 1 in terms of the numbers for the other species (Table 4-1), and aluminium sources used were pseudo boehmite (P-B) or aluminium isopropoxide (A-I).

Table 4-1: Overview of molar ratios and synthesis conditions used for the synthesized samples. Conventional samples are shown first and hierarchical ones after. Aluminium sources used were pseudo boehmite (P-B) and aluminium isopropoxide (A-I). Phase pure samples are the green highlighted rows.

Sample	H_2O	Al	Si	TEA	TEAOH	F127	TPOAc	Dur. (h)	T (°C)	XRD
C-24h P-B	24	P-B	0.5	1	0.1	0	0	24	180	CHA
C-48h P-B	24	P-B	0.5	1	0.1	0	0	48	180	CHA, AFI
C-20h	24	P-B	0.5	1	0.1	0	0	20	180	CHA, AFI
C-170 °C	24	P-B	0.5	1	0.1	0	0	24	170	CHA, AFI
C-0.3Si A-I	28	A-I	0.3	0	0.9	0	0	72	190	CHA
C-0.5Si A-I	28	A-I	0.5	0	0.9	0	0	72	190	CHA
H-24h P-B	24	P-B	0.5	1	0.1	$4*10^{-5}$	0	24	180	CHA
H-48h P-B	24	P-B	0.5	1	0.1	$4*10^{-5}$	0	48	180	CHA, AFI
H-1g F127	24	P-B	0.5	1	0.1	$8*10^{-5}$	0	24	180	CHA
H-2g F127	24	P-B	0.5	1	0.1	$16*10^{-5}$	0	24	180	CHA, AFI
H-3g F127	24	P-B	0.5	1	0.1	$24*10^{-5}$	0	24	180	CHA, AFI
H-4g F127	24	P-B	0.5	1	0.1	$32*10^{-5}$	0	24	180	CHA, AFI
H-0.1Si P-B	24	P-B	0.1	1	0.1	$4*10^{-5}$	0	24	180	CHA
H-0.3Si P-B	24	P-B	0.3	1	0.1	$4*10^{-5}$	0	24	180	CHA
H-0.4Si P-B	24	P-B	0.4	1	0.1	$4*10^{-5}$	0	24	180	CHA, AFI
H-TPOAc	24	P-B	0.5	1	0.1	0	0.05	24	180	CHA, AFI
H-0.3Si A-I	28	A-I	0.3	0	0.9	$4*10^{-5}$	0	72	190	CHA
H-0.5Si A-I	28	A-I	0.5	0	0.9	$4*10^{-5}$	0	72	190	CHA

Nine out of the 18 samples were deemed phase pure SAPO-34 (only CHA) based on their x-ray diffraction (XRD) results (Figure 4.1 and Appendix A: Additional XRD results) and highlighted in green (Table 4-1).[32] All samples using aluminium isopropoxide as aluminium

source (4 samples) became phase pure SAPO-34 (C-0.3Si A-I, C-0.5Si A-I, H-0.3Si A-I and H-0.5Si A-I from Table 4-1). Aluminium isopropoxide is an organic aluminium source stated to favour SAPO-34 formation more than inorganic sources according to Emrani et al. due to more homogeneous aluminium precursor distribution.[44] Using pseudo boehmite (inorganic source) as aluminium source resulted in both CHA and CHA+AFI in the resulting samples, further supporting Emrani et al.'s statement. From here the H-0.5Si A-I and C-0.5Si A-I samples (Table 4-1), referred to as Hier and Conv in the Figures of section 4, were chosen for further investigation of porosity, survival of ion exchange and used in the HC-SCR of NO_x.

XRD was used to verify the phases present in the synthesized samples by matching their diffractograms with those of known phases, and to confirm their crystallinity (sharp defined peaks on specific values of the incidence angle θ as in Figure 2.13).[37] Diffractograms of samples matching that of the CHA phase were confirmed as phase pure SAPO-34. The XRD results of the "as prepared" (AP) phase pure H-0.5Si A-I (Hier-AP) and C-0.5Si A-I (Conv-AP) state are stacked in Figure 4.1, above the theoretical diffractogram of the CHA phase.[32] The highest peak of the hierarchical sample in Figure 4.1 is 22 % higher than the same peak for the Conv sample.[32] Clear (tall and narrow) diffraction peaks can mean more long-range order according to Chorkendorff et al., indicating larger crystallites for H-0.5Si A-I than C-0.5Si A-I.[37] This is later confirmed by the obtained scanning electron microscopy (SEM) results in the next section. BET results for the H-0.5Si A-I and C-0.5Si A-I samples' porosity are first presented in the next section, to see if they were hierarchical and conventional respectively.

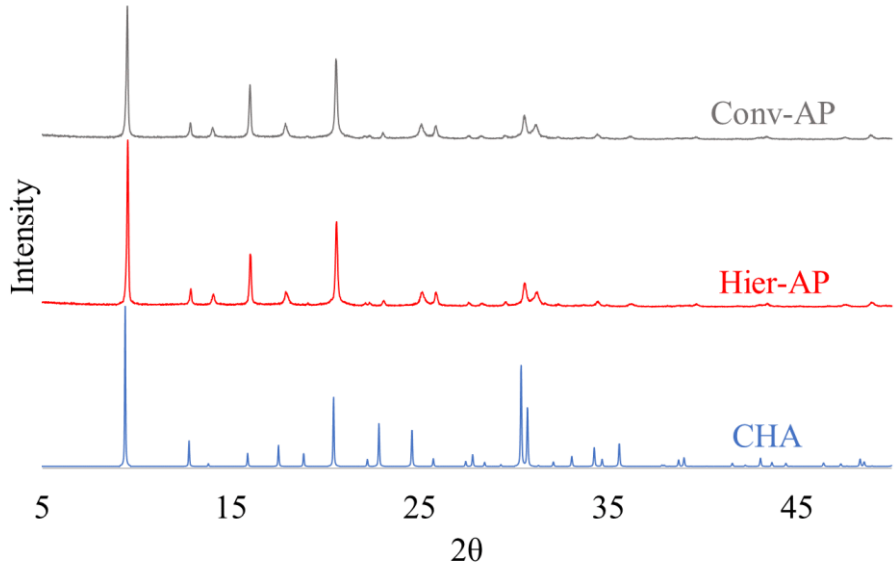

Figure 4.1: Powder XRD diffractogram of the stacked diffractograms of the 2 "as prepared" samples Hier-AP and Conv-AP along with the diffractogram of the chabazite (CHA) structure.[32]

4.2 Investigating the porosity

Brunauer Emmett Teller – Barrett Joyner Halenda (BET-BJH) theory was the main technique and scanning electron microscopy (SEM) an additional technique used for characterizing the porosity of the samples.

Figure 4.2 presents the BET results of the calcined (C) H-0.5Si A-I and C-0.5Si A-I samples (Hier-C and Conv-C). Figure 4.2.a shows their stacked adsorption isotherm curves, where they have similar shaped curves with hysteresis, like the type IV adsorption isotherm (Figure 2.14). This was expected for H-0.5Si A-I with added meso-SDA, but for C-0.5Si A-I where no meso-SDA was added, the type I adsorption isotherm for microporous materials (Figure 2.14) was expected. Both curves have a mixture of H3 and H4 type of hysteresis shown in Figure 2.15, suggesting apparent mesopores present without a defined pore size.[89-91] From the pore size distribution (PSD) (Figure 4.2.c), there is no sharp peak suggesting a specific mesopore size representing the mesopore size for the samples either, but the average pore widths of the apparent mesopores for the hierarchical and conventional samples were 23.82 Å and 25.32 Å respectively.

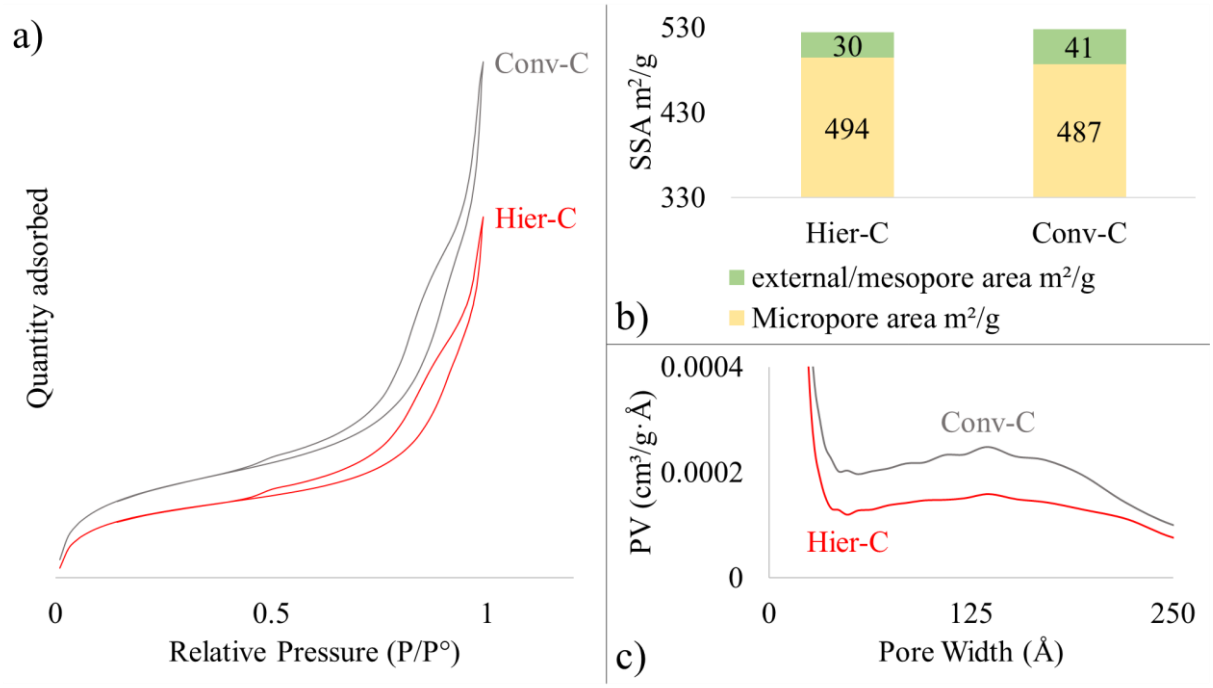

Figure 4.2: a) Stacked adsorption isotherms for the calcined H-0.5Si A-I and C-0.5Si A-I samples. b) Specific surface area (SSA) of the samples distributed between microporous (yellow) and external/mesoporous (green) surface area. c) Pore size distribution (PSD) of the samples showing how much pore volume (PV) was occupied for the specific pore widths.

Figure 4.2.b presents the specific surface area (SSA) of the samples, distributed between microporous (yellow) and external/mesoporous area (green). The total area was very similar for both samples, 524 m^2/g and 528 m^2/g for H-0.5Si A-I and C-0.5Si A-I respectively, and very close to the theoretical value of 550 m^2/g, reported by ACS materials.[36] Microporous and external/mesoporous volume was 0.253 cm^3/g and 0.059 cm^3/g respectively and 0.312 cm^3/g in total for H-0.5Si A-I. For C-0.5Si A-I the same values were 0.249 cm^3/g, 0.085 cm^3/g and 0.334 cm^3/g in total. Both total pore volumes were above the reported theoretical value of 0.27 g/cm^3.[36]

The same BET results (adsorption isotherms, total specific surface area, pore volume and pore size distribution) of all the other samples in Table 4-1 are given in Appendix B: Additional BET results.

Scanning electron microscopy (SEM) images of the calcined H-0.5Si A-I and C-0.5Si A-I samples below (Figure 4.3 and 4.4) illustrate the samples from a-d zooming out.

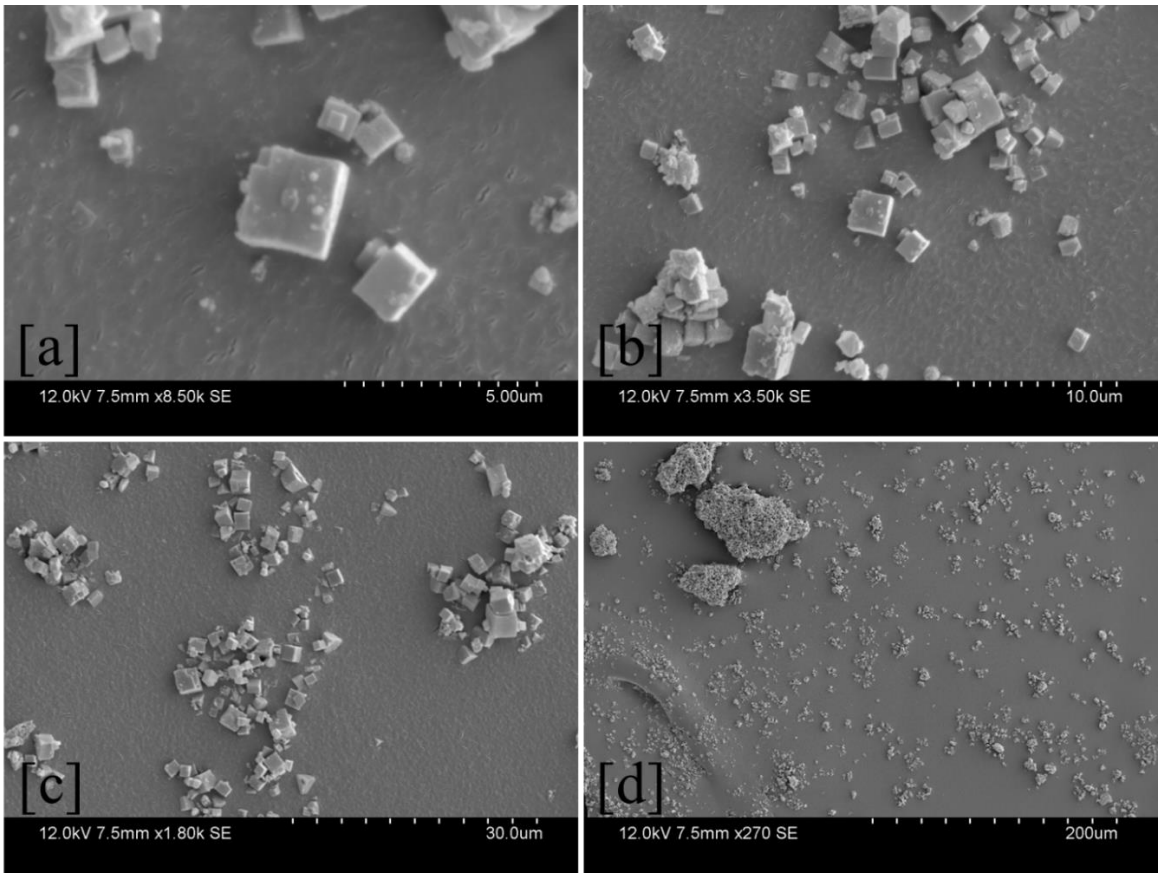

Figure 4.3: SEM images of calcinated H-0.5Si A-I, zooming out from a-d.

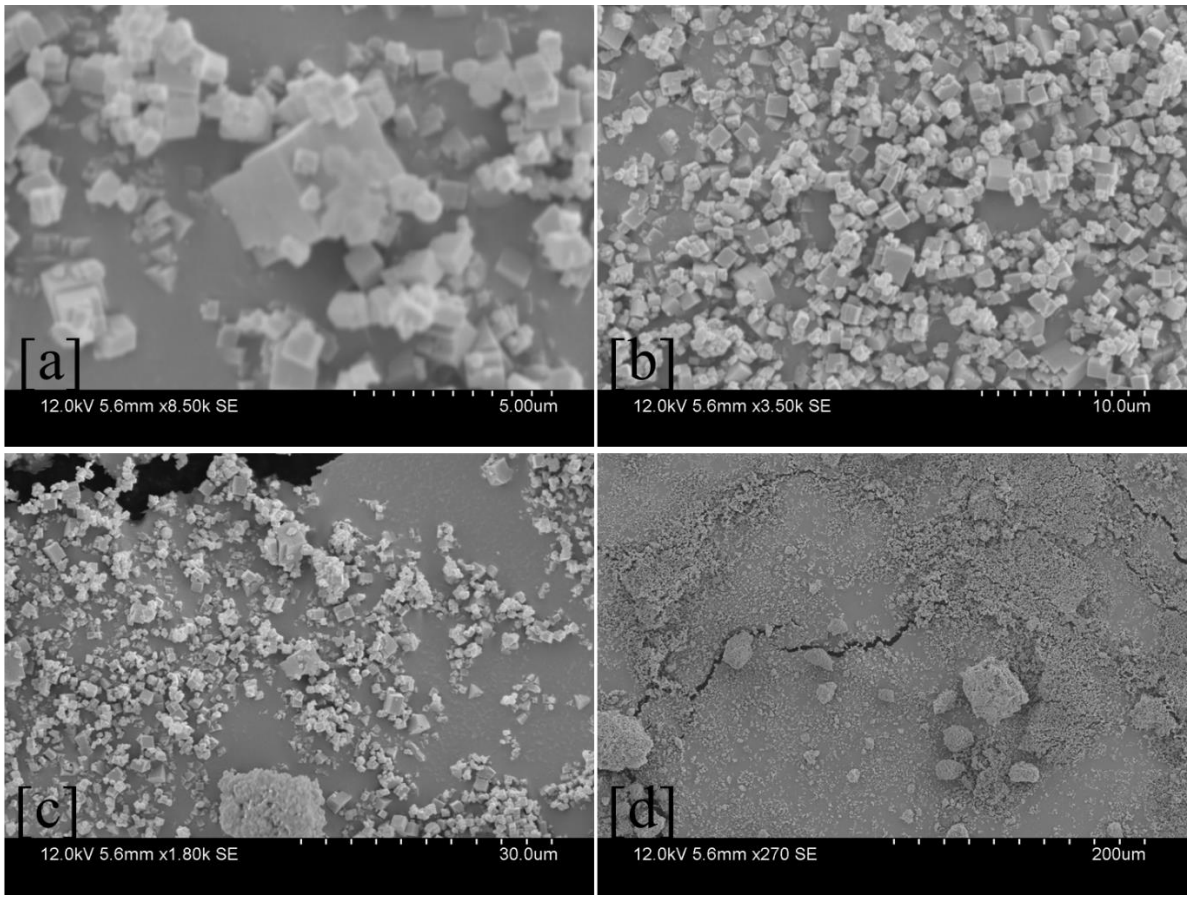

Figure 4.4: SEM images of calcinated C-0.5Si A-I, zooming out from a-d.

The particle size distribution of the 2 samples based upon their SEM images (Figure 4.3 and 4.4) are shown below (Figure 4.5 and 4.6 respectively). The conventional sample has a narrow particle size distribution with few diameters occurring frequently and an average particle size of 1.4 µm. The hierarchical sample has a broader particle size distribution with several different diameters occurring less frequently, and a larger average particle size of 2.7 µm, 2 times bigger than the conventional sample.

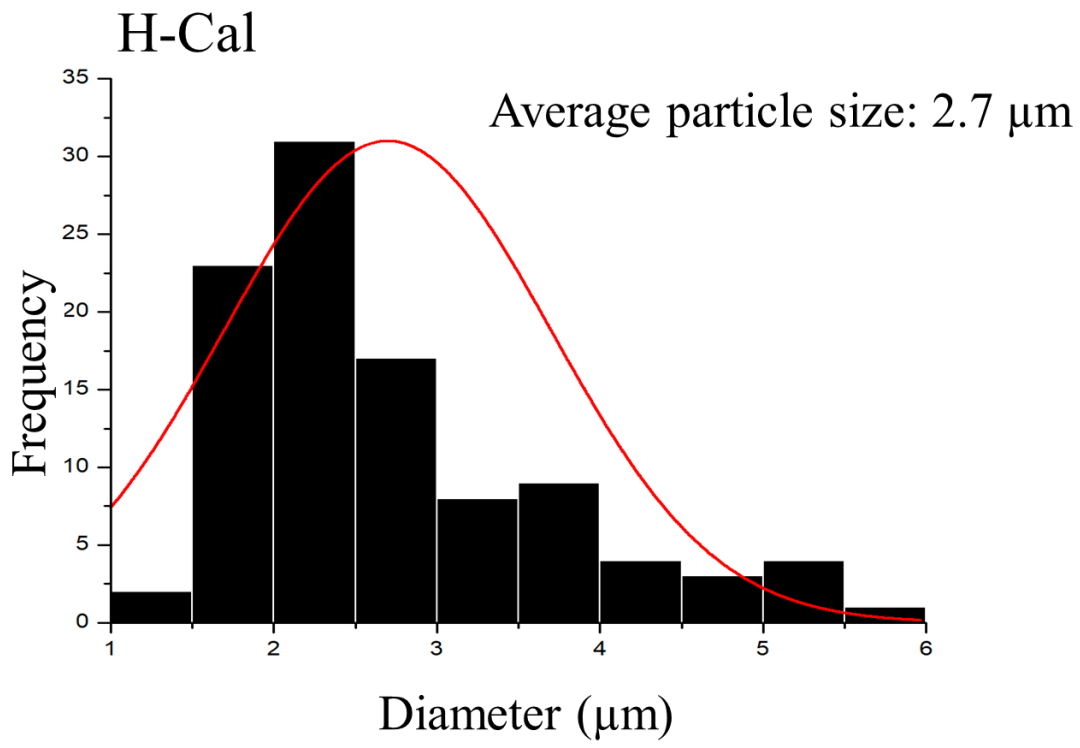

Figure 4.5: Particle size distribution of H-0.5Si A-I sample based upon the same SEM session as Figure 4.3.

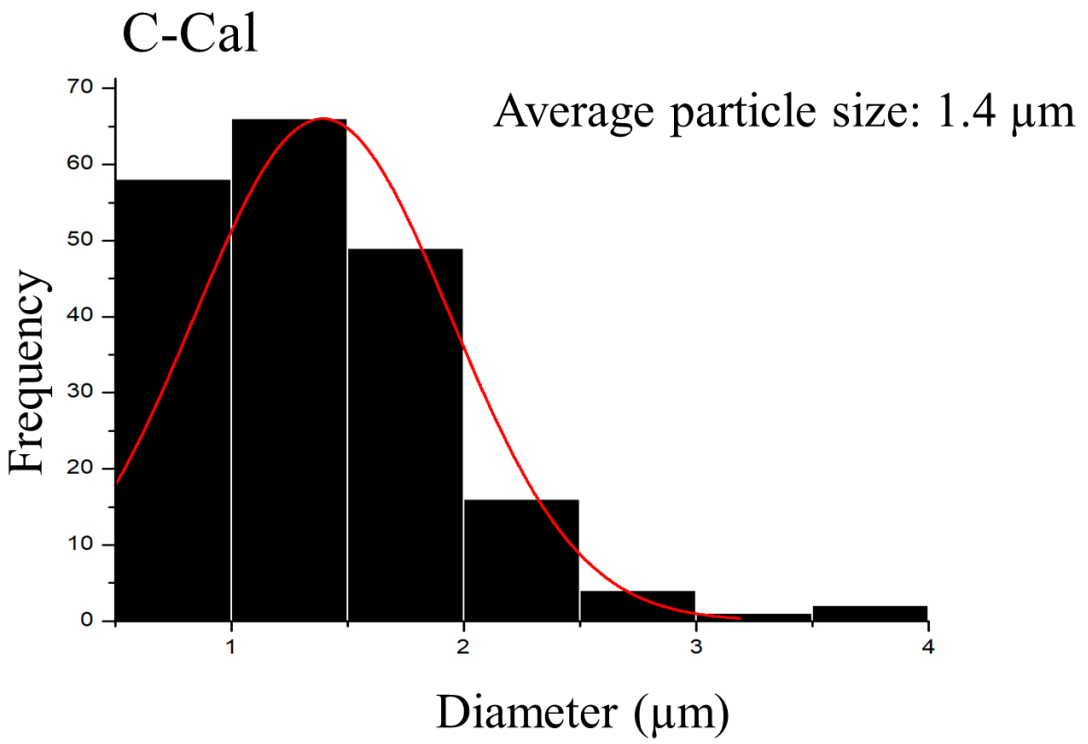

Figure 4.6: Particle size distribution of C-0.5Si A-I sample based upon the same SEM session as Figure 4.4.

Cui and Yang et al. report on hierarchical SAPO-34 having slightly lower specific surface area than the conventional version, supported by the values obtained for H-0.5Si A-I (524 m^2/g) and C-0.5Si A-I (528 m^2/g).[98, 99] Dai et al. reports the surface area of SAPO-34 is greatly dependent on the particle size, where smaller particle size would result in smaller internal surface area (microporous) and larger external surface area.[100] C-0.5Si A-I has a larger external/mesoporous surface area (41 m^2/g) than H-0.5Si A-I (30 m^2/g). This is most likely only external surface area as the conventional sample has a smaller average particle size, and no meso-SDA was added to it, supporting Dai et al.[100] The small particle size of C-0.5Si A-I could be due to aluminium isopropoxide as aluminium source. Aluminium isopropoxide provides a homogenous aluminium precursor distribution, which could have led to more nucleation sites forming simultaneously, resulting in smaller crystallites and larger external surface area according to Emrani and Dai et al.[44, 100] It was not possible to say whether the external surface area of the conventional sample was mesoporous due to agglomeration of the particles creating intercrystalline mesovoids between them according to Pérez-Ramírez et al. (Figure 2.6.b).[15] From the SEM images however, agglomeration was apparent for C-0.5Si A-I (Figure 4.4).

The desired hierarchical SAPO-34 structure was defined as the conventional structure built up around ordered mesoporous channels (Figure 2.6.c), and not mesosized intercrystalline voids between small crystallites (Figure 2.6.b).[15] The H-0.5Si A-I sample had a larger average particle size than the conventional sample, suggesting a smaller external/mesoporous surface area which it had (30 m^2/g), supporting Dai et al.[100] Zhang and Chu et al. state that F127 can function as both meso-SDA and growth inhibitor of crystallites during crystallisation.[47, 48] This would suggest the average particle size of the H-0.5Si A-I sample being smaller than for the C-0.5Si A-I sample as all other synthesis conditions were equal. Since the H-0.5Si A-I sample has a larger average particle size than C-0.5Si A-I, F127 has not been growth inhibiting. If F127 has functioned as a meso-SDA is unclear, as it could have been phase separated from the forming particles during synthesis, where the resulting external surface area is just that and not mesoporous.

Based upon the results from BET and SEM, it could not be said for certain if the meso-SDA containing sample H-0.5Si A-I was hierarchical, and the goal of synthesizing hierarchical SAPO-34 was reached. Hysteresis in the adsorption isotherm indicated hierarchical porosity for the H-0.5Si A-I sample, but for the C-0.5Si A-I sample it was most likely external surface of the crystallites due to smaller particle size.[100]

4.3 State of the samples after ion exchange

In the following sections, the goal of whether the samples retain their crystallinity and porosity after ion exchange with Ag^+ and Cu^{2+} is addressed, and how much metal they take up.

4.3.1 Crystallinity after ion exchange

Both samples were ion exchanged 4 times with Ag^+ and/or Cu^{2+}, after 1 round of ion exchange with ammonium nitrate. XRD and BET results were used to investigate their crystallinity and porosity after the first and fourth round of ion exchange with Ag^+ and/or Cu^{2+}. Observing whether these properties were still present after the ion exchange and if the two-step ion exchange method had worked, was important for studying their effect further in the HC-SCR of NO_x. The diffractograms for H-0.5Si A-I and C-0.5Si A-I after the first and fourth round of ion exchange with AgCu, Ag^+ and Cu^{2+} are presented below (Figure 4.7 and 4.8). The names will contain the metal species ion exchanged into the samples before the "Hier" and "Conv" part separated with a colon ":". 4R is added for the samples ion exchanged 4 times.

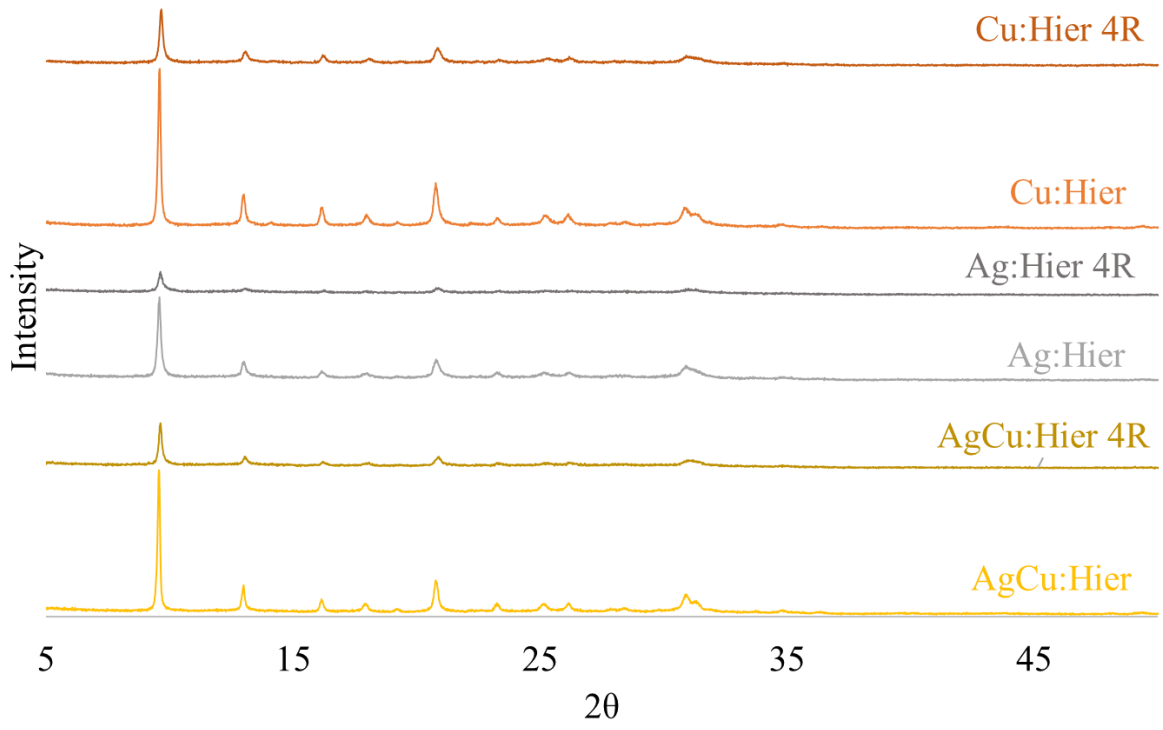

Figure 4.7: Stacked diffractograms for H-0.5Si A-I from 1 round of ion exchange with AgCu, Ag^+ and Cu^{2+}, to 4 rounds (4R). Loss in intensity of the peaks is common for all 3, where ion exchange with Ag^+ has the most reduction in intensity for the H-0.5Si A-I sample.

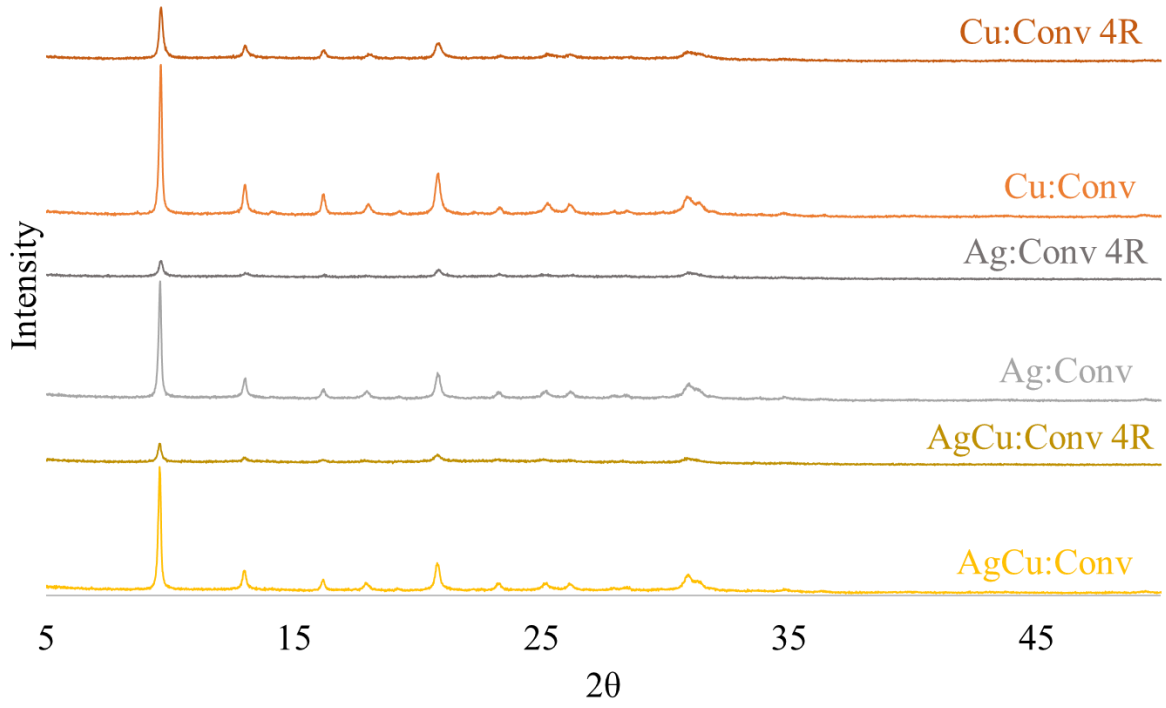

Figure 4.8: Stacked diffractograms for C-0.5Si A-I from 1 round of ion exchange with AgCu, Ag^{+} and Cu^{2+}, to 4 rounds (4R). Loss in intensity of the peaks is common for all 3, where ion exchange with Ag^{+} and AgCu has the most reduction in intensity for the C-0.5Si A-I sample.

With respect to the tallest peak of all the first round ion exchanged samples (Figure 4.7 and 4.8), AgCu:Hier has a loss of 68 %, Ag:Hier the highest loss of 70 % and Cu:Hier the lowest loss of 64 % in intensity after 3 additional rounds of ion exchange. Analogously for C-0.5Si A-I, AgCu:Conv has a loss of 82 %, Ag:Conv the highest loss of 83 % and Cu:Conv the lowest loss of 63 %. Ion exchange with only Cu^{2+} leads to the lowest loss in intensity (crystallinity) and is the least destructive on the SAPO-34 frameworks. Crystallinity is still present for H-0.5Si A-I and C-0.5Si A-I after 4 rounds of ion exchange however, meaning all samples still were protected from hydrolysis. Botne's samples completely collapsed after 1 round of direct ion exchange with AgCu, Ag^{+} and Cu^{2+}.[24] This shows the two-step ion exchange method was important for protection against hydrolysis during aqueous ion exchange with Ag^{+} and Cu^{2+}. This counts for H-0.5Si A-I, C-0.5Si A-I and all the other ion exchanged samples presented in Appendix A: Additional XRD results, supporting various literature.[2, 3, 5, 17-23]

4.3.2 Porosity after ion exchange

The change in specific surface area (SSA) for the H-0.5Si A-I and C-0.5Si A-I samples from the calcined stage (Hier-C and Conv-C) towards the first round and fourth round of ion exchange with AgCu, Ag^{+} and Cu^{2+}, are presented below (Figure 4.9 and 4.10)

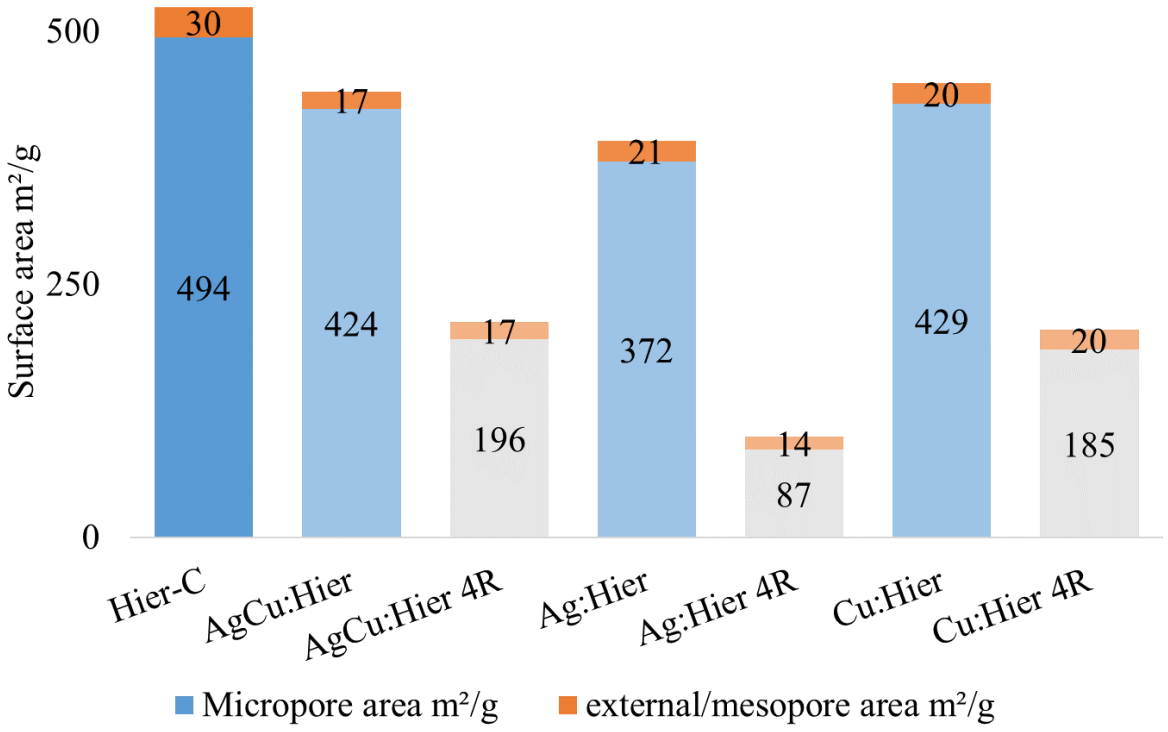

Figure 4.9: Change in specific surface area (SSA) distributed between micro- and mesoporous area, for H-0.5Si A-I from the calcinated stage towards 4 rounds of ion exchange with AgCu, Ag^{+} and Cu^{2+}.

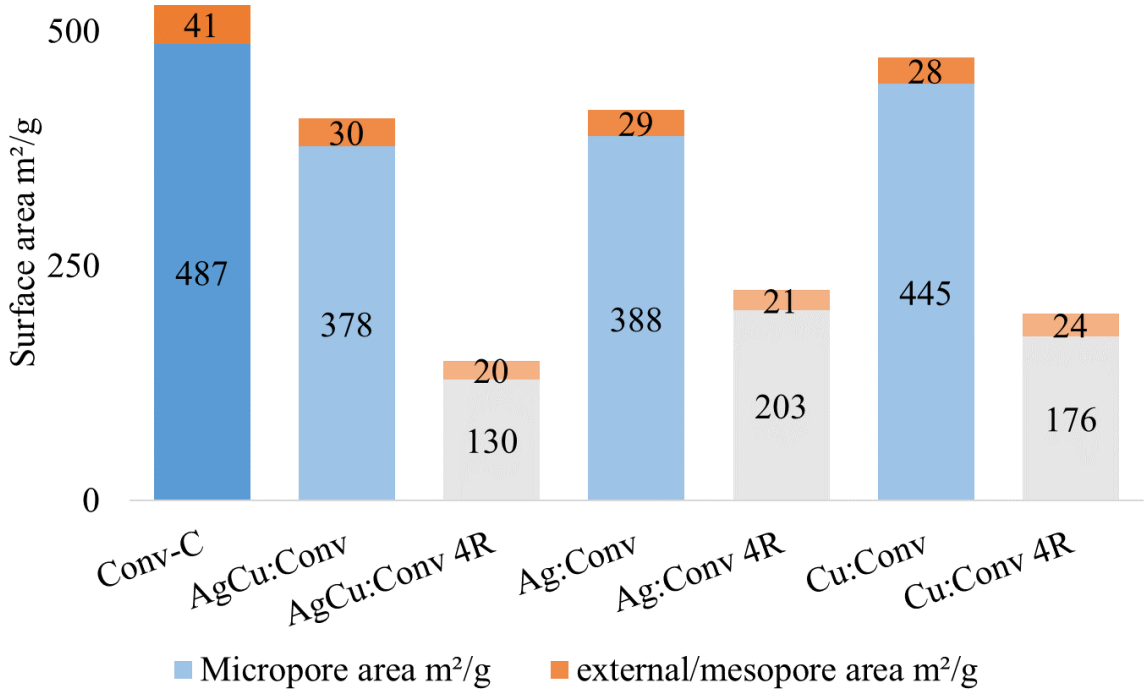

Figure 4.10: Change in specific surface area distributed between micro- and mesoporous/external surface area, for C-0.5Si A-I from the calcinated stage towards 4 rounds of ion exchange with AgCu, Ag^{+} and Cu^{2+}.

AgCu:Hier and Cu:Hier led to 14 % loss in microporous surface area after 1 round of ion exchange, and ca. 60 % in total after 4 rounds. Their external/mesoporous surface area suffered 43 % and 33 % respectively after 1 round of ion exchange, but no loss after 4 rounds. Ag:Conv and Cu:Conv lost 8 % and 20 % respectively in microporous surface area after 1 round of ion exchange and around 60% after 4 rounds. For external surface area loss, the values were ca. 30 % after the first round and 50 % after 4 rounds. The Ag:Hier and AgCu:Conv lost ca. 25 % in microporous surface area after 1 round of ion exchange, and 82 % and 73 % respectively after 4 rounds. Loss in external/mesoporous area was ca. 30 % and 25 % respectively after 1 round and 50 % after 4 rounds. The losses in micro- and mesoporous pore volume (PV) were very similar to those of the specific surface area (SSA) of the samples above and are presented in Appendix B: Additional BET results.

From the BET results the greatest loss in specific surface area after ion exchange appeared to be in the microporous range. The average mesopore width for the apparent mesopores of both samples increased. For H-0.5Si A-I the increase was (23.82 Å – 27.82 Å) from the calcined stage to after 4 rounds of ion exchange and (25.32 Å – 30.85 Å) for C-0.5Si A-I. Hydrolysis takes place at hydrophile sites in the framework, where the great apparent loss in microporosity

can indicate the location of the highest concentration of hydrophile sites.[2, 3, 5, 17-23] Despite loss of porosity in the samples after ion exchange, all samples maintained a specific surface area above 100 m^2/g.

The goal of preserving crystallinity and porosity in the samples after ion exchange with AgCu, Ag^+ and Cu^{2+} was reached, where the protective effect of the ammonium ion in the two-step ion exchange method was important. Appendix B presents the BET results of the other ion exchanged samples as well, where the same trends described above can be observed. Adsorption isotherms and pore size distribution (PSD) diagrams for H-0.5Si A-I and C-0.5Si A-I are presented here showing the same trends as presented earlier. PSD shows uniform loss in the pore size interval between the ion exchange stages. Hysteresis is maintained between the ion exchange stages, indicating preservation of external/mesoporous surface area between the ion exchange stages. Diagrams for the change in pore volume is also presented here with the same trend as for the specific surface area (Figure 4.9 and 4.10).

4.3.3 Metal content after ion exchange

Inductively coupled plasma – mass spectrometry (ICP-MS) was used for determining the weight percentage of silver and copper present inside the samples after ion exchange. Below, the ICP-MS results of the ion exchanged samples are presented (Figure 4.11 and 4.12), showing the metal contents of copper and silver present in weight percentage (wt%) after 1 round and 4 rounds of ion exchange.

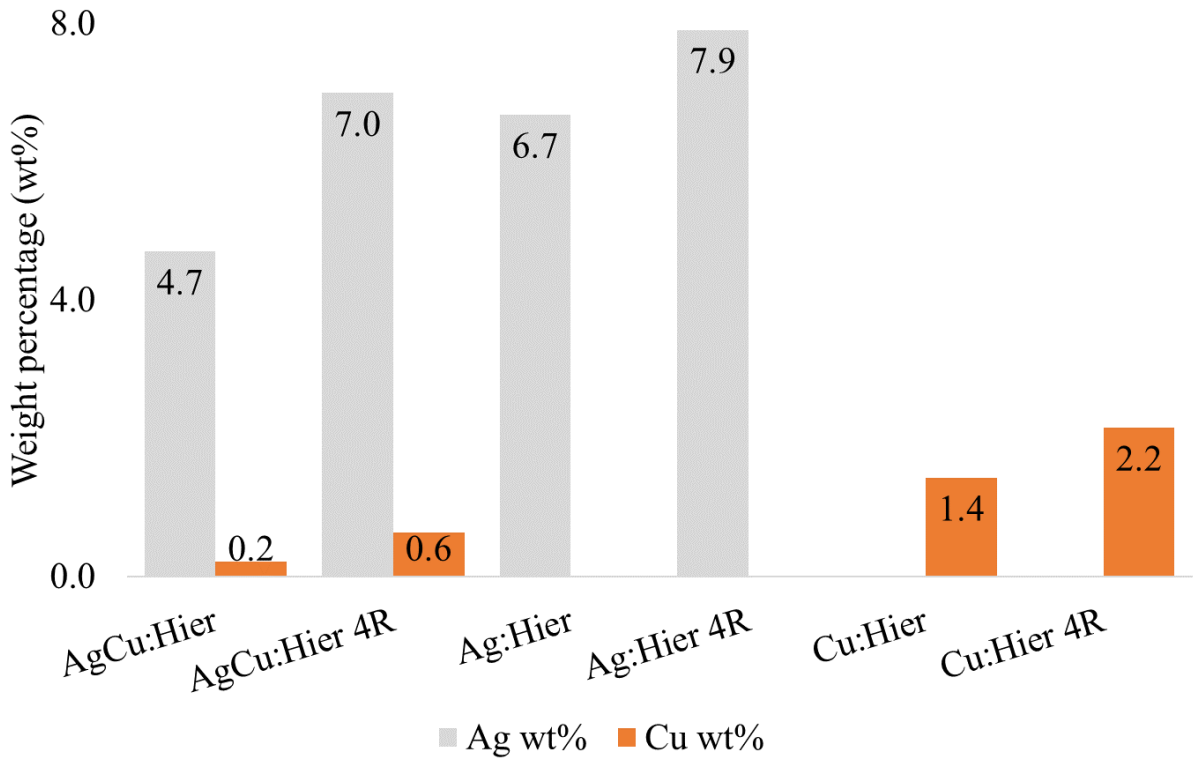

Figure 4.11: Metal content (wt%) present in the H-0.5Si A-I samples used for NO_x conversion analysis after 1 round and 4 rounds of ion exchange with $AgNO_3$ and $Cu(NO_3)_2$.

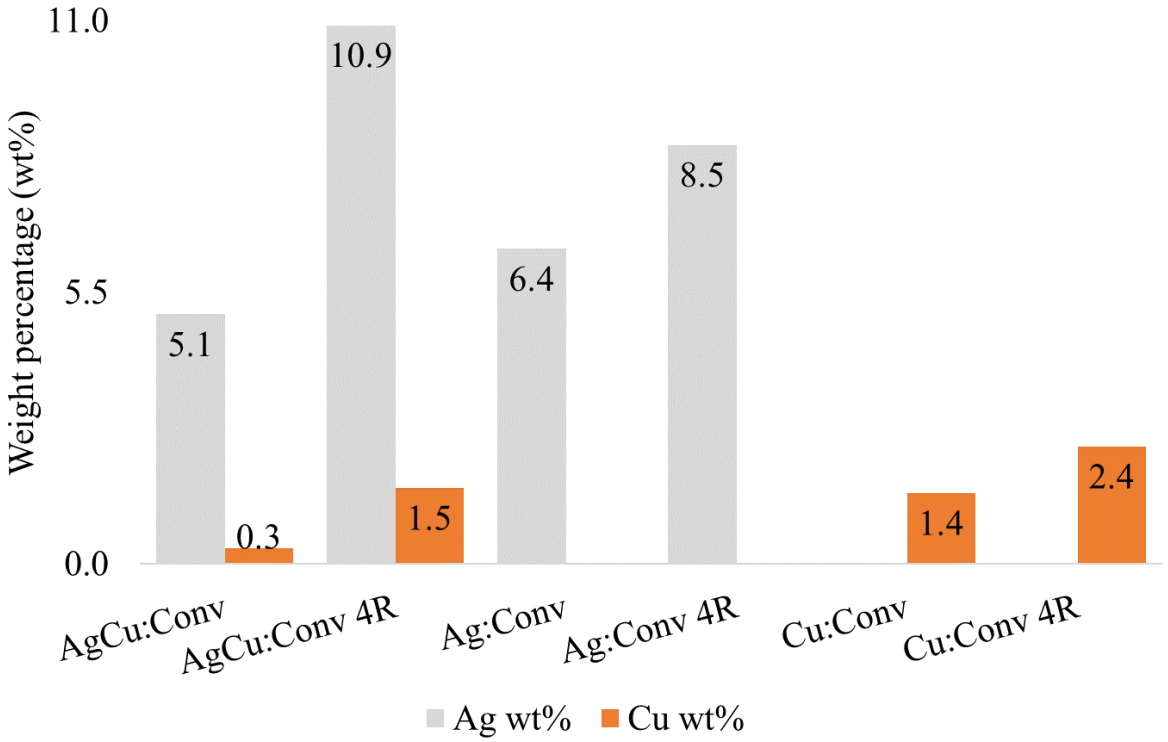

Figure 4.12: Metal content (wt%) present in the C-0.5 A-I samples used for NO_x conversion analysis after 1 round and 4 rounds of ion exchange with $AgNO_3$ and $Cu(NO_3)_2$.

As expected, the content of both silver and copper in all samples increased from 1 round of ion exchange to 4 rounds of ion exchange. The Ag:Hier (6.7 wt%) and Ag:Conv (6.4 wt%) samples already had a high silver content from the first round of ion exchange, with an increase of 18 % and 33 % respectively after 4 rounds. The Cu:Hier (1.4 wt%) and Cu:Conv (1.4 wt%) samples had a higher increase of 51 % and 66 % respectively after 4 rounds, but the greatest increase was for the simultaneously exchanged samples. For H-0.5Si A-I (Ag: 4.7 wt% and Cu: 0.2 wt%) the increase in silver and copper content was 49 % and 193 % respectively. For C-0.5Si A-I (Ag: 5.1 wt% and Cu: 0.3 wt%) the increase was 116 % and 385 % respectively. As stated by Paolucci et al., several rounds of ion exchange will increase the metal content, supported by these results.[62, 63]

The Cu^{2+} exchanged samples have similar copper content as Schetlein et al., but lower than Botne, while the Ag^{+} exchanged samples have higher silver content than Botne's.[24, 25] The AgCu samples have higher silver content and lower copper content than Schetlein and Botne.[24, 25]

Increasing copper content further would have required more rounds of ion exchange, which would have reduced the crystallinity and porosity further. Silver reached an unexpected high wt% after 1 round and 4 rounds of ion exchange and had an apparent higher affinity than Cu^{2+} for the samples' framework. Ag^{+} ion exchange was also apparently more destructive upon the frameworks, based upon the XRD results in Figure 4.7 and 4.8. In Appendix C: Additional ICP-MS results, the metal content of the other ion exchanged samples of this thesis are presented in Figure C.1 with similar values for the metal species.

4.3.4 Summary of section 4.1 – 4.3

Table 4-2 presents the total specific surface area (SSA) and the metal content of the H-0.5Si A-I and C-0.5Si A-I samples.

Table 4-2: Summary of total specific surface area (SSA) and metal content (wt%) results for all samples used in NO_x conversion analysis.

Sample	SSA m^2/g	Ag wt%	Cu wt%
Hier-C	524	-	-
AgCu:Hier	441	4.7	0.2
AgCu:Hier 4R	213	7.0	0.6
Ag:Hier	393	6.7	-
Ag:Hier 4R	101	7.9	-
Cu:Hier	449	-	1.4
Cu:Hier 4R	205	-	2.2
Conv-C	528	-	-
AgCu:Conv	408	5.1	0.3
AgCu:Conv 4R	150	10.9	1.5
Ag:Conv	417	6.4	-
Ag:Conv 4R	224	8.5	-
Cu:Conv	473	-	1.4
Cu:Conv 4R	200	-	2.4

4.4 NO_x conversion results

The crystallinity and porosity of the H-0.5Si A-I and C-0.5Si A-I samples were preserved after ion exchange, and these 2 samples were used further in the HC-SCR of NO_x. NO_x conversion results of the ion exchanged samples are presented below, along with activity diagrams (inspired from Botne's work)[24] presenting the conversion values reached at the different temperature intervals in percentage. The goal here was to use the HC-SCR of NO_x as a model reaction, to study the effect of porosity and presence of silver in the copper containing samples on the NO_x conversion. Propene was mainly used as the hydrocarbon source (HC) for the HC-SCR of NO_x described in section 3.7, but in section 4.4.5 the 4 samples using isobutane as hydrocarbon are presented. Botne considered samples with NO_x conversion greater than or equal to 30% as active samples, and the same is done in this thesis.[24] Botne used a dry feed while a wet feed was used in this thesis.[24, 25]

First a name change for all the samples used for NO_x conversion analysis is done. From here, the name of each sample will consist of the metal(s) that was/were exchanged into it before the colon ":". The "Hier" or "Conv" indicating the hierarchical or conventional sample as basis follows, and finally a digit representing the weight percentage of the metal(s) inside the sample. For AgCu samples, there will be a comma "," to mark the next digit. So, in AgCu:H-5.1,0.3 the weight percentage (wt%) of silver and copper inside the sample were 5.1 and 0.3 respectively. All the samples with new names are presented below (Table 4-3).

Table 4-3: Presents the names used for the samples used in NO_x conversion analysis.

Hier samples	New name	Conv samples	New name
AgCu:Hier	AgCu:Hier-4.7,0.2	**AgCu:Conv**	AgCu:Conv-5.1,0.3
AgCu:Hier 4R	AgCu:Hier-7.0,0.6	**AgCu:Conv 4R**	AgCu:Conv-10.9,1.5
Ag:Hier	Ag:Hier-6.7	**Ag:Conv**	Ag:Conv-6.4
Ag:Hier 4R	Ag:Hier-7.9	**Ag:Conv 4R**	Ag:Conv-8.5
Cu:Hier	Cu:Hier-1.4	**Cu:Conv**	Cu:Conv-1.4
Cu:Hier 4R	Cu:Hier-2.2	**Cu:Conv 4R**	Cu:Conv-2.4

4.4.1 NO_x conversion with silver and propene

Figure 4.13 presents the NO_x conversion diagram for the Ag^+ exchanged samples. None of the samples had any conversion values close to 30 % in any of the temperature intervals, so none were considered active.

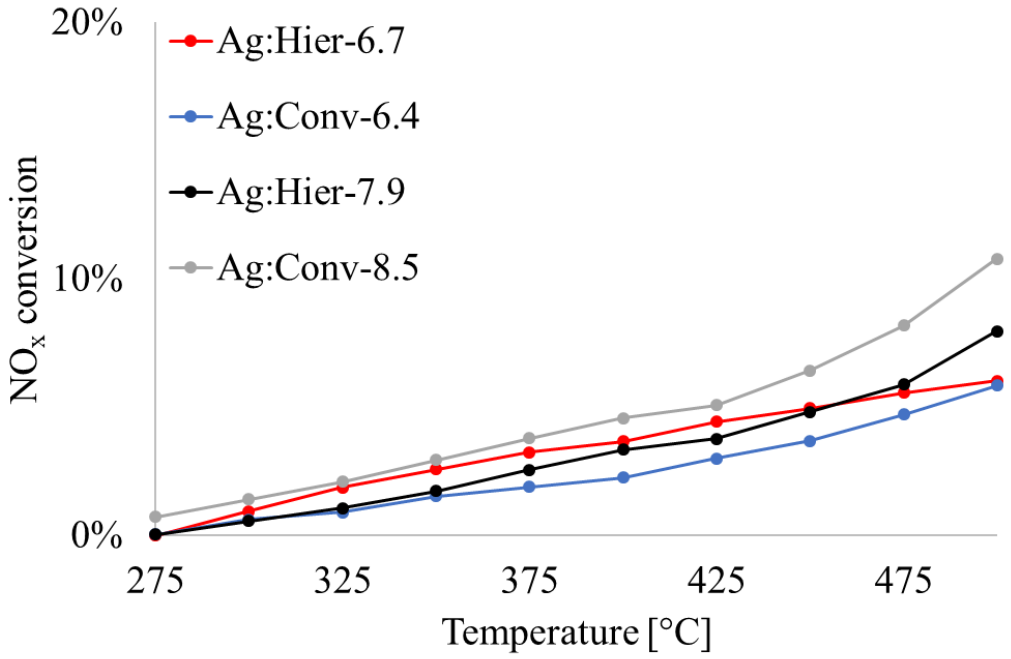

Figure 4.13: NO_x conversion for the samples: Ag:Hier-6.7, Ag:Conv-6.4, Ag:Hier-7.9 and Ag:Conv-8.5 with propene as hydrocarbon source.

Table 4-4 presents the conversion percentages for the samples (Figure 4.13). Although none were considered active, their maximum values are coloured yellow in Table 4-4 and were all at 500 °C. Botne's Ag^+ exchanged SAPO-34 samples showed no activity either, where Botne used a dry feed.[24] There was gradual increase in conversion at most temperature intervals for both the hierarchical and conventional sample after 4 rounds of ion exchange. Increase in silver content was likely the reason as crystallinity and porosity decreased for these 2 samples, indicating Ag^+ could be considered active at higher silver content.

Table 4-4: Activity diagram for the samples: Ag:Hier-6.7, Ag:Conv-6.4, Ag:Hier-7.9 and Ag:Conv-8.5 with propene as hydrocarbon source.

Temperature (°C)	275	300	325	350	375	400	425	450	475	500
Ag:Hier-6.7	0	1	2	3	3	4	4	5	6	6
Ag:Conv-6.4	0	1	1	2	2	2	3	4	5	6
Ag:Hier-7.9	0	1	1	2	3	3	4	5	6	8
Ag:Conv-8.5	1	1	2	3	4	5	5	6	8	11

4.4.2 NO_x conversion with copper and propene

Figure 4.14 presents the NO_x conversion diagram for the copper exchanged hierarchical and conventional samples.

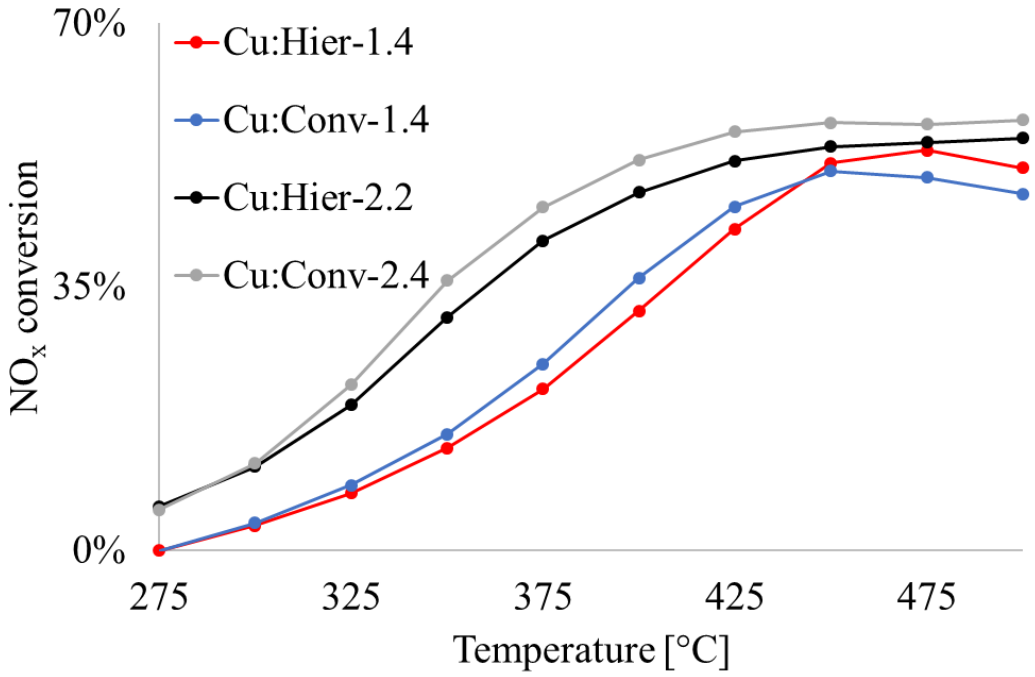

Figure 4.14: NO_x conversion for the samples: Cu:Hier-1.4, Cu:Conv-1.4, Cu:Hier-2.2 and Cu:Conv-2.4 with propene as hydrocarbon source.

Table 4-5 presents the conversion percentages for the samples (Figure 4.14). The red cells in the table mark the values for which the samples are active, and the green mark the maximum conversion obtained for each sample. Cu:Hier-1.4 and Cu:Conv-1.4 were active from 400 °C and up, and Cu:Hier-2.2 and Cu:Conv-2.4 were active from 350 °C and up, likely due to the increase in copper content as crystallinity and porosity had decreased for the latter 2. This was similar to Botne's Cu^{2+} exchanged samples, but lower than Schjetlein, both using a dry feed.[24, 25]

Table 4-5: Activity diagram for the samples: Cu:Hier-1.4, Cu:Conv-1.4, Cu:Hier-2.2 and Cu:Conv-2.4 with propene as hydrocarbon source.

Temperature (°C)	275	300	325	350	375	400	425	450	475	500
Cu:Hier-1.4	0	3	8	14	21	32	43	51	53	51
Cu:Conv-1.4	0	4	9	15	25	36	46	50	50	47
Cu:Hier-2.2	6	11	19	31	41	48	52	54	54	55
Cu:Conv-2.4	5	12	22	36	46	52	56	57	57	57

4.4.3 NO_x conversion with AgCu and propene

Figure 4.15 presents the NO_x conversion diagram for the AgCu exchanged hierarchical and conventional samples.

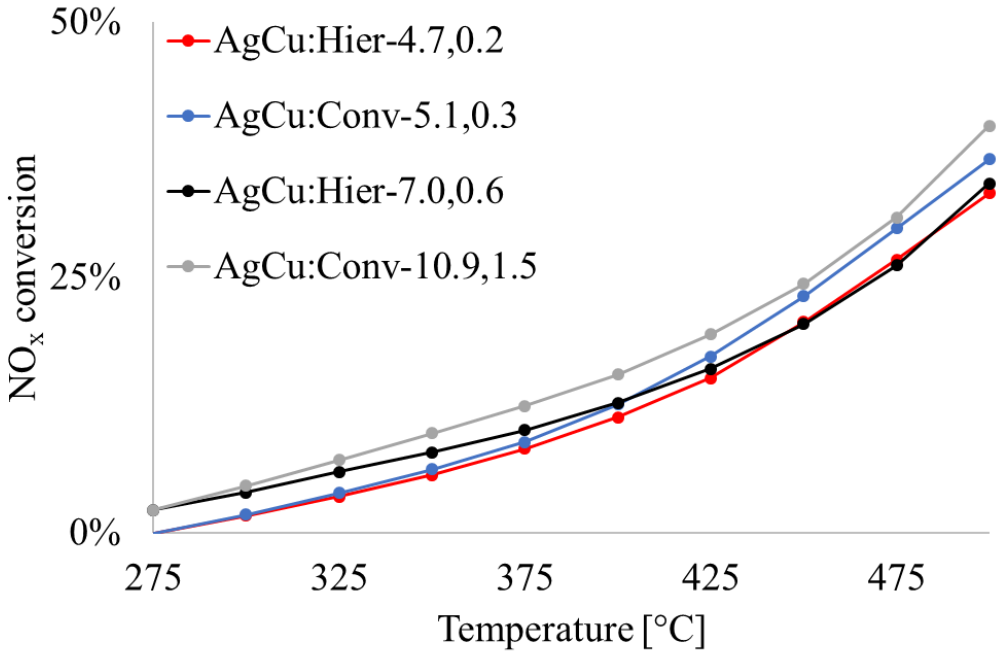

Figure 4.15: NO_x conversion for the samples: AgCu:Hier-4.7,0.2, AgCu:Conv-5.1,0.3, AgCu:Hier-7.0,0.6 and AgCu:Conv-10.9,1.5 with propene as hydrocarbon source.

Table 4-6 presents the conversion percentages for the samples (Figure 4.15). Again, the red cells in the table mark the values for which the samples are active, and the green mark the maximum conversion obtained for each sample. AgCu:Hier-4.7,0.2 and AgCu:Hier-7.0,0.6 had their maximum conversion at 500 °C, and no activity at the lower temperature intervals. For AgCu:Conv-5.1,0.3 and AgCu:Conv-10.9,1.5 it was the same, where they were active at 475 °C as well. The hierarchical sample had higher and lower conversion than Botne and Schjetlein respectively, and opposite for the conventional sample.[24, 25] It was unclear to say whether this was due to the lower copper content present in the samples, and if silver had an effect.

Table 4-6: Activity diagram for the samples: AgCu:Hier-4.7,0.2, AgCu:Conv-5.1,0.3, AgCu:Hier-7.0,0.6 and AgCu:Conv-10.9,1.5 with propene as hydrocarbon source.

Temperature (°C)	**275**	**300**	**325**	**350**	**375**	**400**	**425**	**450**	**475**	**500**
AgCu:Hier-4.7,0.2	0	2	4	6	8	11	15	21	27	33
AgCu:Conv-5.1,0.3	0	2	4	6	9	13	17	23	30	37
AgCu:Hier-7.0,0.6	2	4	6	8	10	13	16	20	26	34
AgCu:Conv-10.9,1.5	2	5	7	10	12	16	19	24	31	40

4.4.4 NO_x conversion with mechanically mixed silver and copper samples with propene

NO_x conversion for the mechanically mixed Ag^+ and Cu^{2+} exchanged hierarchical and conventional samples are given below (Figure 4.16). Here, the Ag:Hier and Cu:Hier samples were mixed, receiving the following name: [Ag+Cu]:Hier-7.9,2.2. Likewise the Ag:Conv and Cu:Conv samples were mixed, receiving the following name: [Ag+Cu]:Conv-8.5,2.4.

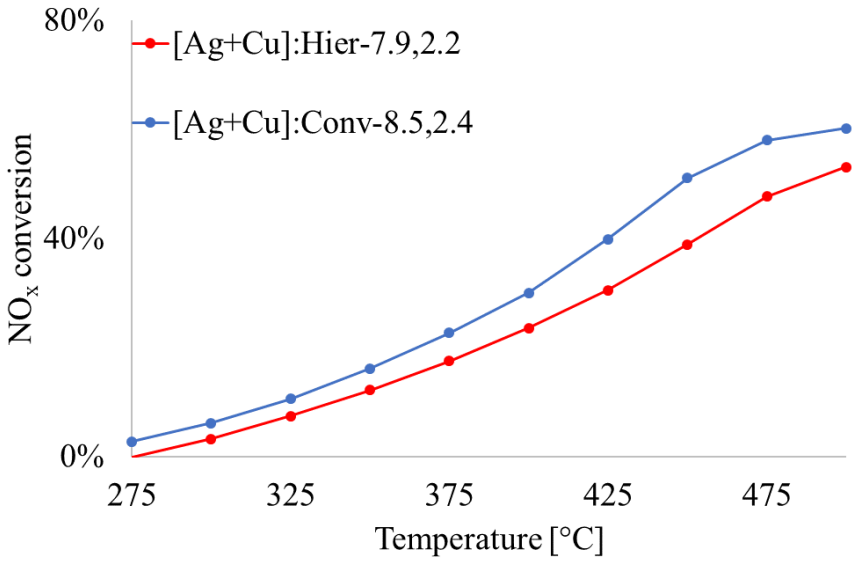

Figure 4.16: NO_x conversion for the samples: [Ag+Cu]:Hier-7.9,2.2 and [Ag+Cu]:Conv-8.5,2.4 with propene as hydrocarbon source.

Table 4-7 presents the conversion percentages for the samples (Figure 4.16). [Ag+Cu]:Hier-7.9,2.2 and [Ag+Cu]:Conv-8.5,2.4 both had their maximum conversion at 500 °C, where [Ag+Cu]:Conv-8.5,2.4 had the highest obtained conversion of all samples at any temperature in this thesis. [Ag+Cu]:Conv-8.5,2.4 was active from 400 °C and upwards, and [Ag+Cu]:Hier-7.9,2.2 was active from 425 °C and upwards. These values were higher than Botne's mechanically mixed samples, for which the conventional had no activity and the hierarchical was just below 30 %.[24] Around the same maximum conversion was reached as for the copper exchanged samples, with half the amount of copper exchanged sample, suggesting silver had an effect.

Table 4-7: Activity diagram for the samples: [Ag+Cu]:Hier-7.9,2.2 and [Ag+Cu]:Conv-8.5,2.4 with propene as hydrocarbon source.

Temperature (°C)	**275**	**300**	**325**	**350**	**375**	**400**	**425**	**450**	**475**	**500**
[Ag+Cu]:Hier-7.9,2.2	0	3	7	12	18	24	31	39	48	53
[Ag+Cu]:Conv-8.5,2.4	3	6	11	16	23	30	40	51	58	60

4.4.5 NO_x-conversion for samples with isobutane as HC for SCR

The NO_x conversion diagram with the samples using isobutane is shown below (Figure 4.17).

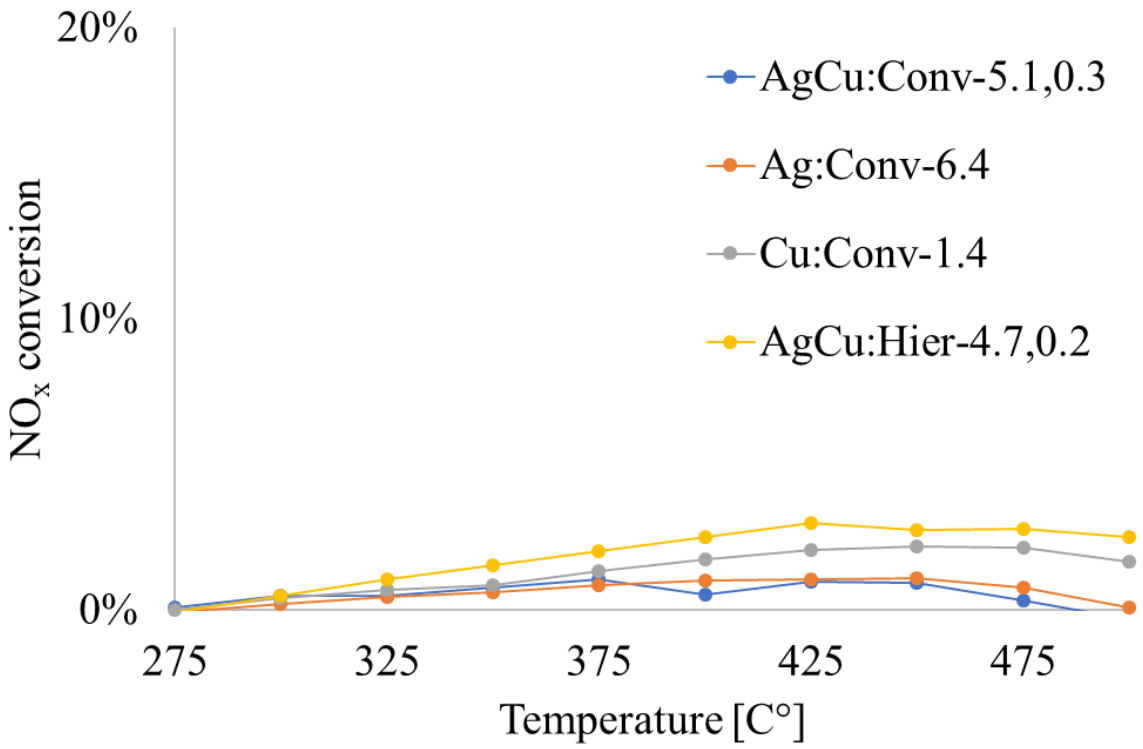

Figure 4.17: NO_x conversion for the samples: AgCu:Conv-5.1,0.3, Ag:Conv-6.4, Cu:Conv-1.4 and AgCu:Hier-4.7,0.2 with isobutane as hydrocarbon source.

Table 4-8 presents the conversion percentages for all the samples (Figure 4.17). None of the samples had any NO_x conversion close to 30 % at any of the temperature intervals. The maximum conversion values are coloured yellow in Table 4-8 just like Table 4-4. These results suggested very low concentration of active sites inside the apparent mesopores and external surface of the samples. The same samples except Ag:Conv-6.4 were considered active with propene as hydrocarbon and suggested isobutane was unable to reach the active sites inside the CHA cage as expected.

Table 4-8: Activity diagram for the samples: AgCu:Conv-5.1,0.3, Ag:Conv-6.4, Cu:Conv-1.4 and AgCu:Hier-4.7,0.2 with isobutane as hydrocarbon source.

Temperature (°C)	**275**	**300**	**325**	**350**	**375**	**400**	**425**	**450**	**475**	**500**
AgCu:Conv-5.1,0.3	0	0	0	1	1	1	1	1	0	0
Ag:Conv-6.4	0	0	0	1	1	1	1	1	1	0
Cu:Conv-1.4	0	0	1	1	1	2	2	2	2	2
AgCu:Hier-4.7,0.2	0	1	1	2	2	3	3	3	3	3

4.4.6 Summary of section 4.4

Table 4-9 summarizes the highest conversion values at their specific temperature intervals, from the activity diagrams in section 4.4. From the results, the samples only containing silver showed no activity. The samples using isobutane as hydrocarbon source showed no activity either, set in the lowest 4 rows of Table 4-9. The copper and AgCu samples, and mechanically mixed samples showed activity. The Cu^{2+} exchanged and mechanically mixed samples had conversions over 50 % and a broad temperature range of activity. The simultaneously exchanged samples had a narrow temperature range where they were active, either only 500 °C or 475-500 °C, and had activities very close to the lower limit of 30 %.

Table 4-9: Summary of the samples' maximum conversion values of NO_x at their specific temperature intervals.

Temperature (°C)	Temperature of max conversion (°C)	Conversion (%)
Cu:Hier-1.4	**475**	**53**
Cu:Conv-1.4	**450**	**50**
Cu:Hier-2.2	**500**	**55**
Cu:Conv-2.4	**500**	**57**
[Ag+Cu]:Hier-7.9,2.2	**500**	**53**
[Ag+Cu]:Conv-8.5,2.4	**500**	**60**
AgCu:Hier-4.7,0.2	**500**	**33**
AgCu:Conv-5.1,0.3	**500**	**37**
AgCu:Hier-7.0,0.6	**500**	**34**
AgCu:Conv-10.9,1.5	**500**	**40**
Ag:Hier-6.7	**500**	**6**
Ag:Conv-6.4	**500**	**6**
Ag:Hier-7.9	**500**	**8**
Ag:Conv-8.5	**500**	**11**
AgCu:Conv-5.1,0.3	**375**	**1**
Ag:Conv-6.4	**450**	**1**
Cu:Conv-1.4	**450**	**2**
AgCu:Hier-4.7,0.2	**425**	**3**

In the next section the results will be put together to address the thesis in more general terms in order to establish in what degree the different parts of it can be answered, and what needs further investigation.

5.0 Discussion

For this master's thesis, the effect of porosity and presence of silver in Cu:SAPO-34 were investigated in the HC-SCR of NO_x, using propene and isobutane as hydrocarbons in a wet feed. For this purpose, the following discussion has been divided in 2 main parts to answer what the effect of porosity and the presence of silver inside Cu:SAPO-34 has had for the NO_x conversion. Whether conventional or hierarchical SAPO-34 was obtained will be further discussed, however from the XRD results in section 4.1, at least phase pure SAPO-34 was obtained.

5.1 Effect of porosity

From the BET (Table 5-1) and SEM results it was unclear to state whether C-0.5Si A-I was conventional and H-0.5Si A-I hierarchical, where a type I and type IV adsorption isotherm was expected for them respectively. Both samples had a type IV adsorption isotherm with hysteresis, and part of their total specific surface area (SSA) was in the mesosized range. Particle size was smaller for C-0.5Si A-I than for H-0.5Si A-I, where the larger mesosized area of the C-0.5Si A-I most likely belonged only to the external surface of its crystallites. This is supported by Dai et al. stating smaller crystallites provide larger total external area, and no meso-SDA was added to C-0.5Si A-I.[100] Aluminium isopropoxide as an organic aluminium precursor promotes smaller crystallite size according to Emrani et al. and supports the obtained crystallite sizes for the C-0.5Si A-I sample.[44] These arguments strongly suggested the sample was conventional.

Table 5-1: Summary of total specific surface area (SSA) distributed in micro- and meso/external surface area, and metal content (wt%) for selected samples used in NO_x conversion analysis with propene as hydrocarbon. Maximum NO_x conversion reached for the samples is included in the last column.

Sample	SSA m^2/g	Micro m^2/g	Meso m^2/g	Ag wt%	Cu wt%	Max. NO_x conversion %
H-0.5Si A-I	524	494	30	-	-	-
AgCu:Hier-7.0,0.6	213	196	17	7.0	0.6	34
Ag:Hier-7.9	101	87	14	7.9	-	8
Cu:Hier-2.2	205	185	20	-	2.2	55
[Ag+Cu]	-	-	-	-	-	53
C-0.5Si A-I	528	487	41	-	-	-
AgCu:Conv-10.9,1.5	150	130	20	10.9	1.5	40
Ag:Conv-8.5	224	203	21	8.5	-	11
Cu:Conv-2.4	200	176	24	-	2.4	57
[Ag+Cu]	-	-	-	-	-	60

Whether H-0.5Si A-I had the desired hierarchical framework (mesosized pores and channels connected to the external surface of the crystallites) could not be claimed based only on the obtained BET and SEM results. The mesosized surface area for H-0.5Si A-I could have been mesopores, external surface of the crystallites or both. H-0.5Si A-I was the most promising candidate of all synthesized meso-SDA containing samples however, as it had the most mesosized surface area.

The employed two-step ion exchange method for the samples was expected to give some loss in crystallinity and porosity, but less than for direct ion exchange, from which Botne's samples completely collapsed.[24] All samples maintained crystallinity after 4 rounds of ion exchange, and total specific surface area above 100 m^2/g, which was a good indication of the protective effect of the ammonium ion.[2, 3, 5, 17-23] Metal content increasing from the first to the fourth round of ion exchange, indicated remaining Brønsted acid sites and ammonium sites also gradually being exchanged with Ag^+ and Cu^{2+} species.

The biggest loss in porosity after ion exchange was microporous for all samples, indicated by the loss of microporous surface area for the samples. This reflected where the highest concentration of the Brønsted acidity and other hydrophile sites prone to hydrolysis resided within all samples.[20, 22, 23] For the apparent mesopores/external surface in the samples an increase in average apparent mesopore size took place with increased rounds of ion exchange. This could indicate smaller sized apparent mesopores being more prone to hydrolysis and Pérez-Ramírez et al. states Brønsted acidity in mesopores is possible and shown by Miletto et al.[86, 101] This suggested the smallest apparent mesopores in the H-0.5Si A-I sample contained most of the Brønsted acidity in the meso range of the total specific surface area.[86, 101] For the conventional sample it likely meant general loss of external surface area, suggesting some Brønsted acidity present on the external surface of the sample's crystallites as well.

From the HC-SCR of NO_x results using isobutane, close to no conversion was reached at any of the temperature intervals. Isobutane is too big to enter the CHA cage, so whatever reaction the specie could undergo would be on possible active sites either in the mesopores or on the external surface of the crystallites. This further strengthened that most of the Brønsted acidity resided within the micropores as discussed above, and established in section 2.3.6.[86, 101]

From section 4.4, the ion exchanged versions of the C-0.5Si A-I sample with Ag^+, Cu^{2+}, AgCu and [Ag+Cu] had in general higher NO_x conversion values than the analogous versions of the

H-0.5Si A-I sample (Table 5-1). This was the case after 1 and 4 rounds of ion exchange, with very similar conversion profiles in the conversion diagrams. Only the 4 round exchanged samples are included in Table 5-1 due to their higher metal content. Copper content was lower than for Botne's (4 – 5.5 wt%) samples and silver content was higher than for Botne's (2 – 9 wt%) samples, but crystallinity and porosity was preserved for this thesis' samples (Table 5-1).[24] The mechanically mixed samples obtained surprisingly high NO_x conversion values (60 % for the conventional and 53 % for the hierarchical) compared to the analogous samples of Botne (3 % for the conventional and 25 % for the hierarchical).[24] Botne used a dry feed compared to the wet feed of this thesis, so the conditions were not identical for the obtained NO_x conversion values.

The higher conversions for the ion exchanged C-0.5Si A-I samples, could mean more accessible active sites for the reacting species than for their H-0.5Si A-I analogues. This agrees with more internal surface area being available for the C-0.5Si A-I samples due to smaller average particle size and less diffusion limitations, supporting Dai et al and others.[11-15, 100] Still, with similar metal content the H-0.5Si A-I samples are close to their C-0.5Si A-I analogues in conversion values (Table 5-1) despite larger average particle size. This could indicate presence of mesopores inside the H-0.5Si A-I ion exchanged samples, making more active sites available and reducing diffusion limitations as intended for hierarchical frameworks.

Botne argues for the low conversion of mechanically mixed samples due to long diffusion paths for the reacting species between the Cu^{2+} and Ag^{+} sites in the mechanically mixed samples. Because of small particle size of the C-0.5Si A-I and suspected hierarchy in the H-0.5Si A-I samples however, it could indicate shorter diffusion paths than for Botne's samples. Botne's samples had collapsed as well contrary to the samples mechanically mixed in this thesis, but without knowing Botne's samples' average particle size, it is unclear whether particle size and porosity made the difference. Further investigation is needed for stating whether porosity had an effect, but the effect of silver will be further discussed in section 5.2.

5.2 Effect of silver in Cu:SAPO-34

Silver content was more than 7 times higher than copper in the simultaneously exchanged samples (Table 5-1). Due to the samples' apparent higher affinity for Ag^+ species, Cu^{2+} may have been forced into the other positions of the CHA cage. Botne and Delic suggested ionic species behaving differently when ion exchanged simultaneously with other species, taking up different positions inside the framework than if they were ion exchanged alone.[24, 78] This could have led Cu^{2+} species in the position IV of the CHA cage (Figure 2.10). This position is more prone for direct hydrocarbon oxidation than providing the important NO_2 intermediate from NO and O_2 which is its intended oxidative function.[4, 5, 17, 61] The abundant Ag^+ sites would have less NO_2 to reduce towards N_2, thereby unable to perform its intended reducing function and lowering the samples' activity for NO_x conversion.

Ag^+ has low activity in reducing NO according to Halasz et al. where low conversion was expected and obtained by the purely silver exchanged samples.[75] This could explain the lower obtained NO_x conversion of the simultaneously ion exchanged samples with high silver and low copper content compared to the purely copper exchanged samples (Table 5-1). Had copper content (0.6 wt% for H-0.5Si A-I and 1.5 wt% for C-0.5Si A-I) been closer to the silver content (7.0 wt% for H-0.5Si A-I and 10.9 wt% for C-0.5Si A-I) in the simultaneously exchanged samples, it could have led to higher conversion as well. This is since the simultaneously ion exchanged samples already were active with the low copper content present and the purely copper exchanged samples showed an increasing activity temperature window and higher conversion with increased copper content. Higher copper content in the mechanically mixed samples than in the simultaneously exchanged samples could as such have been one of the reasons for its higher obtained NO_x conversion and wider activity temperature window. Here, it was more likely the Cu^{2+} and Ag^+ would exchange into the position III of the CHA cage as they were prepared separately first.[2-4, 17, 56-58]

Botne's simultaneously ion exchanged samples had an apparent synergistic effect, thought to be due to low diffusion length between the Cu^{2+} and Ag^+ sites inside the same CHA cage for the reacting species. This occurred for the conventional sample with a collapsed structure, which still reached a NO_x conversion of 83 % (in dry feed).[24] Botne had similar silver and copper content present, suggesting more Cu^{2+} present in the active sites (position III) inside the CHA cage.[2-4, 17, 24, 56-58] This thesis' samples still had their crystallinity and porosity intact, which could have led to a higher number of CHA cages with both Cu^{2+} and Ag^+ present inside,

providing the synergistic effect. For the mechanically mixed samples, the Cu^{2+} and Ag^{+} sites were in different CHA cages leading to bigger diffusion lengths, but still a synergistic effect was apparent here as well. This is because a higher NO_x conversion was reached for these samples with half the Cu^{2+} present than with the purely Cu^{2+} exchanged samples. This further supports the role of Cu^{2+} and Ag^{+} as oxidative and reductive sites in the HC-SCR of NO_x. Smaller particle size for the conventional sample and possible mesopores in the hierarchical could have assisted in shorter diffusion paths as well as suggested at the end of section 5.1.

Xiang et al. reported the Ag^{+} species having a protective effect towards hydrolysis like the ammonium ion on the framework. Based on the XRD and BET results however, most loss in crystallinity and porosity occurred during ion exchange with Ag^{+} and during the simultaneous ion exchange (AgCu), contradicting Xiang et al.[5] Cu^{2+} exchange was less destructive on the samples, but the final silver content for all samples was 3 times that of the copper content or higher. Botne who directly ion exchanged the samples, obtained more similar metal content values for copper and silver.[24] Botne used a 4:1 Ag^{+}:Cu^{2+} ratio for the simultaneously exchanged samples based on Delic's method for obtaining a 1:1 ratio between the metal species in zeolite Y, just like the samples in this thesis.[24, 78] Botne obtained 8.5 wt% (silver) and 5.5 wt% (copper) for the conventional sample, and 5.7 wt% (silver) and 4.3 wt% (copper) for the hierarchical sample.[24] Xiang et al. performed direct ion exchange as well to make simultaneously exchanged samples, but when increasing Ag^{+}:Cu^{2+} ratio, the difference in their content also increased.[5] Using a 1:1 ratio for Ag^{+}:Cu^{2+} resulted in silver (2.25 wt%) 50 % higher than for copper (1.42 wt%), and a 5:3 ratio gave 4.83 wt% for silver, over 3 times higher than for copper (1.46 wt%).[5]

These results could indicate that SAPO-34 in general has more affinity for the Ag^{+} ion when comparing with Xiang et al. and Botne. Xiang et al and Botne however performed direct ion exchange.[5, 24] Botne obtaining a Ag^{+}:Cu^{2+} closer to 1:1, could indicate Cu^{2+} is more easily exchanged with Brønsted acid sites (protons) than with ammonium ions, but Ag^{+} exchanges with similar ease for both.[24] When looking briefly at the kinetics, 2 ammonium ions need to exit the framework for each Cu^{2+} ion entering it, while only 1 has to exit for each Ag^{+} ion. For direct ion exchange however, protons need to exit the framework instead which are more mobile than the larger ammonium ion. This could have led to more similar copper and silver content after the ion exchange with protons (direct ion exchange) than for ammonium (two-step ion exchange). Several parallels of the same sample should have been exchanged with Cu^{2+} by either the direct or two-step method in order to see if different copper contents resulted in the

samples. A smaller Ag^{+}:Cu^{2+} ratio giving a 1:1 ratio between silver and copper content after simultaneous ion exchange should have been investigated for the two-step method as well. There was however not enough of the samples in order to investigate these topics and will be left for future work.

6.0 Conclusion

Strong indications were present for phase pure conventional SAPO-34 being successfully synthesized based upon the XRD and BET results obtained for the C-0.5Si A-I sample. The H-0.5Si A-I sample was phase pure as well, although its porosity could not be deemed hierarchical with the results from BET, SEM and the HC-SCR of NO_x only. Whether its specific surface area in the mesosized range was mesoporous or external surface needed further investigation. Smaller particle size of C-0.5Si A-I did assist in higher NO_x conversion, most likely reducing diffusion limitations. The H-0.5Si A-I sample was not far behind with larger particles, suggesting some hierarchy present inside the particles, providing the same effect.

Both samples preserved crystallinity and porosity after 4 rounds of ion exchange with Ag^+ and Cu^{2+}, showing good resistivity towards hydrolysis and proving the protective effect of the ammonium ion. The greatest loss of porosity was in the microporous region further indicating the location of most of the Brønsted acidity for both samples. Some apparent mesoporosity was lost, suggesting presence of hydrophile sites in the apparent mesopores and external surface of the crystallites as well. Based on the results from HC-SCR of NO_x with isobutane giving very low conversion however, Brønsted acidity was deemed very low in these regions.

Silver and copper content went up after several ion exchange rounds for all samples, as did their NO_x conversions, suggesting metal content being more crucial for the NO_x conversion than the degree of porosity. Porosity seemed to be one of the determining factors for obtaining high conversion with the mechanically mixed samples however, where Botne obtained much lower with collapsed samples. Ag^+ and Cu^{2+} were most likely in the necessary position III of the CHA cage for high activity, resulting in the high NO_x conversion. Lower, but still considerable conversion for the simultaneously exchanged samples was suggested to be because of the lower Cu^{2+} content than in the purely copper exchanged samples. The Cu^{2+} in the simultaneously exchanged samples was suggested to be stationed in a larger degree at the other possible positions of the CHA cage. The same synergistic effect which Botne experienced was suggested to occur with the mechanically mixed and simultaneously exchanged samples here as well.

7.0 Further work

The mechanically mixed conventional and hierarchical samples of silver and copper should be investigated further with regards to the synergistic effect taking place, and what role porosity and degree of crystallinity has in the HC-SCR of NO_x. Performing HC-SCR of NO_x with propene on the samples in both a dry and wet feed should be investigated further in order to observe the effect of water on the NO_x conversion of the samples. This information could be used to further study the role water has in the reaction mechanism of NO_x reduction. From here it is also natural to look further into the product selectivity of the samples and whether the samples have selectivity for the desired product N_2, or if selectivity is higher for other products.

Further investigating the coordination Ag^+ and Cu^{2+} species have inside the CHA cage when ion exchanged simultaneously should also be investigated further, and what effect this has on NO_x conversion. Looking into which coordinations occur with different ion exchange conditions (Ag^+:Cu^{2+} ratio used, salts used and concentrations used) inside the CHA cage with simultaneous ion exchange could be investigated. What Ag^+:Cu^{2+} ratio during simultaneous ion exchange gives a 1:1 ratio afterwards between silver and copper could be investigated as well.

The methanol to olefin reaction could be used as a different model reaction for the plain conventional and hierarchical samples, to get a better understanding about their Brønsted acidity distribution between the micropores and apparent mesopores/external surface.

8.0 Literature

1. Iwamoto, M., *Metal ion-exchanged zeolites as highly active materials for removal of nitrogen monoxide by catalytic decomposition, selective catalytic reduction, or adsorption*, in *Advanced Materials '93*, H. Aoki, et al., Editors. 1994, Elsevier. p. 117-122.
2. Fickel, D.W., et al., *The ammonia selective catalytic reduction activity of copper-exchanged small-pore zeolites.* Applied Catalysis B: Environmental, 2011. **102**(3): p. 441-448.
3. Fickel, D.W. and R.F. Lobo, *Copper coordination in Cu-SSZ-13 and Cu-SSZ-16 investigated by variable-temperature XRD.* Journal of Physical Chemistry C, 2010. **114**(3): p. 1633-1640.
4. Vogt, E.T.C., et al., *Chapter Two - Zeolites and Zeotypes for Oil and Gas Conversion*, in *Advances in Catalysis*, F.C. Jentoft, Editor. 2015, Academic Press. p. 143-314.
5. Xiang, X., et al., *Improving the low-temperature hydrothermal stability of Cu-SAPO-34 by the addition of Ag for ammonia selective catalytic reduction of NOx.* Applied Catalysis A: General, 2018. **551**: p. 79-87.
6. Leistner, K., et al., *Comparison of Cu/BEA, Cu/SSZ-13 and Cu/SAPO-34 for ammonia-SCR reactions.* Catalysis Today, 2015. **258**: p. 49-55.
7. Ma, L., et al., *Characterization of commercial Cu-SSZ-13 and Cu-SAPO-34 catalysts with hydrothermal treatment for NH3-SCR of NOx in diesel exhaust.* Chemical Engineering Journal, 2013. **225**: p. 323-330.
8. Gao, F., et al., *Current Understanding of Cu-Exchanged Chabazite Molecular Sieves for Use as Commercial Diesel Engine DeNOx Catalysts.* Topics in Catalysis, 2013. **56**(15): p. 1441-1459.
9. Christensen, C.H., et al., *Mesoporous zeolite single crystal catalysts: Diffusion and catalysis in hierarchical zeolites.* Catalysis Today, 2007. **128**(3): p. 117-122.
10. Yang, H., et al., *Synthesis and catalytic performances of hierarchical SAPO-34 monolith.* Journal of Materials Chemistry, 2010. **20**(16): p. 3227-3231.
11. Askari, S., R. Halladj, and A. Haghmoradi, *Effect of Synthesis Conditions on Selective Formation of SAPO-5 and SAPO-34 AU - Valizadeh, Bardiya.* Synthesis and Reactivity in Inorganic, Metal-Organic, and Nano-Metal Chemistry, 2014. **44**(1): p. 79-83.
12. Sun, Q., J. Yu, and Z. Xie, *The state-of-the-art synthetic strategies for SAPO-34 zeolite catalysts in methanol-to-olefin conversion.* National Science Review, 2017. **5**(4): p. 542-558.
13. Teketel, S., et al., *Morphology-induced shape selectivity in zeolite catalysis.* Journal of Catalysis, 2015. **327**: p. 22-32.
14. Guo, G., et al., *Cost-effective synthesis of hierarchical SAPO-34 zeolites with abundant intracrystalline mesopores and excellent MTO performance.* Chemical Communications, 2018. **54**(30): p. 3697-3700.
15. Pérez-Ramírez, J., et al., *Hierarchical zeolites: enhanced utilisation of microporous crystals in catalysis by advances in materials design.* Chemical Society Reviews, 2008. **37**(11): p. 2530-2542.
16. Xi, D., et al., *In situ growth-etching approach to the preparation of hierarchically macroporous zeolites with high MTO catalytic activity and selectivity.* Journal of Materials Chemistry A, 2014. **2**(42): p. 17994-18004.
17. Gao, F., et al., *Effects of Alkali and Alkaline Earth Cocations on the Activity and Hydrothermal Stability of Cu/SSZ-13 NH3–SCR Catalysts.* ACS Catalysis, 2015. **5**(11): p. 6780-6791.
18. Gao, F., et al., *Synthesis and Evaluation of Cu-SAPO-34 Catalysts for Ammonia Selective Catalytic Reduction. 1. Aqueous Solution Ion Exchange.* ACS Catalysis, 2013. **3**(9): p. 2083-2093.
19. Wang, J., et al., *Recent advances in the selective catalytic reduction of NOx with NH3 on Cu-Chabazite catalysts.* Applied Catalysis B: Environmental, 2017. **202**: p. 346-354.
20. Xu, M., et al., *New insight into Cu/SAPO-34 preparation procedure: Impact of NH4-SAPO-34 on the structure and Cu distribution in Cu-SAPO-34 NH3-SCR catalysts.* Applied Catalysis B: Environmental, 2018. **220**: p. 161-170.

21. Seijger, G.B.F., et al., *Screening of silver and cerium exchanged zeolite catalysts for the lean burn reduction of NOx with propene.* Applied Catalysis B: Environmental, 2003. **40**(1): p. 31-42.
22. Guo, Q., et al., *Effect of the Nature and Location of Copper Species on the Catalytic Nitric Oxide Selective Catalytic Reduction Performance of the Copper/SSZ-13 Zeolite.* ChemCatChem, 2014. **6**(2): p. 634-639.
23. Xie, L., et al., *Excellent Performance of One-Pot Synthesized Cu-SSZ-13 Catalyst for the Selective Catalytic Reduction of NOx with NH3.* Environmental Science & Technology, 2014. **48**(1): p. 566-572.
24. Botne, G., *The Effect of mechanical mixing and Porosity on the Activity of Ag and Cu Ion exchanged Zeotypes in the HC-SCR of NOx with Propene*, in *Department of Chemistry (IKJ)*. 2017, NTNU: Trondheim NTNU. p. 76.
25. Schjetlein, E.-M.M., *Understanding the Effect of Porosity of Cu:SAPO-34 and AgCu:SAPO-34 for the HC-SCR deNOx Reaction*, in *Department of Chemistry NTNU*. 2018, NTNU: Trondheim NTNU. p. 84.
26. Holma, T., et al., *Continuous lean NOx reduction with hydrocarbons over dual pore system catalysts.* Applied Catalysis B: Environmental, 2004. **48**(2): p. 95-100.
27. Shichi, A., A. Satsuma, and T. Hattori, *Influence of geometry-limited diffusion on the selective catalytic reduction of NO by hydrocarbons over Cu-exchanged zeolite.* Applied Catalysis B: Environmental, 2001. **30**(1): p. 25-33.
28. Martens, J.A., et al., *Molecule sieving catalysts for NO reduction with hydrocarbons in exhaust of lean burn gasoline and diesel engines.* Applied Catalysis B: Environmental, 2001. **29**(4): p. 299-306.
29. Oikawa, H., et al., *Highly selective conversion of ethene to propene over SAPO-34 as a solid acid catalyst.* Applied Catalysis A: General, 2006. **312**: p. 181-185.
30. Csicsery, S.M., *Catalysis by shape selective zeolites-science and technology*, in *Pure and Applied Chemistry*. 1986. p. 841.
31. Qiao, Z.A. and Q.S. Huo, *Chapter 15 - Synthetic Chemistry of the Inorganic Ordered Porous Materials*, in *Modern Inorganic Synthetic Chemistry (Second Edition)*, R. Xu and Y. Xu, Editors. 2017, Elsevier: Amsterdam. p. 389-428.
32. Baerlocher, C. 1996; Available from: http://www.iza-structure.org/databases/.
33. Ekpe, I., *Zeolite Synthesis, Characterisation and Application Areas: A Review*. Vol. 6. 2017.
34. Momma, K. and F. Izumi, *VESTA 3 for three-dimensional visualization of crystal, volumetric and morphology data.* Journal of Applied Crystallography, 2011. **44**(6): p. 1272-1276.
35. Teketel, S., et al., *Shape selectivity in zeolite catalysis. The Methanol to Hydrocarbons (MTH) reaction*. 2014. p. 179-217.
36. Material, A.; Available from: https://www.acsmaterial.com/sapo-1198.html.
37. Chorkendorff I., N.J.W., *Concepts of Modern Catalysis and Kinetics*, in *Concepts of Modern Catalysis and Kinetics*, W.-V.V.g.C. Kga, Editor. 2007. p. 131-134.
38. Izadbakhsh, A., et al., *Key parameters in hydrothermal synthesis and characterization of low silicon content SAPO-34 molecular sieve.* Microporous and Mesoporous Materials, 2009. **126**(1): p. 1-7.
39. Martínez-Espín, J.S., *Mechanistic and kinetic investigations on the role of methanol and dimethyl ether in the Methanol-To-Hydrocarbons reaction*. 2017.
40. Kong, L., et al., *The Synthesis of Hierarchical SAPO-34 and its Enhanced Catalytic Performance in Chloromethane Conversion to Light Olefins.* Catalysis Letters, 2014. **144**(9): p. 1609-1616.
41. Cao, G. and Y. Wang, *Nanostructures and nanomaterials : synthesis, properties, and applications*. 2013, New Jersey [etc.]: World Scientific.
42. Moliner, M., F. Rey, and A. Corma, *Towards the Rational Design of Efficient Organic Structure-Directing Agents for Zeolite Synthesis.* Angewandte Chemie International Edition, 2013. **52**(52): p. 13880-13889.
43. Najafi, N., S. Askari, and R. Halladj, *Hydrothermal synthesis of nanosized SAPO-34 molecular sieves by different combinations of multi templates.* Powder Technology, 2014. **254**: p. 324-330.

44. Emrani, P., S. Fatemi, and S.S. Ashraf Talesh, *Effect of Synthesis Parameters on Phase Purity, Crystallinity and Particle Size of SAPO-34*. Vol. 30. 2011.
45. Li, X., et al., *Synthesis and applications of hierarchically porous catalysts.* Chinese Journal of Catalysis, 2013. **34**(1): p. 22-47.
46. Sun, Q., et al., *Organosilane surfactant-directed synthesis of hierarchical porous SAPO-34 catalysts with excellent MTO performance.* Chemical Communications, 2014. **50**(49): p. 6502-6505.
47. Zhang, P., et al., *Direct synthesis of hierarchical SAPO-11 molecular sieve with enhanced hydroisomerization performance*. Fuel Processing Technology, 2018. **179**: p. 72-85.
48. Chu, S., et al., *Synthesis of Ga2O3/HZSM-5@cubic ordered mesoporous SiO2 with template Pluronic F127 to improve its catalytic performance in the aromatization of methanol.* Journal of Porous Materials, 2017. **24**(4): p. 1069-1078.
49. Wang, C., et al., *Dual template-directed synthesis of SAPO-34 nanosheet assemblies with improved stability in the methanol to olefins reaction.* Journal of Materials Chemistry A, 2015. **3**(10): p. 5608-5616.
50. Jakobsen, T.D., *SAPO-34 with Copper: Investigation of hierarchical pore characteristics and interactions with copper for catalytic applications*, in *Department of chemistry (IKJ)*. 2014. p. 73.
51. Dai, C., et al., *Chapter Two - Advances in the synthesis and catalysis of solid and hollow zeolite-encapsulated metal catalysts*, in *Advances in Catalysis*, C. Song, Editor. 2018, Academic Press. p. 75-115.
52. Iwamoto, M., et al., *Catalytic decomposition of nitric oxide over copper(II)-exchanged, Y-type zeolites.* Journal of the Chemical Society, Faraday Transactions 1: Physical Chemistry in Condensed Phases, 1981. **77**(7): p. 1629-1638.
53. Paolucci, C., et al., *Catalysis in a Cage: Condition-Dependent Speciation and Dynamics of Exchanged Cu Cations in SSZ-13 Zeolites.* Journal of the American Chemical Society, 2016. **138**(18): p. 6028-6048.
54. Bethke, K.A. and H.H. Kung, *Supported Ag Catalysts for the Lean Reduction of NO with C3H6.* Journal of Catalysis, 1997. **172**(1): p. 93-102.
55. Hartmann, M. and L. Kevan, *Transition-Metal Ions in Aluminophosphate and Silicoaluminophosphate Molecular Sieves: Location, Interaction with Adsorbates and Catalytic Properties.* Chemical Reviews, 1999. **99**(3): p. 635-664.
56. Deka, U., et al., *Changing active sites in Cu–CHA catalysts: deNOx selectivity as a function of the preparation method*. Microporous and Mesoporous Materials, 2013. **166**: p. 144-152.
57. Wang, L., et al., *Location and nature of Cu species in Cu/SAPO-34 for selective catalytic reduction of NO with NH3.* Journal of Catalysis, 2012. **289**: p. 21-29.
58. Xue, J., et al., *Characterization of copper species over Cu/SAPO-34 in selective catalytic reduction of NOx with ammonia: Relationships between active Cu sites and de-NOx performance at low temperature.* Journal of Catalysis, 2013. **297**: p. 56-64.
59. Ishihara, T., et al., *Copper Ion-Exchanged SAPO-34 as a Thermostable Catalyst for Selective Reduction of NO with C3H6.* Journal of Catalysis, 1997. **169**(1): p. 93-102.
60. Chen, H.-Y., *Cu/Zeolite SCR Catalysts for Automotive Diesel NOx Emission Control*, in *Urea-SCR Technology for deNOx After Treatment of Diesel Exhausts*, I. Nova and E. Tronconi, Editors. 2014, Springer New York: New York, NY. p. 123-147.
61. Miyadera, T., *Selective reduction of nitric oxide with ethanol over an alumina-supported silver catalyst.* Applied Catalysis B: Environmental, 1997. **13**(2): p. 157-165.
62. Vennestrøm, P.N.R., et al., *Migration of Cu Ions in SAPO-34 and Its Impact on Selective Catalytic Reduction of NOx with NH3.* ACS Catalysis, 2013. **3**(9): p. 2158-2161.
63. Paolucci, C., et al., *Chapter One - Catalysis Science of NOx Selective Catalytic Reduction With Ammonia Over Cu-SSZ-13 and Cu-SAPO-34*, in *Advances in Catalysis*, C. Song, Editor. 2016, Academic Press. p. 1-107.
64. Martínez-Franco, R., et al., *Rational direct synthesis methodology of very active and hydrothermally stable Cu-SAPO-34 molecular sieves for the SCR of NOx.* Applied Catalysis B: Environmental, 2012. **127**: p. 273-280.

65. Shibata, J., et al., *Influence of zeolite support on activity enhancement by addition of hydrogen for SCR of NO by propane over Ag-zeolites.* Applied Catalysis B: Environmental, 2004. **54**(3): p. 137-144.
66. Shimizu, K.-i. and A. Satsuma, *Selective catalytic reduction of NO over supported silver catalysts—practical and mechanistic aspects.* Physical Chemistry Chemical Physics, 2006. **8**(23): p. 2677-2695.
67. Boutros, M., J.-M. Trichard, and P. Da Costa, *Silver supported mesoporous SBA-15 as potential catalysts for SCR NOx by ethanol.* Applied Catalysis B: Environmental, 2009. **91**(3): p. 640-648.
68. Chen, H.-Y., et al., *Reduction over zeolite-based catalysts of nitrogen oxides in emissions containing excess oxygen: Unraveling the reaction mechanism.* Catalysis Today, 2004. **96**(1): p. 1-10.
69. Poignant, F., et al., *In situ FT-IR study of NH3 formation during the reduction of NOx with propane on H/Cu-ZSM-5 in excess oxygen.* Catalysis Today, 1996. **29**(1): p. 93-97.
70. Poignant, F., et al., *NH3 formation during the reduction of nitrogen monoxide by propane on H–Cu–ZSM-5 in excess oxygen.* Journal of the Chemical Society, Chemical Communications, 1995(1): p. 89-90.
71. Brosius, R. and J.A. Martens, *Reaction Mechanisms of Lean-Burn Hydrocarbon SCR over Zeolite Catalysts.* Topics in Catalysis, 2004. **28**(1): p. 119-130.
72. Azizi, Y., et al., *NOx abatement in the exhaust of lean-burn natural gas engines over Ag-supported γ-Al2O3 catalysts.* Surface Science, 2016. **646**: p. 186-193.
73. Liu, D.-J. and H.J. Robota, *On the Mechanism of NO Selective Catalytic Reduction by Hydrocarbons over Cu-ZSM-5 via X-ray Absorption Spectroscopic Study.* The Journal of Physical Chemistry B, 1999. **103**(14): p. 2755-2765.
74. Moreno-González, M., et al., *Evidence of a Cu2+–Alkane Interaction in Cu-Zeolite Catalysts Crucial for the Selective Catalytic Reduction of NOx with Hydrocarbons.* ACS Catalysis, 2017. **7**(5): p. 3501-3509.
75. Halasz, I. and A. Brenner, *Selectivity-determining role of C3H8/NO ratio in the reduction of nitric oxide by propane in presence of oxygen over ZSM5 zeolites.* Catalysis Letters, 1998. **51**(3): p. 195-206.
76. Traa, Y., B. Burger, and J. Weitkamp, *Zeolite-based materials for the selective catalytic reduction of NOx with hydrocarbons.* Microporous and Mesoporous Materials, 1999. **30**(1): p. 3-41.
77. Mathisen, K., et al., *Irreversible Silver(I) Interconversion in Ag:ZSM-5 and Ag:SAPO-5 by Propene and Hydrogen.* The Journal of Physical Chemistry C, 2012. **116**(1): p. 171-184.
78. Delic, A., *Characterization of copper cations in zeolite Y in presence of silver cations; the two-cation effect.*, in *Department of Chemistry (IKJ)*. 2009, NTNU: Trondheim NTNU. p. 135.
79. Pârvulescu, V.I., P. Grange, and B. Delmon, *NO decomposition over physical mixtures of Cu-ZSM-5 with zeolites or oxides.* Applied Catalysis B: Environmental, 2001. **33**(3): p. 223-237.
80. Sullivan, J.A. and O. Keane, *A combination of NOx trapping materials and urea-SCR catalysts for use in the removal of NOx from mobile diesel engines.* Applied Catalysis B: Environmental, 2007. **70**(1): p. 205-214.
81. Corbos, E.C., et al., *NOx abatement for lean-burn engines under lean–rich atmosphere over mixed NSR-SCR catalysts: Influences of the addition of a SCR catalyst and of the operational conditions.* Applied Catalysis A: General, 2009. **365**(2): p. 187-193.
82. Konova, P., et al., *A combination of Ag/alumina and Ag modified ZSM-5 to remove NOx and CO during lean conditions.* Applied Catalysis B: Environmental, 2007. **70**(1): p. 138-145.
83. Fischer, M. and R. Bell, *Cation-exchanged SAPO-34 for adsorption-based hydrocarbon separations: Predictions from dispersion-corrected DFT calculations*. 2014.
84. Luo, J.-Y., et al., *Hydrocarbon Poisoning of Cu-Zeolite SCR Catalysts*. 2012, SAE International.
85. Ye, Q., L. Wang, and R.T. Yang, *Activity, propene poisoning resistance and hydrothermal stability of copper exchanged chabazite-like zeolite catalysts for SCR of NO with ammonia in comparison to Cu/ZSM-5.* Applied Catalysis A: General, 2012. **427-428**: p. 24-34.

86. Miletto, I., et al., *Hierarchical SAPO-34 Architectures with Tailored Acid Sites using Sustainable Sugar Templates.* ChemistryOpen, 2018. **7**(4): p. 297-301.
87. Weller, M., et al., *Inorganic chemistry*. 2014. p. 234-235.
88. commercialization, L.M.d.a.; Available from: https://www.lucideon.com/testing-characterization/techniques/bet-surface-area-analysis-bjh-pore-size-volume-analysis.
89. Sultan, M., T. Miyazaki, and S. Koyama, *Optimization of adsorption isotherm types for desiccant air-conditioning applications.* Renewable Energy, 2018. **121**: p. 441-450.
90. Tang, X., et al., *The effect of the variation in material composition on the heterogeneous pore structure of high-maturity shale of the Silurian Longmaxi formation in the southeastern Sichuan Basin, China.* Journal of Natural Gas Science and Engineering, 2015. **23**: p. 464-473.
91. Sing, K.S.W., *Reporting Physisorption Data for Gas/Solid Systems With Special Reference to the Determination of Surface Area and Porosity*.
92. Skoog, D.A., et al., *Skoog and West's Fundamentals of analytical chemistry*. 2014, Cengage Learning: Andover, Hants. p. 802-809.
93. Skoog, D.A., et al., *Skoog and West's Fundamentals of analytical chemistry*. 2014, Cengage Learning: Andover, Hants. p. 778-779.
94. instruments, N. 2002; Available from: https://www.nanoscience.com/techniques/scanning-electron-microscopy/#how.
95. J., T., *Introduction of rhenium into porous supports*, in *Department of chemistry (IKJ) NTNU*. 2017, Norwegian university of science and technology (NTNU): Department of chemistry (IKJ) NTNU. p. 113.
96. Wells, K.H. 15.03.2019; Available from: https://www.ntnu.no/wiki/pages/viewpage.action?pageId=86728099.
97. Albertsen, E.H. 15.03.2019; Available from: https://www.ntnu.no/wiki/display/imtlab/BET.
98. Cui, Y., et al., *Pore-structure-mediated hierarchical SAPO-34: Facile synthesis, tunable nanostructure, and catalysis applications for the conversion of dimethyl ether into olefins.* Particuology, 2013. **11**(4): p. 468-474.
99. Yang, S.-T., et al., *Microwave synthesis of mesoporous SAPO-34 with a hierarchical pore structure.* Materials Research Bulletin, 2012. **47**(11): p. 3888-3892.
100. Dai, W., et al., *Mechanisms of the Deactivation of SAPO-34 Materials with Different Crystal Sizes Applied as MTO Catalysts.* ACS Catalysis, 2013. **3**(4): p. 588-596.
101. Pérez-Ramírez, J., et al., *Zeolite Catalysts with Tunable Hierarchy Factor by Pore-Growth Moderators.* Advanced Functional Materials, 2009. **19**(24): p. 3972-3979.

Appendices

Appendix A: Additional XRD results

Appendix B: Additional BET results

Appendix C: Additional ICP-MS results

Appendix D: Additional NO_x conversion results

Appendix E: Complete activity diagram of all reactions

Appendix F: Modelling of the bypass value

Appendix A: Additional XRD results

A change of tungsten filament was done for the XRD instrument after the calcination stage. This led to increased intensity of the diffractograms from ion exchange with ammonium nitrate, when normally the opposite is expected after aqueous ion exchange. Pointing out this parameter change explains this repeating trend for the relevant diffractograms in Appendix A.

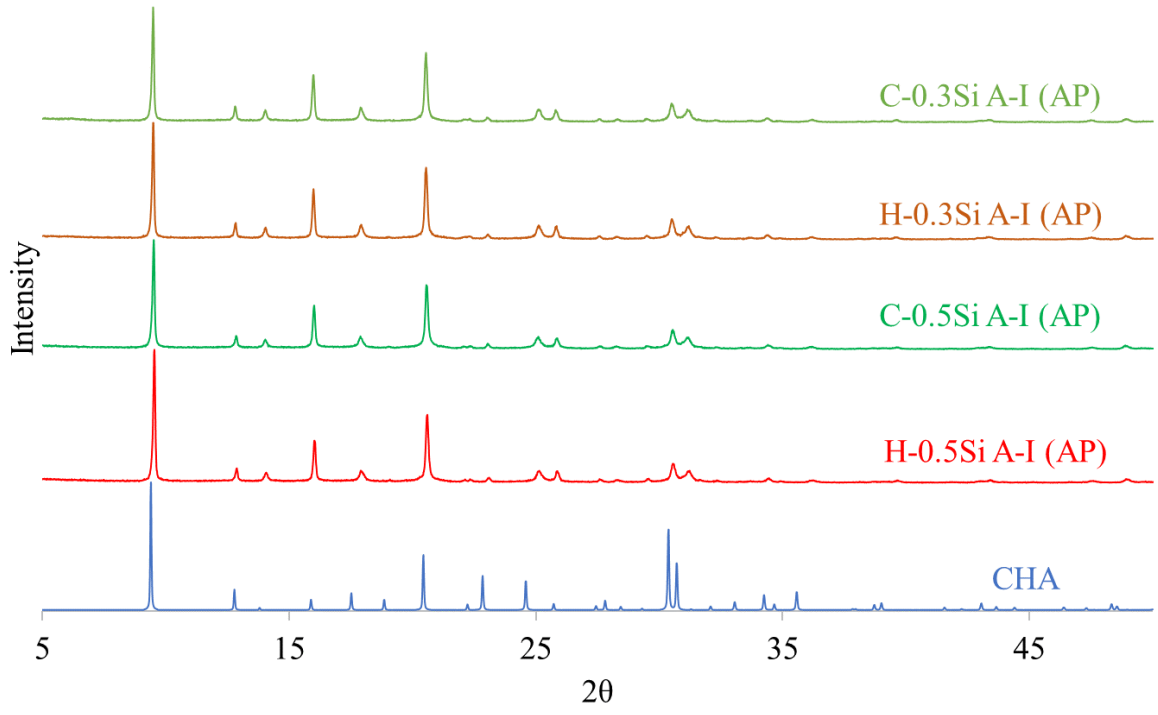

Figure A.1: Powder XRD diffractogram displaying the stacked diffractograms of the 4 “as prepared” (AP) samples in row 5, 6, 17, and 18 from Table 4-1.

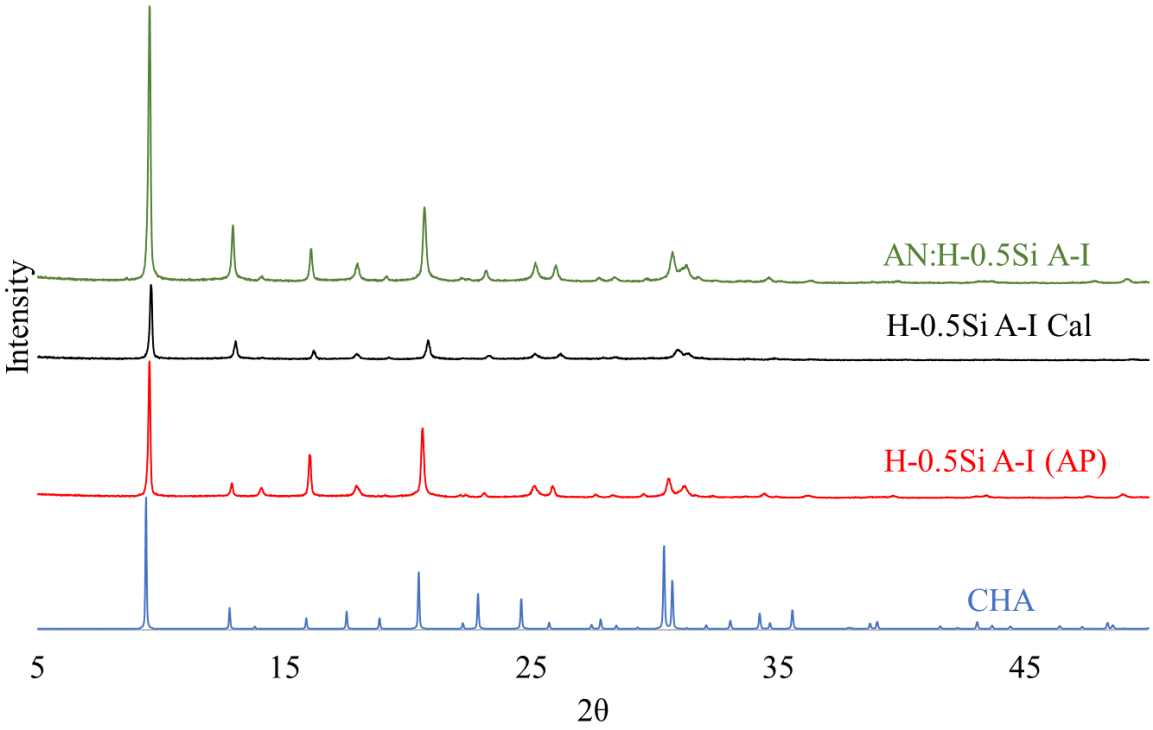

Figure A.2: Stacked diffractograms for H-0.5Si A-I from "as prepared" (AP) to ion exchange with ammonium nitrate (AN).

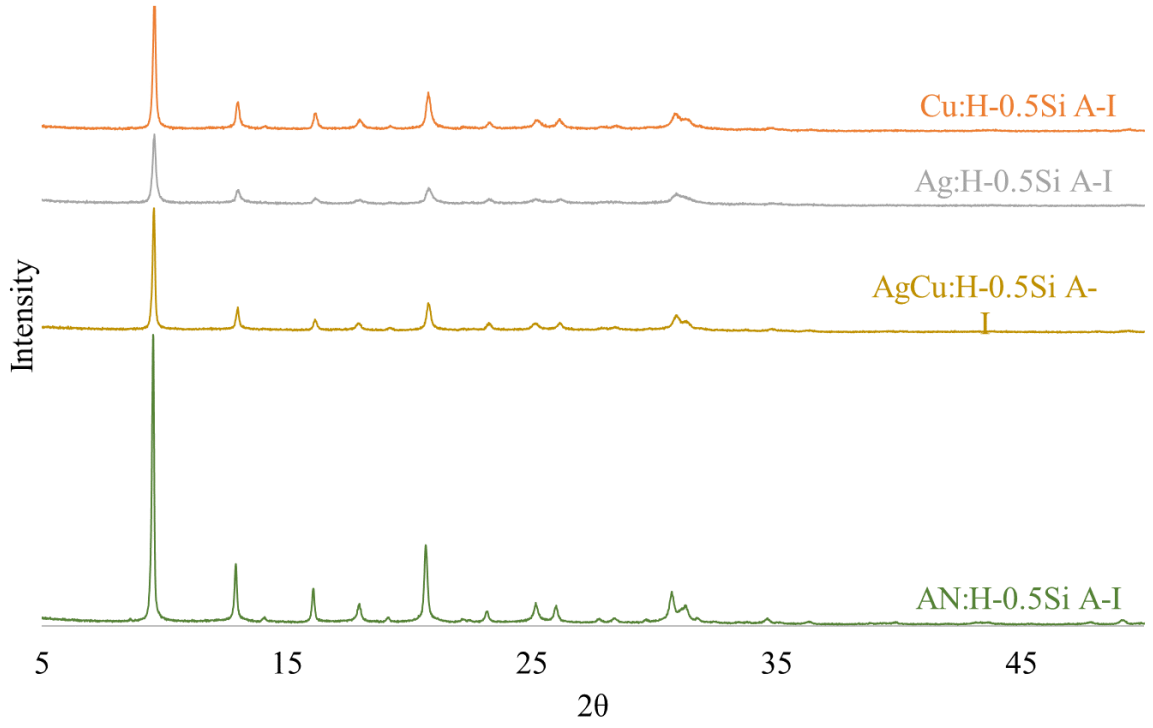

Figure A.3: Stacked diffractograms for H-0.5Si A-I from ion exchange with ammonium nitrate (AN) to ion exchange with AgCu, Ag^{+} and Cu^{2+}. Loss in intensity of the peaks is common for all 3, but ion exchange with Ag^{+} leads to the greatest loss.

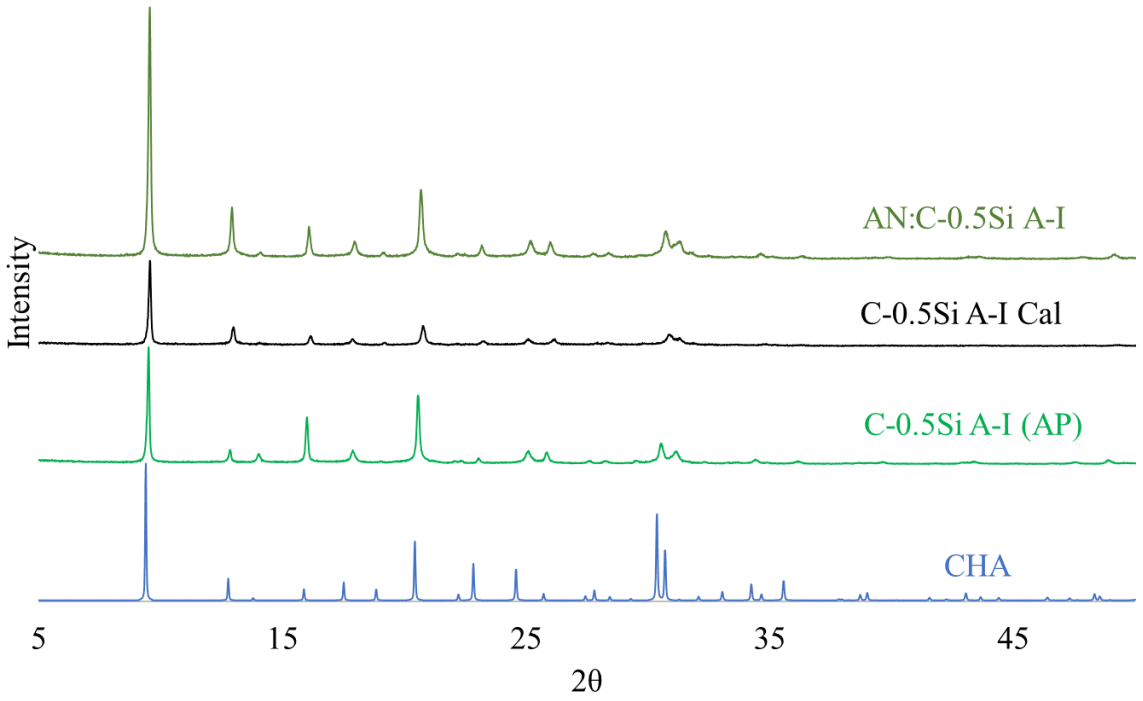

Figure A.4: Stacked diffractograms for C-0.5Si A-I from "as prepared" (AP) to ion exchange with ammonium nitrate (AN).

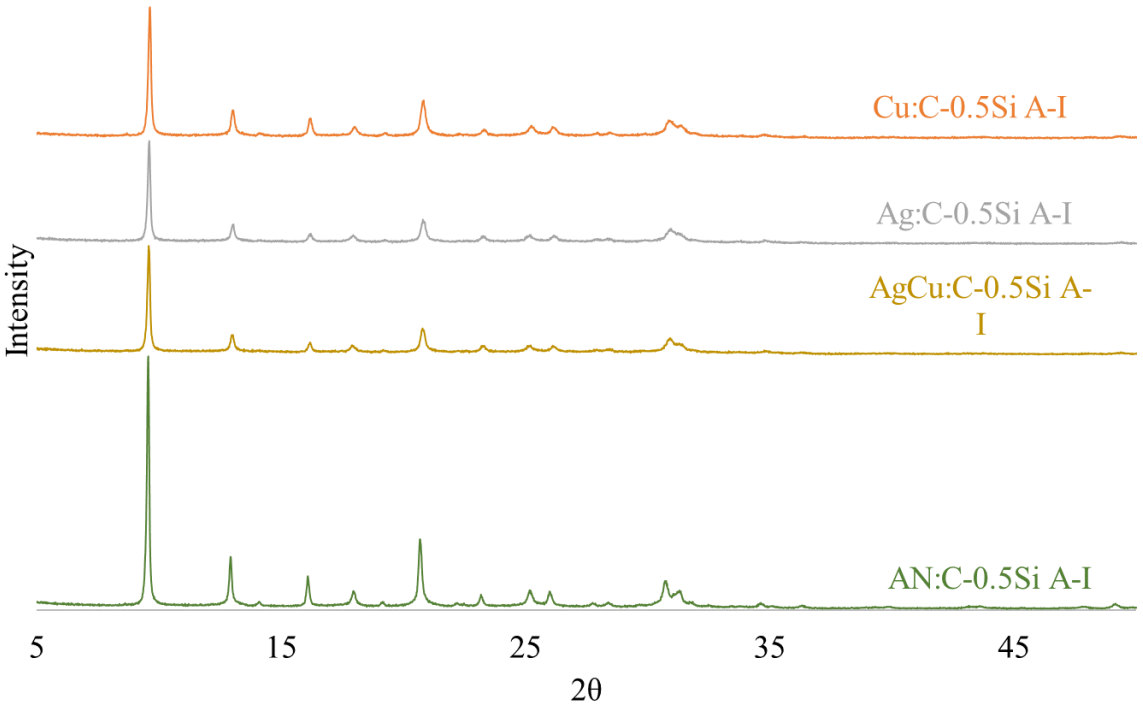

Figure A.5: Stacked diffractograms for C-0.5Si A-I from ion exchange with ammonium nitrate (AN) to ion exchange with AgCu, Ag^{+} and Cu^{2+}. Loss in intensity of the peaks is common for all 3, but ion exchange with Ag^{+} leads to the greatest loss.

D

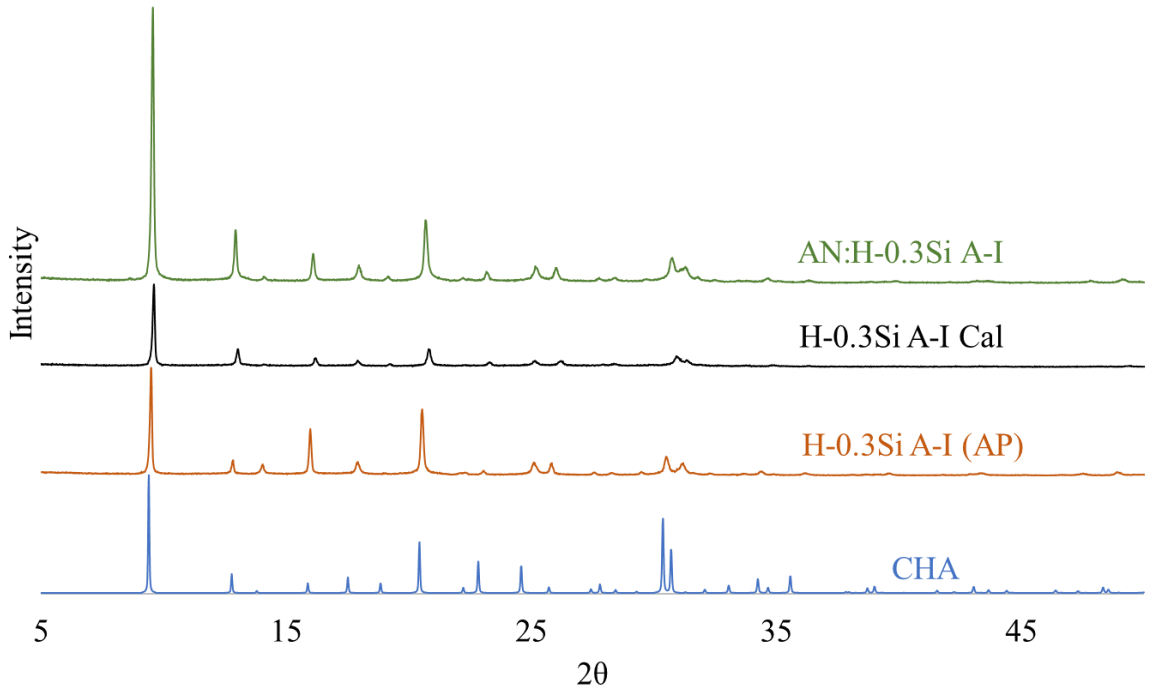

Figure A.6: Stacked diffractograms for H-0.3Si A-I from "as prepared" (AP) to ion exchange with ammonium nitrate (AN).

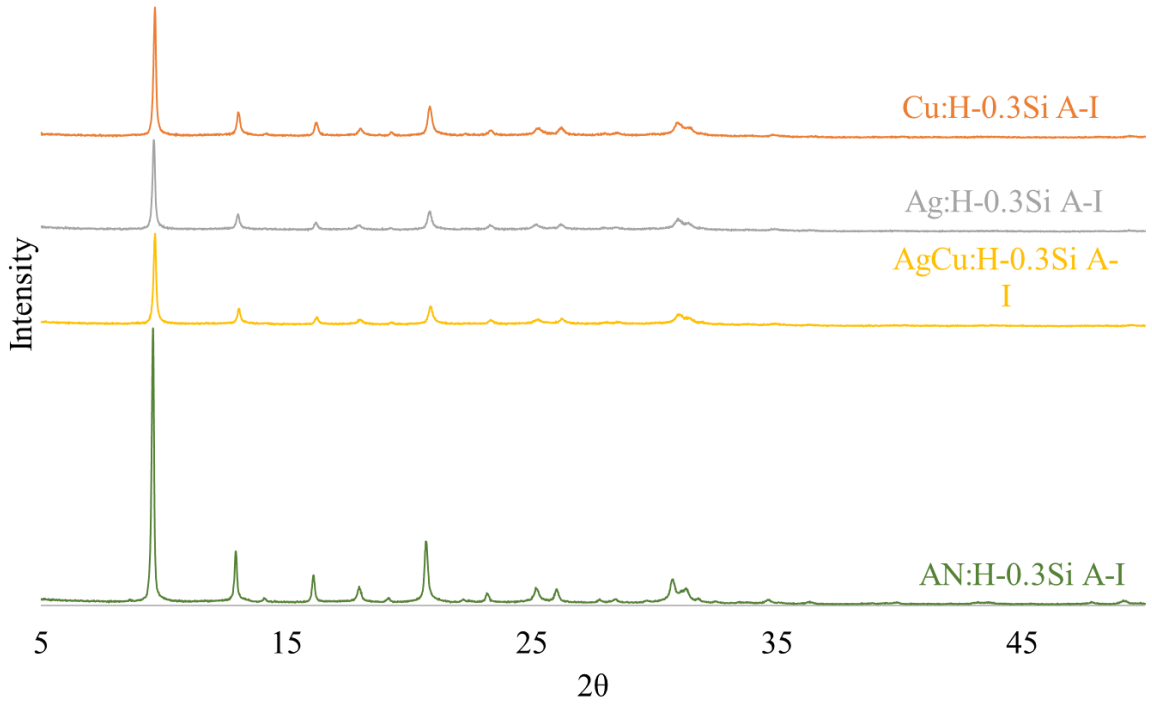

Figure A.7: Stacked diffractograms for H-0.3Si A-I from ion exchange with ammonium nitrate (AN) to ion exchange with AgCu, Ag^{+} and Cu^{2+}.

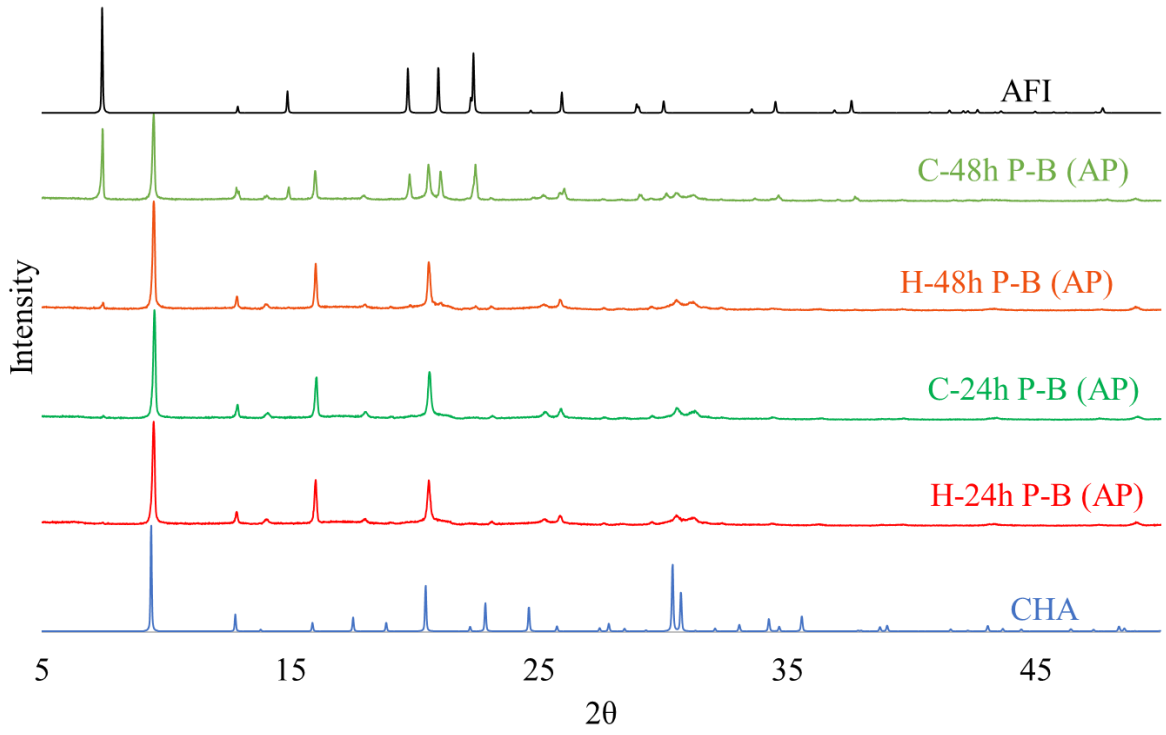

Figure A.8: Powder XRD diffractogram displaying the stacked diffractograms of the 4 “as prepared” (AP) samples in row 1, 2, 7, and 8 from Table 4-1.

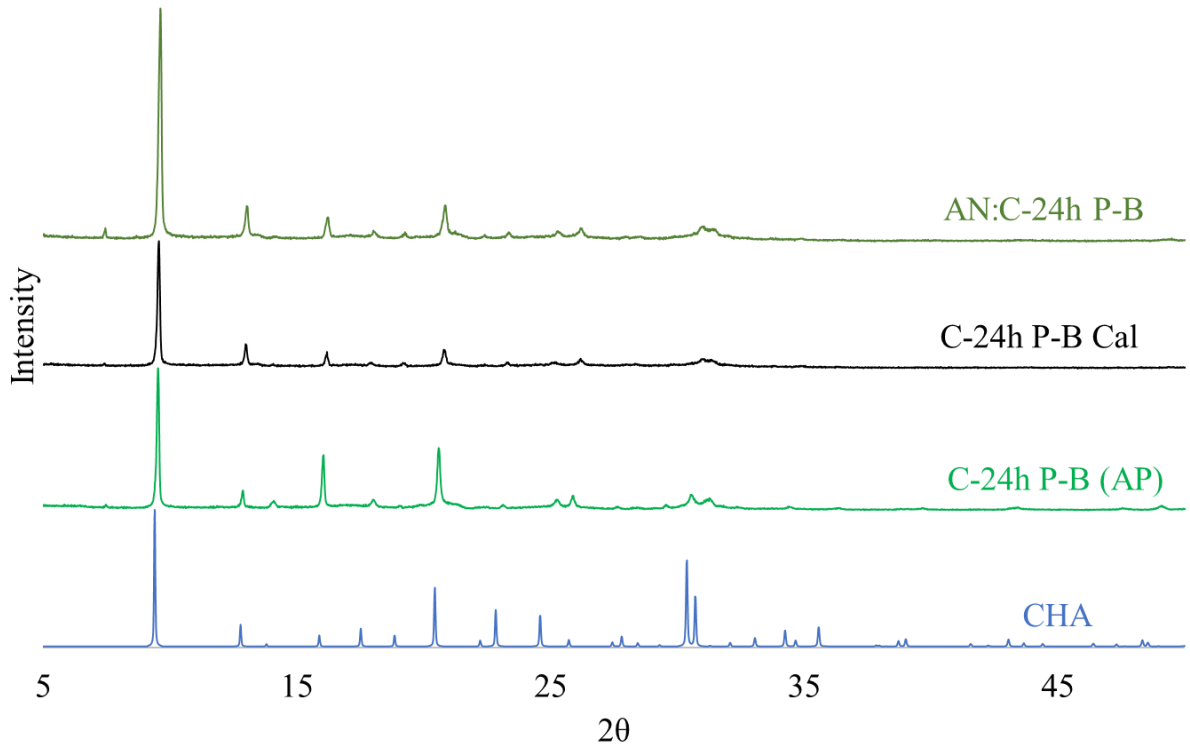

Figure A.9: Stacked diffractograms for C-24h P-B from “as prepared” (AP) to ion exchange with ammonium nitrate (AN).

F

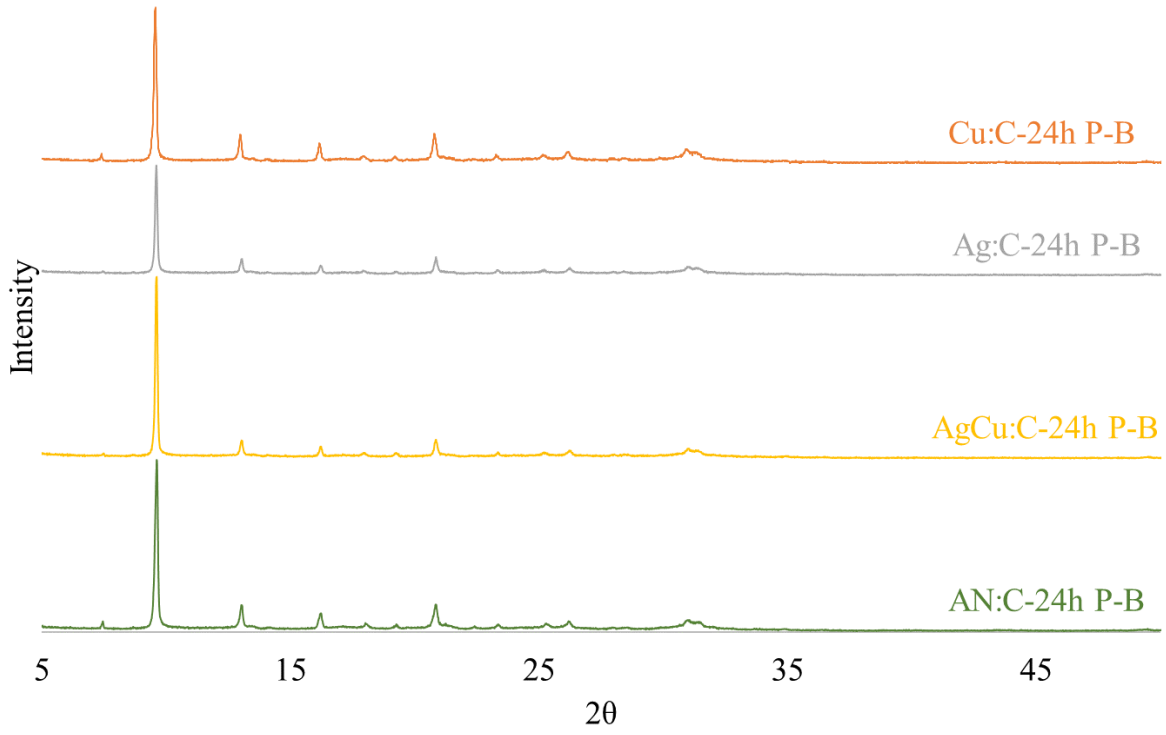

Figure A.10: Stacked diffractograms for C-24h P-B from ion exchange with ammonium nitrate (AN) to ion exchange with AgCu, Ag^{+} and Cu^{2+}.

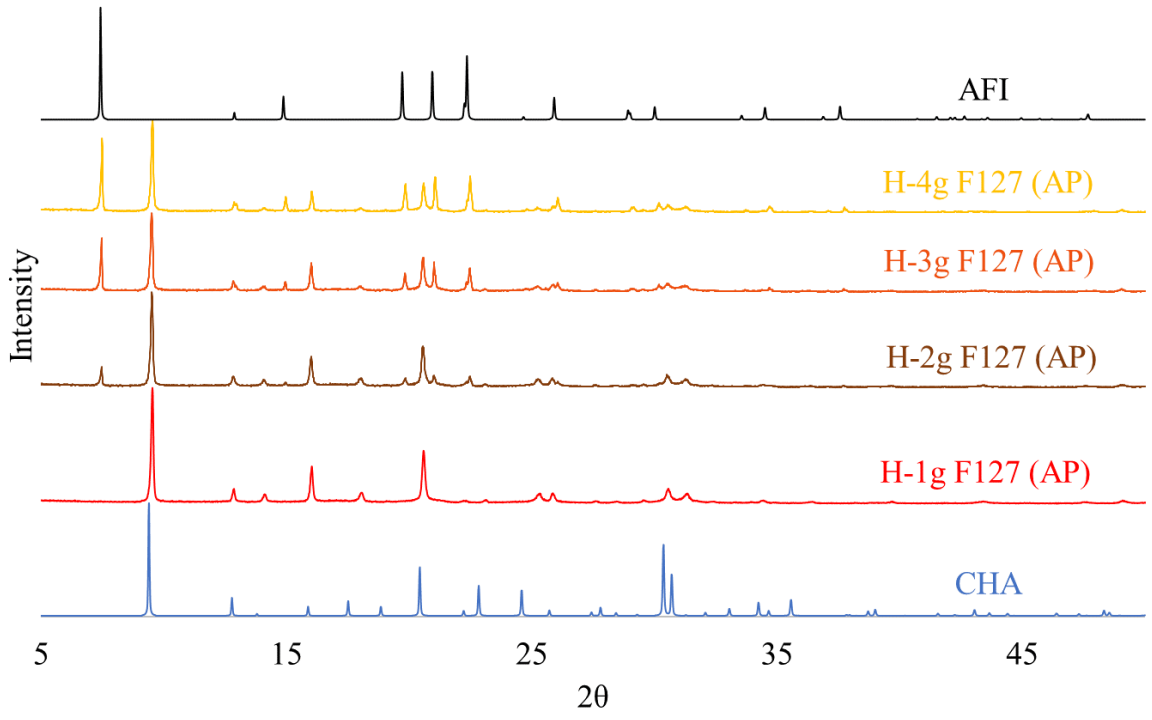

Figure A.11: Powder XRD diffractogram displaying the stacked diffractograms of the 4 “as prepared” (AP) samples in row 9, 10, 11 and 12 from Table 4-1.

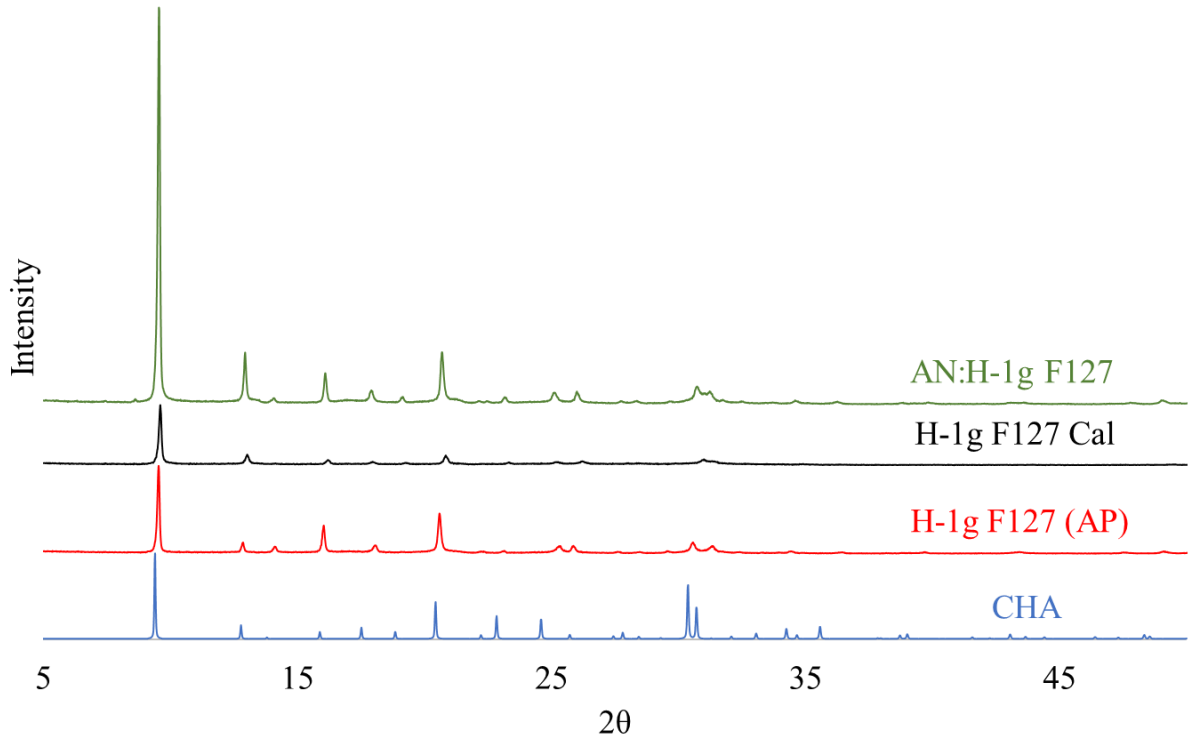

Figure A.12: Stacked diffractograms for H-1g F127 from "as prepared" (AP) to ion exchange with ammonium nitrate (AN).

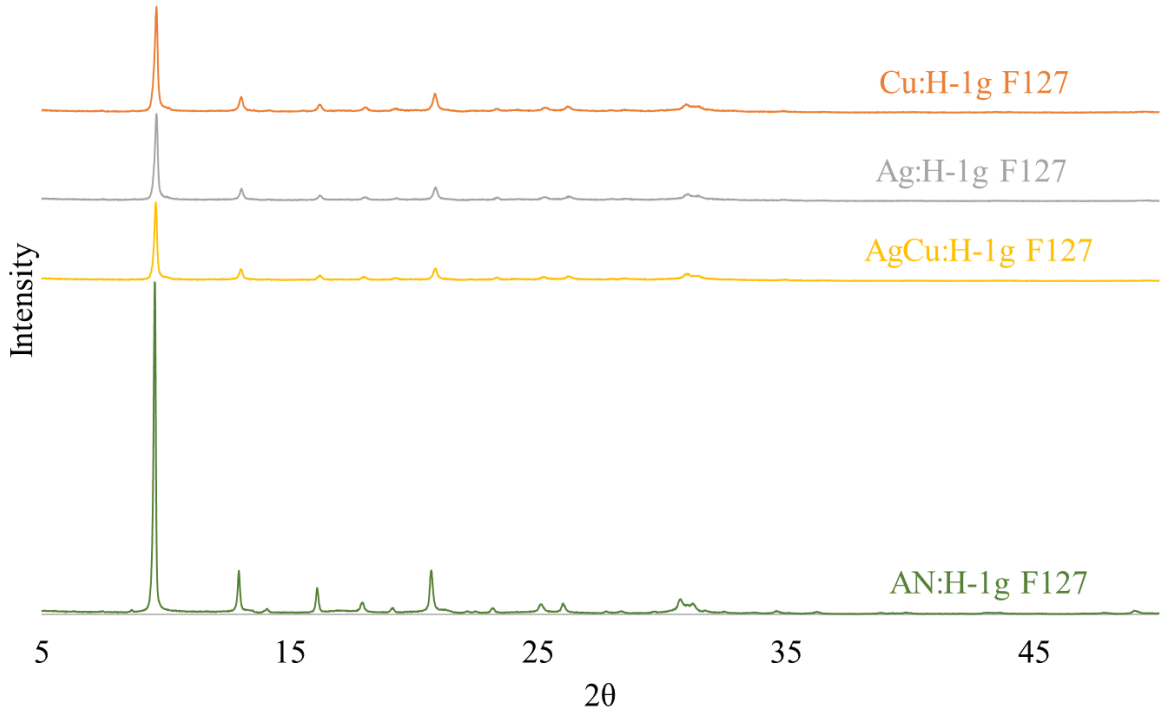

Figure A.13: Stacked diffractograms for H-1g F127 from ion exchange with ammonium nitrate (AN) to ion exchange with AgCu, Ag^{+} and Cu^{2+}.

H

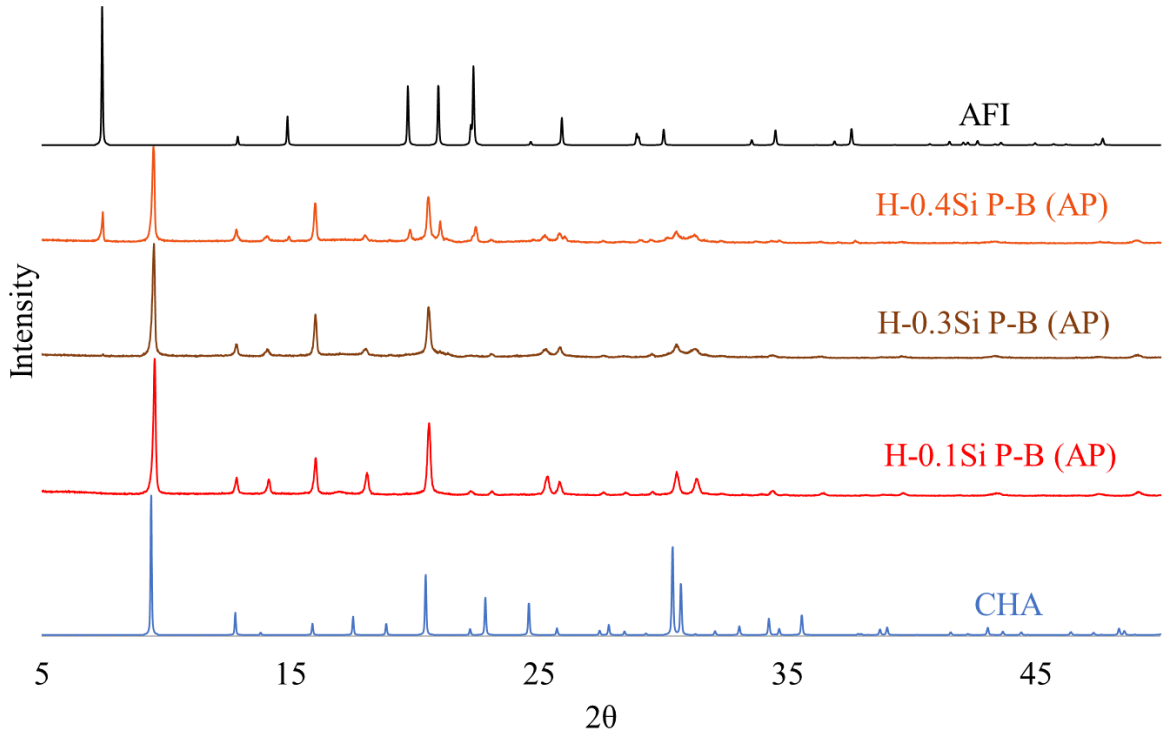

Figure A.14: Powder XRD diffractogram displaying the stacked diffractograms of the 4 “as prepared” (AP) samples in row 13, 14 and 15 from Table 4-1.

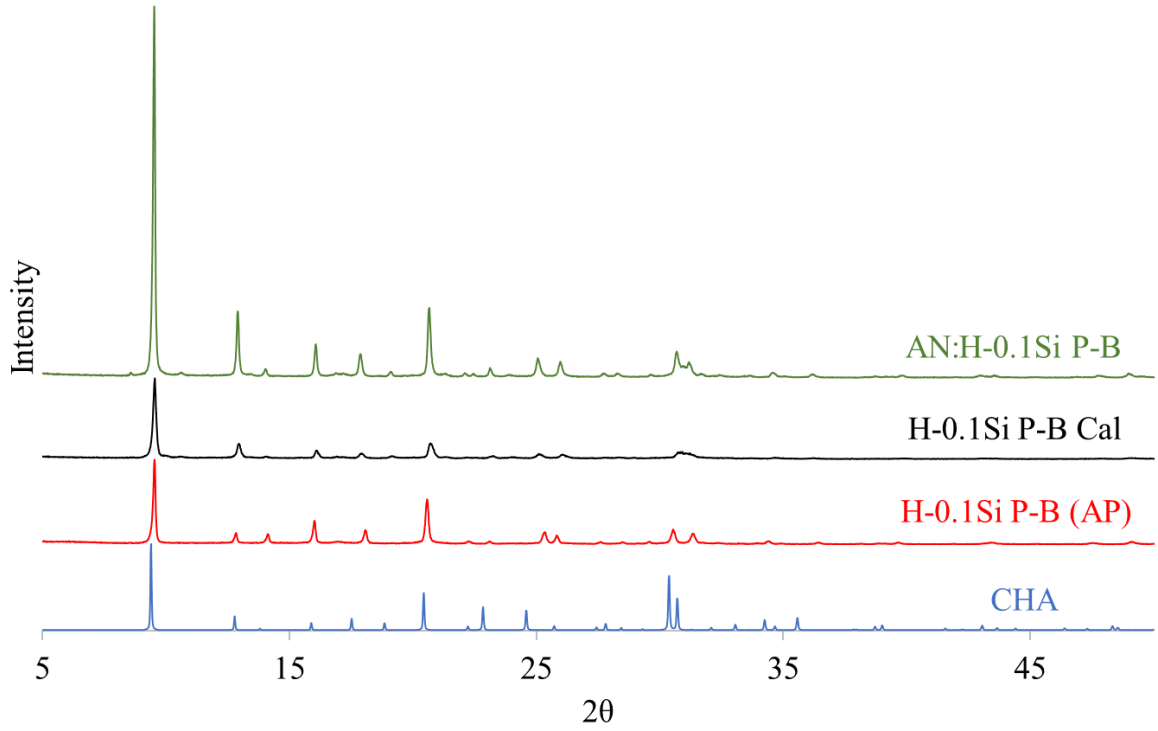

Figure A.15: Stacked diffractograms for H-0.1Si P-B from “as prepared” (AP) to ion exchange with ammonium nitrate (AN).

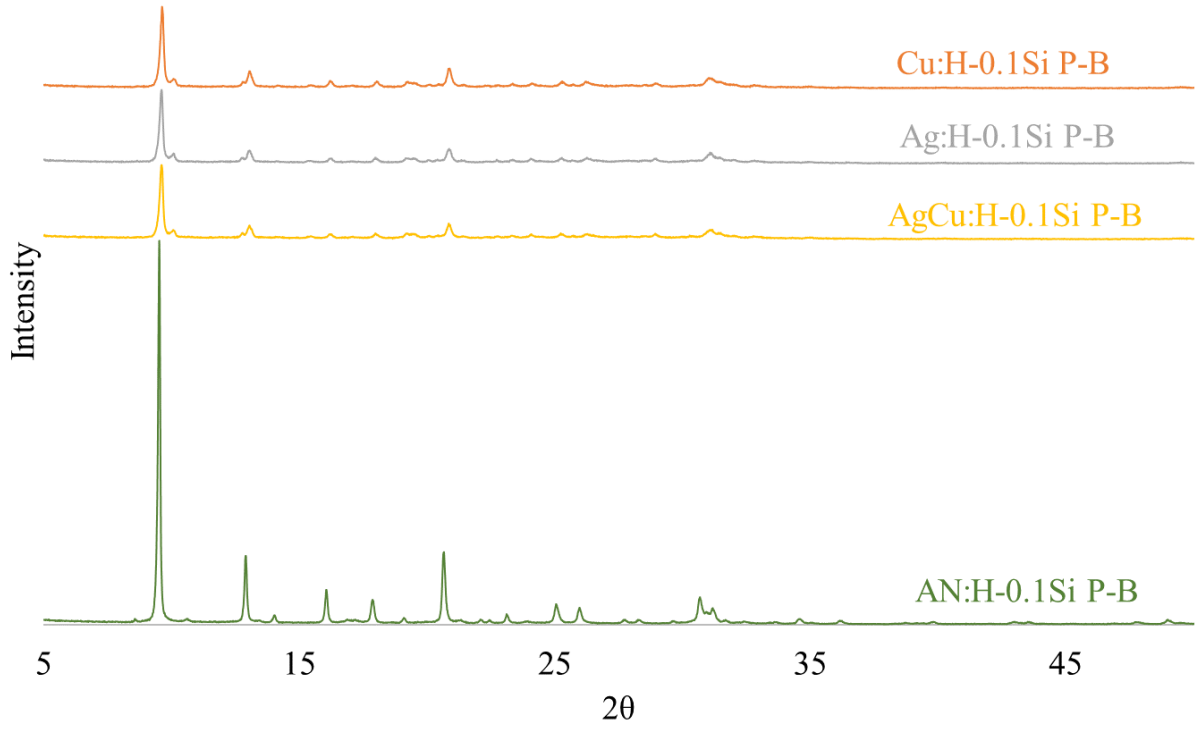

Figure A.16: Stacked diffractograms for H-0.1Si P-B from ion exchange with ammonium nitrate (AN) to ion exchange with AgCu, Ag^{+} and Cu^{2+}.

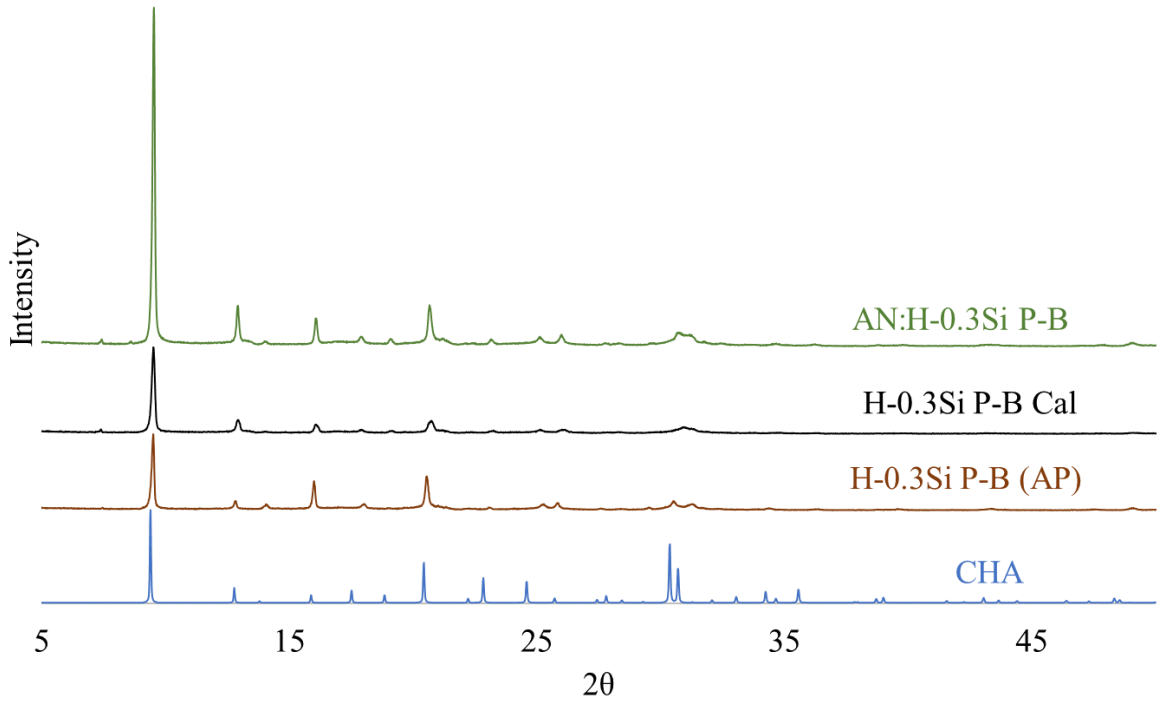

Figure A.17: Stacked diffractograms for H-0.3Si P-B from "as prepared" (AP) to ion exchange with ammonium nitrate (AN).

J

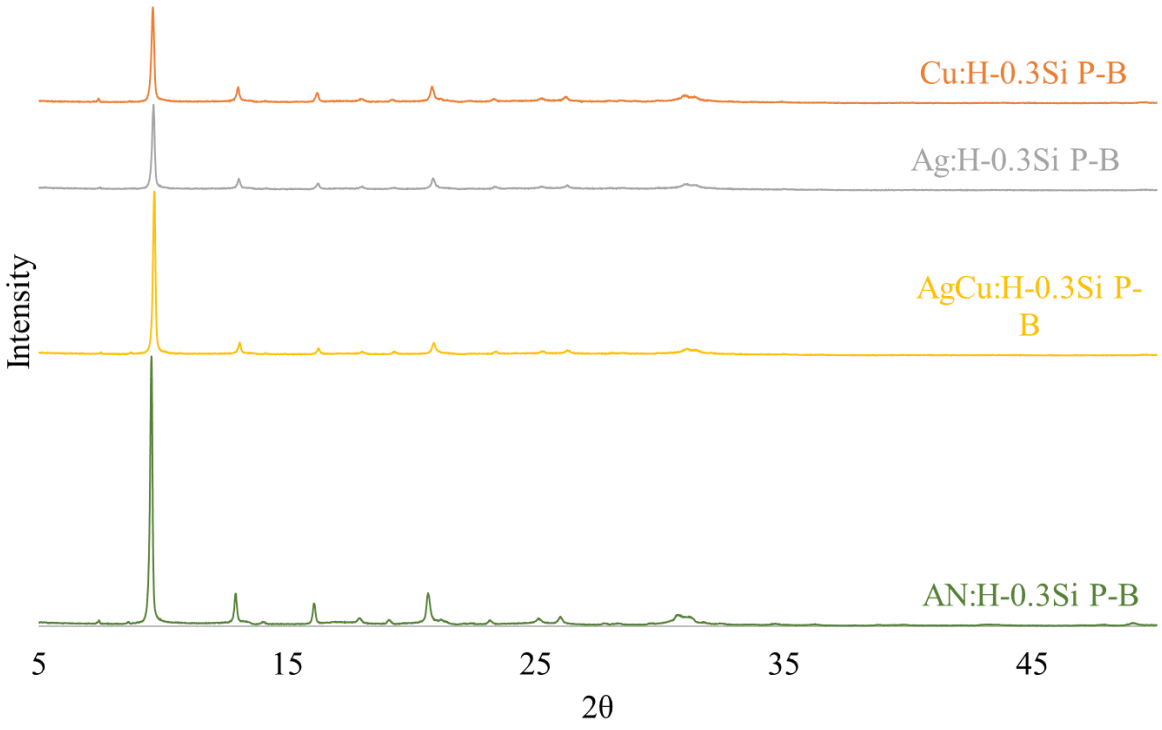

Figure A.18: Stacked diffractograms for H-0.3Si P-B from ion exchange with ammonium nitrate (AN) to ion exchange with AgCu, Ag^{+} and Cu^{2+}.

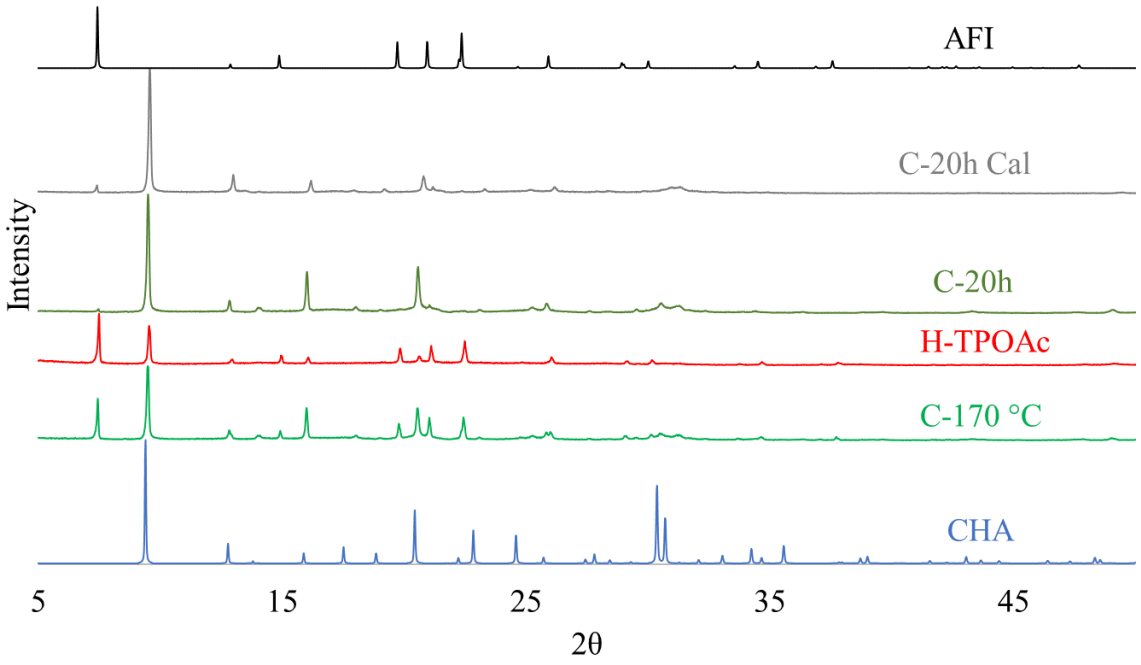

Figure A.19: Powder XRD diffractogram displaying the stacked diffractograms of the 3 “as prepared” (AP) samples in row 3, 4 and 16 from Table 4-1. The calcined diffractogram of the C-20h sample is displayed as well, but an AFI phase arose after calcination.

K

Appendix B: Additional BET results

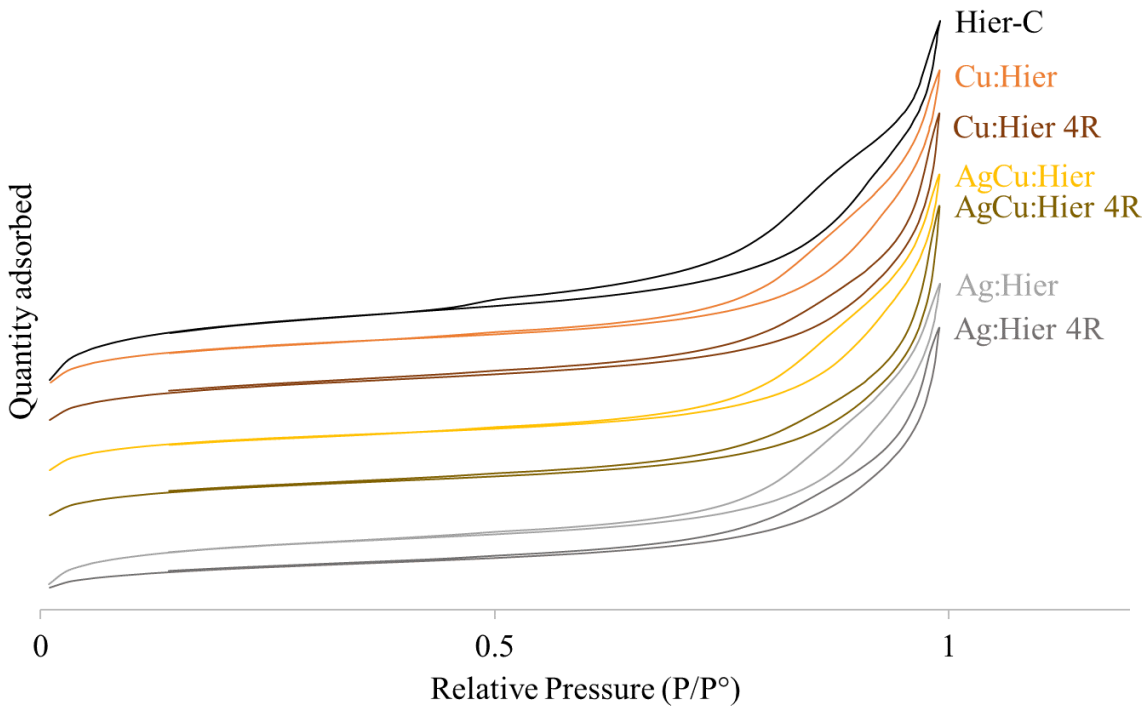

Figure B.1: Change in the adsorption isotherm hysteresis for H-0.5Si A-I from calcination towards 1 round of ion exchange and 4 rounds of ion exchange with AgCu, Ag^{+} and Cu^{2+}. The curves are stacked.

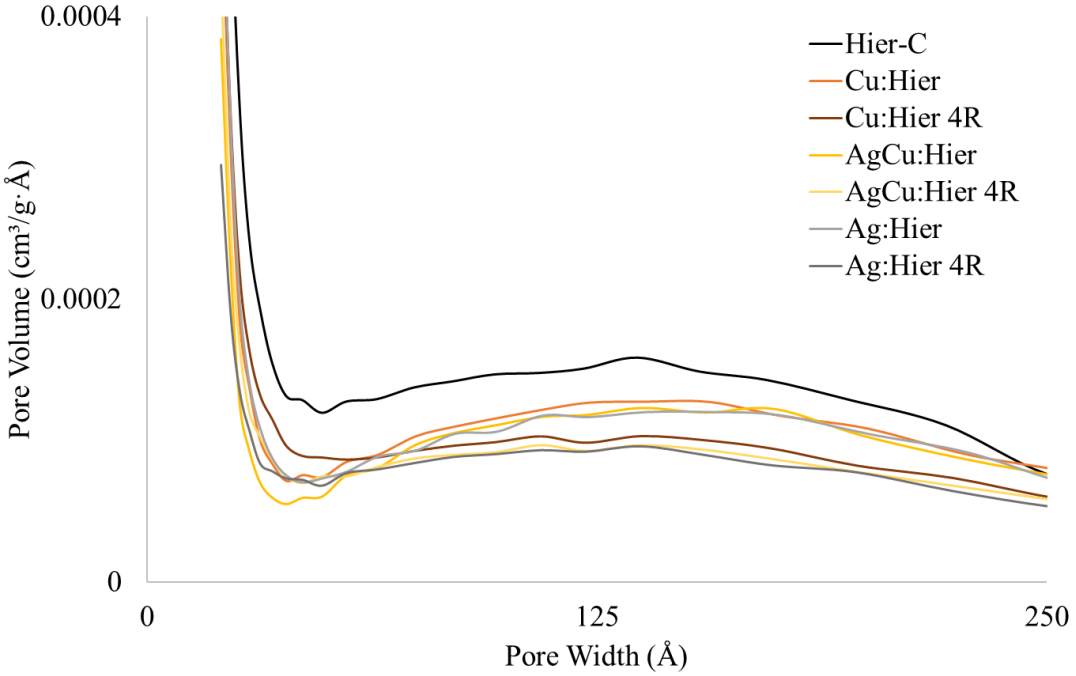

Figure B.2: Change in PSD of the H-0.5Si A-I sample after calcination, 1 round of ion exchange and 4 rounds of ion exchange with AgCu, Ag^{+} and Cu^{2+}.

L

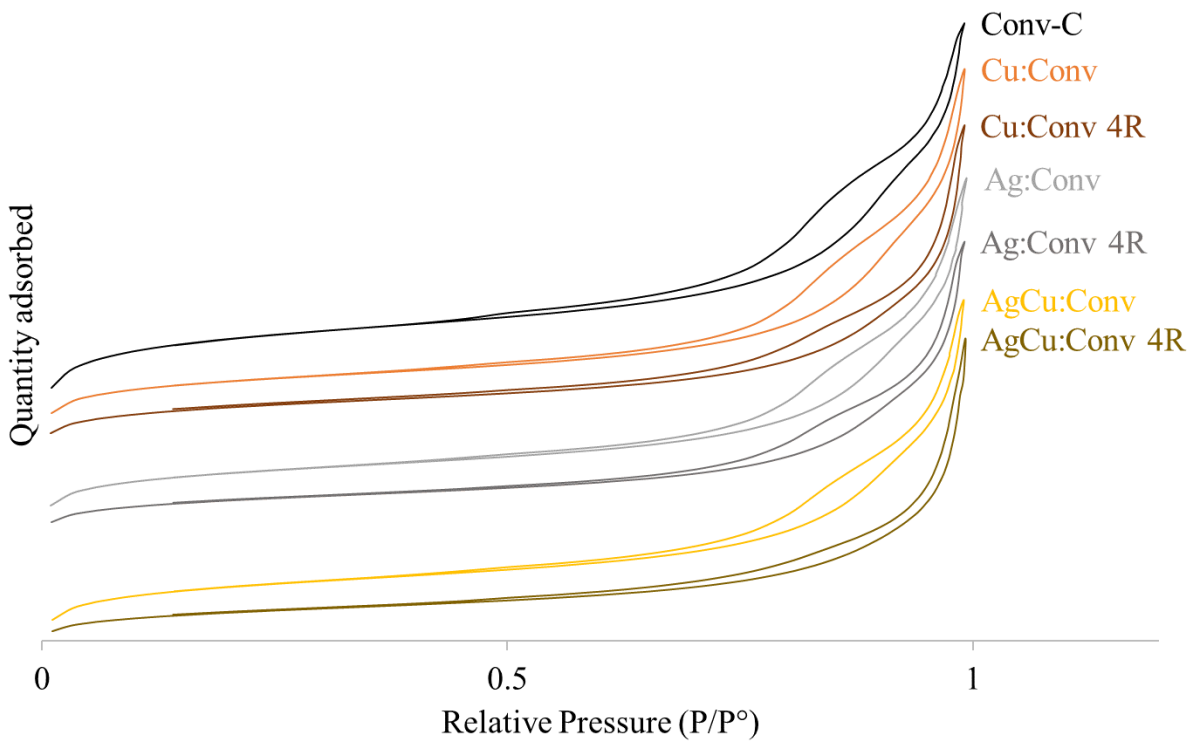

Figure B.3: Change in the adsorption isotherm hysteresis for C-0.5Si A-I from calcination towards 1 round of ion exchange and 4 rounds of ion exchange with AgCu, Ag^{+} and Cu^{2+}. The curves are stacked.

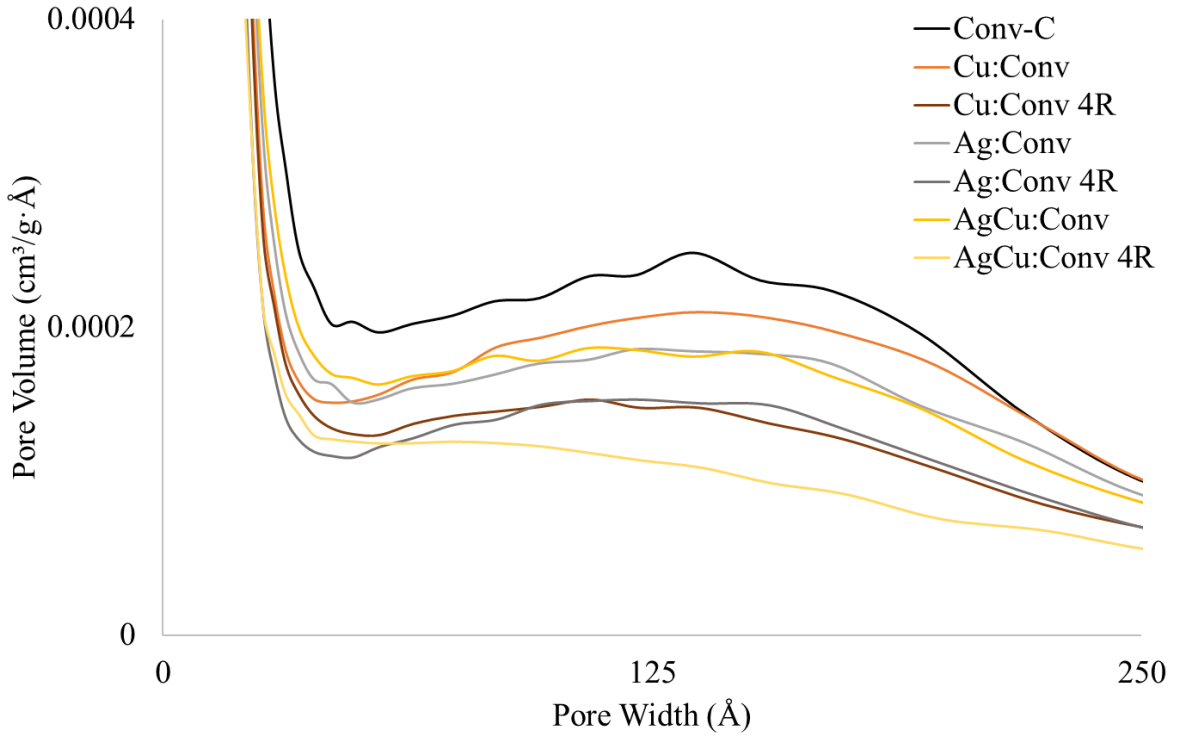

Figure B.4: PSD of the Conv sample after calcination, 1 round of ion exchange and 4 rounds of ion exchange with AgCu, Ag^{+} and Cu^{2+}.

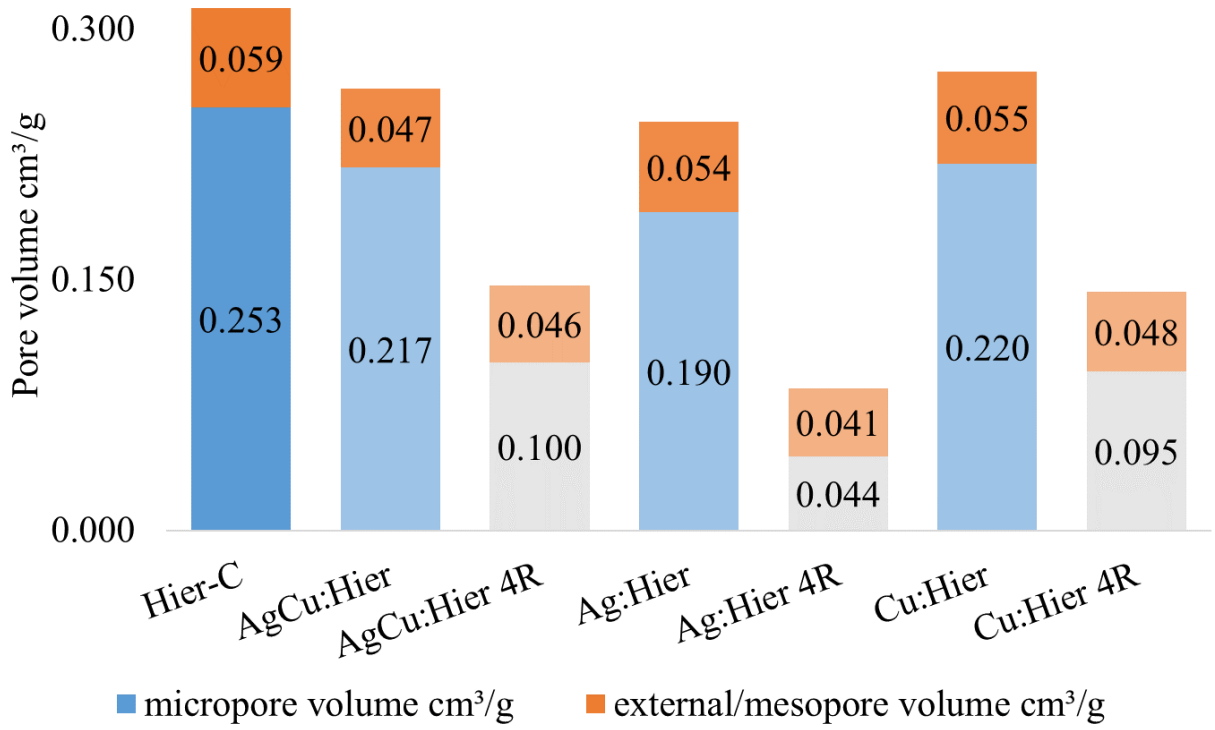

Figure B.5: Change in pore volume distributed between micro- and mesopore volume, for H-0.5Si A-I calcined (Hier-C) and after 1 round and 4 rounds of ion exchange.

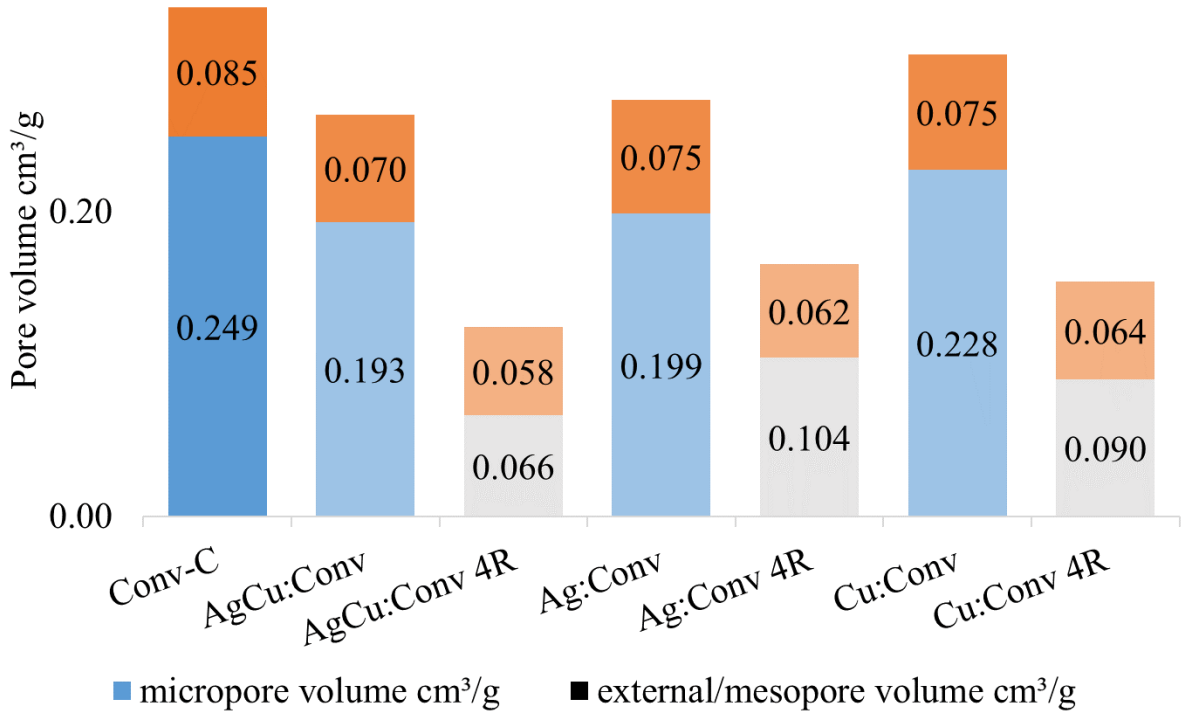

Figure B.6: Change in pore volume distributed between micro- and mesopore volume, for C-0.5Si A-I calcined (Conv-C) and after 1 round and 4 rounds of ion exchange.

N

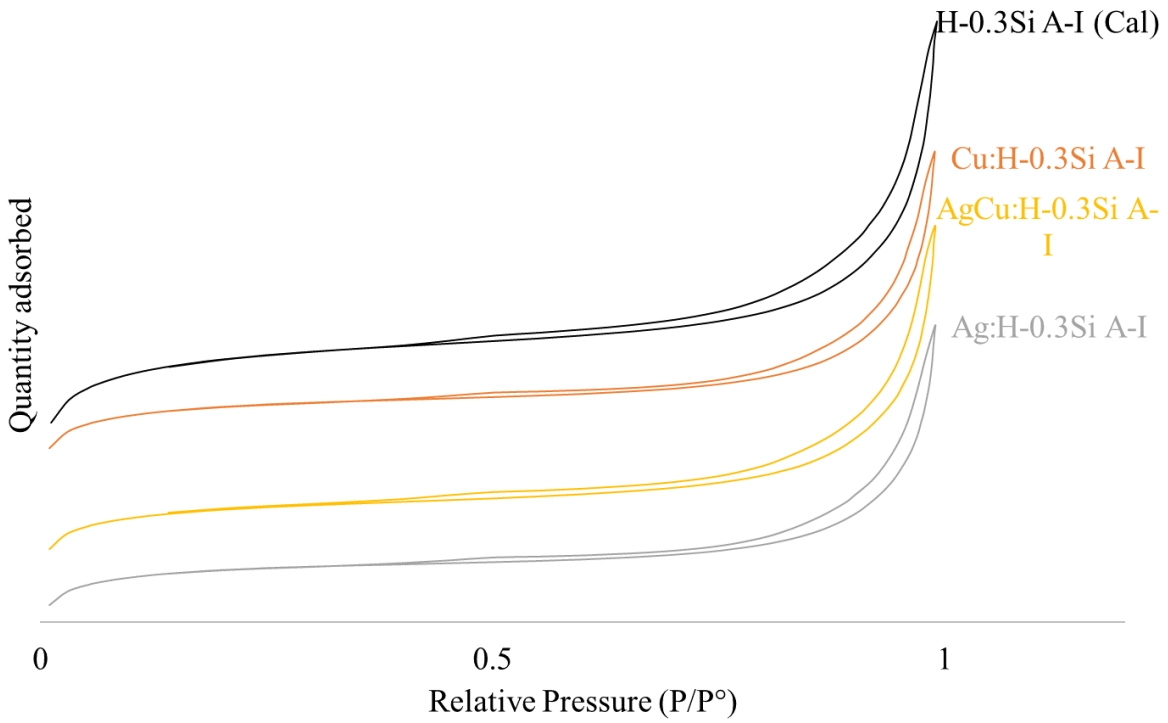

Figure B.7: Change in the isothermal hysteresis before and after ion exchange for H-0.3Si A-I. The curves are stacked.

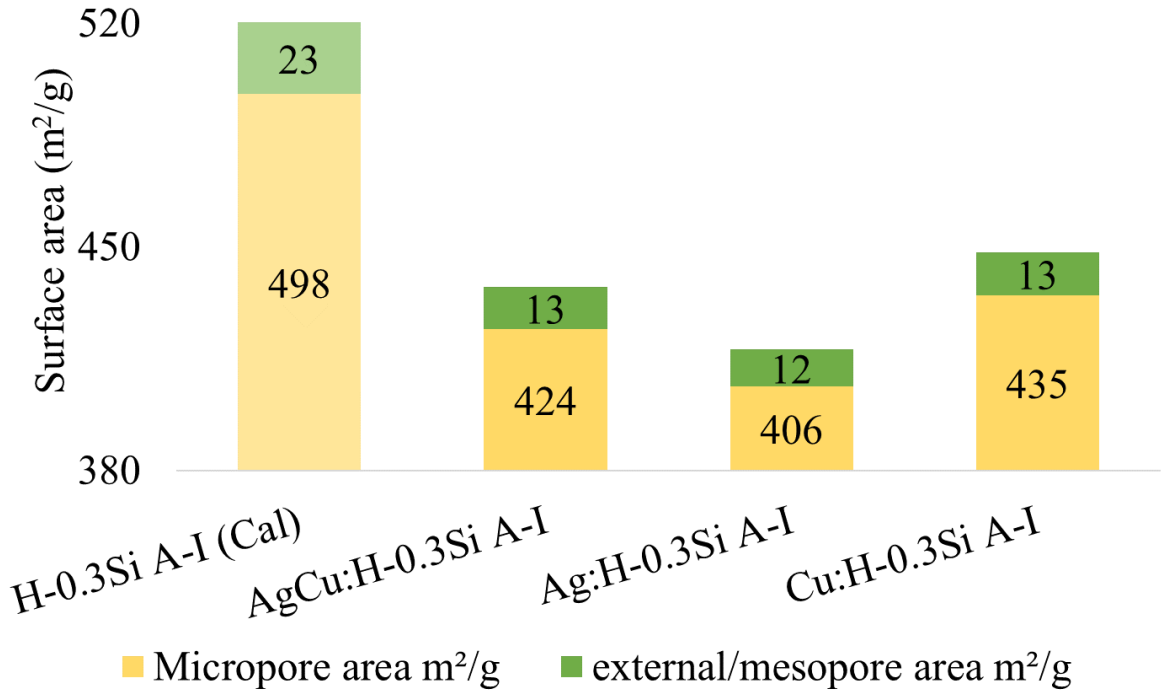

Figure B.8:Pore surface area belonging to the micro- and meso range of the H-0.3Si A-I before and after ion exchange.

O

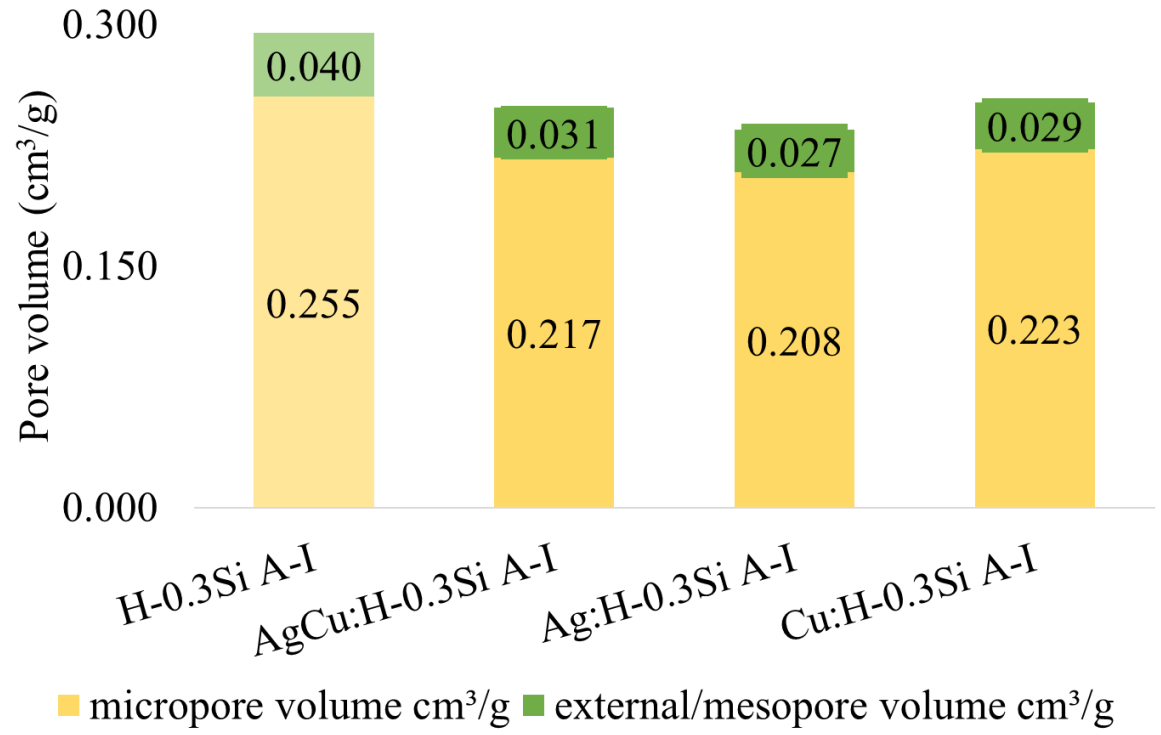

Figure B.9: Pore volume belonging to the micro- and meso range of H-0.3Si A-I before and after ion exchange.

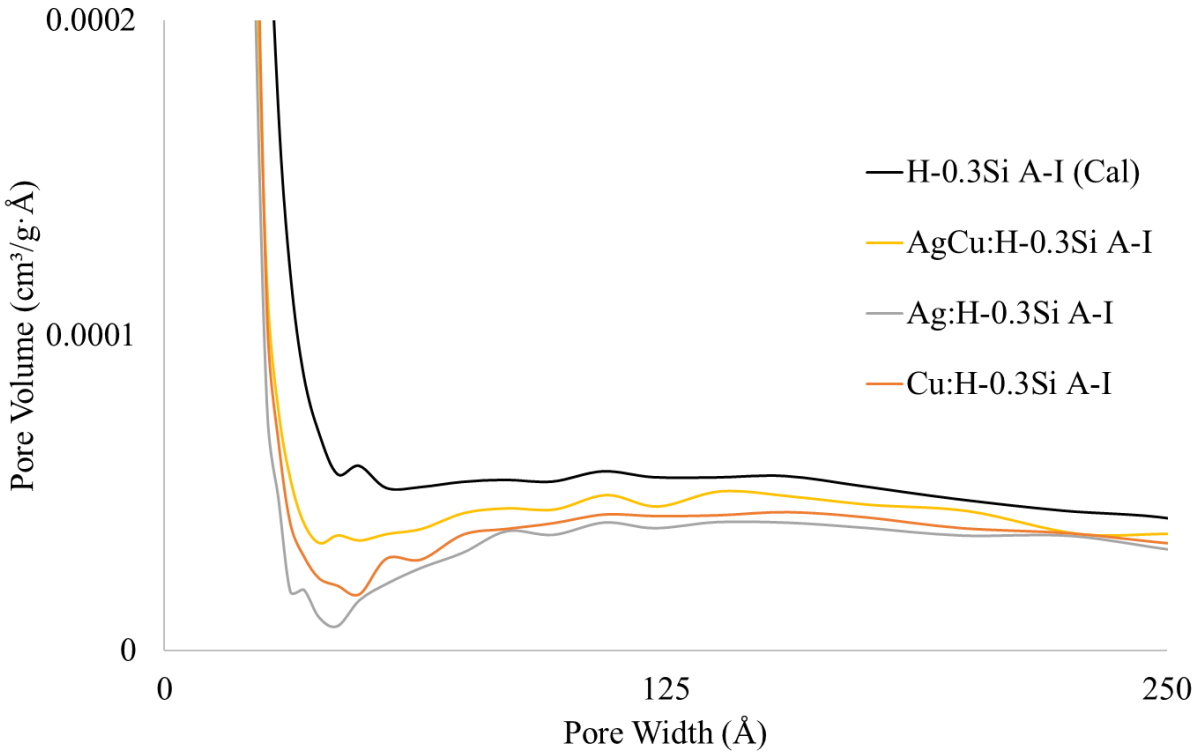

Figure B.10: Change in PSD in the micro- and meso range for H-0.3Si A-I before and after ion exchange.

P

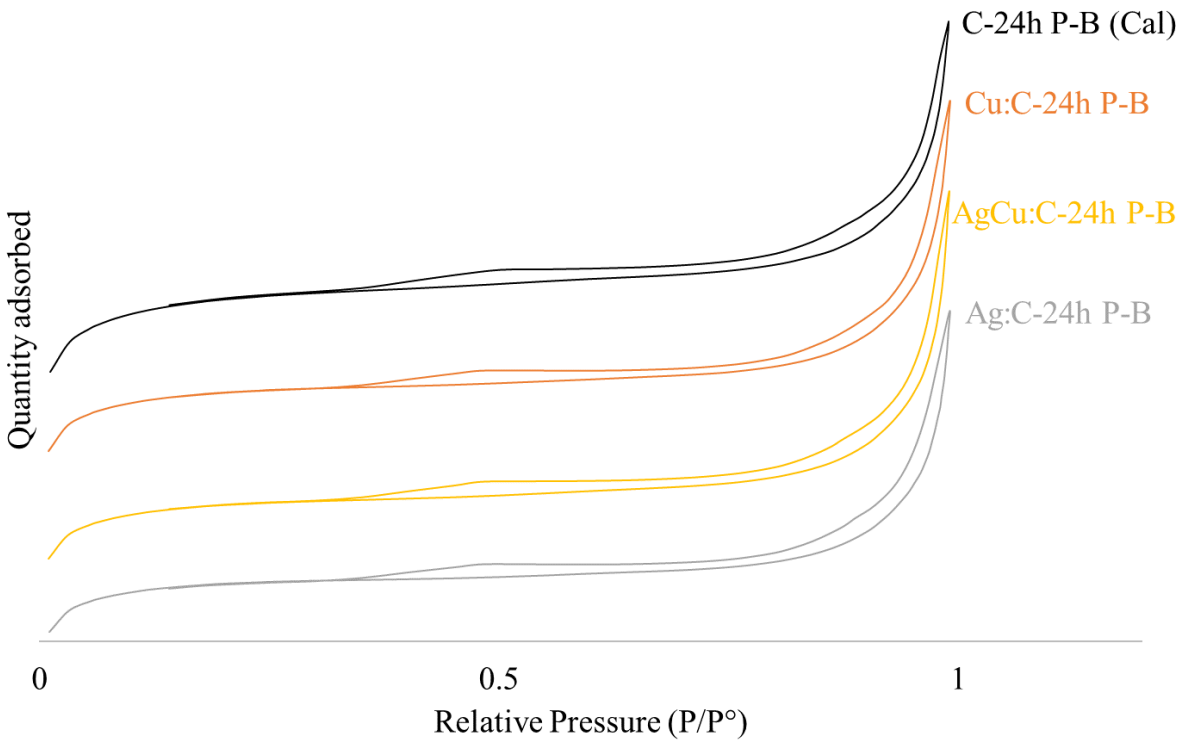

Figure B.11: Change in the isothermal hysteresis before and after ion exchange for C-24h P-B. The curves are stacked.

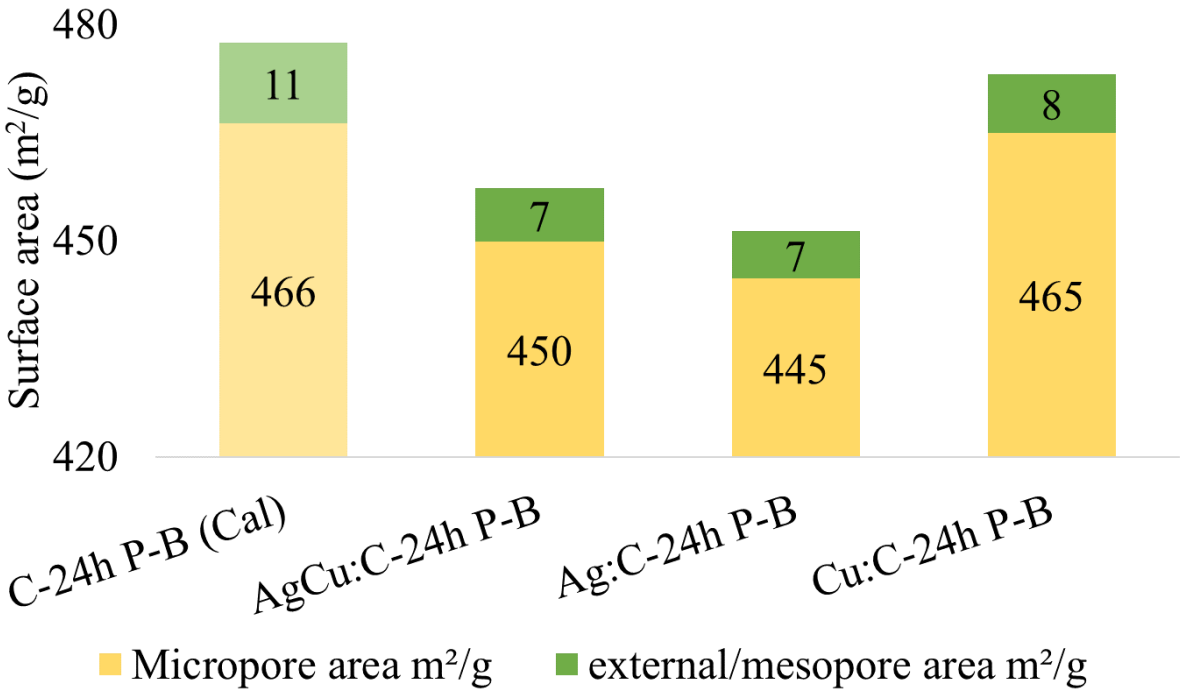

Figure B.12: Pore surface area belonging to the micro- and meso range of C-24h P-B before and after ion exchange.

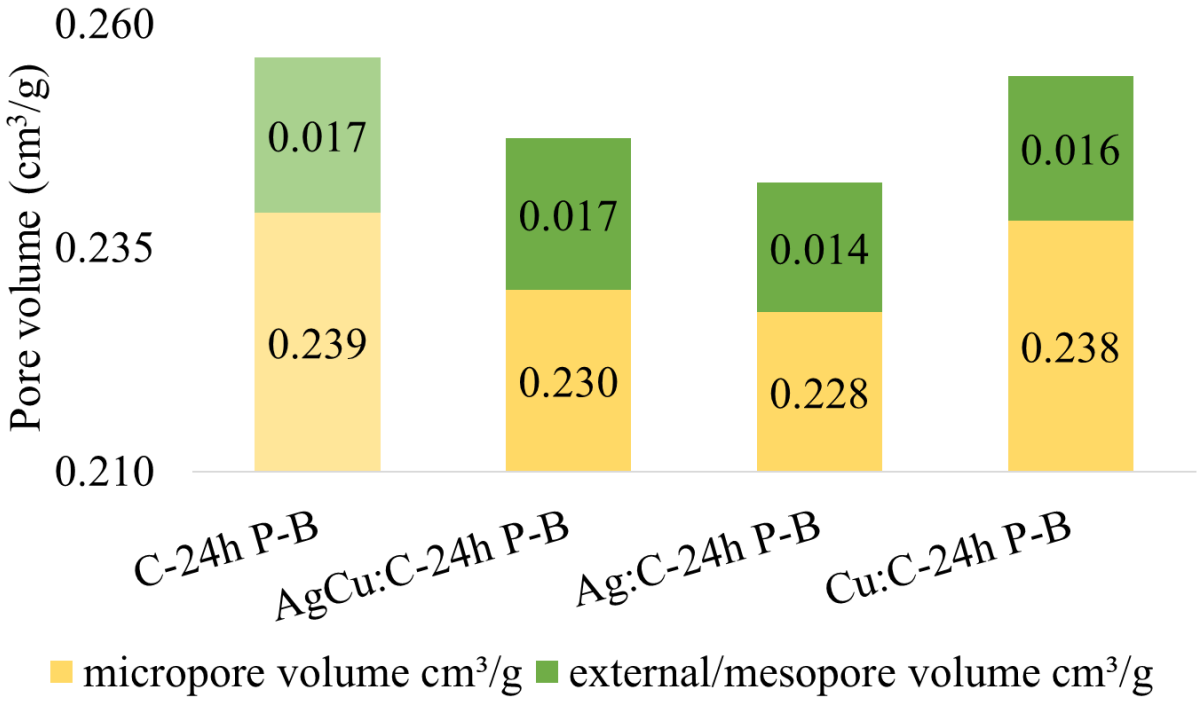

Figure B.13: Pore volume belonging to the micro- and meso range of C-24h P-B before and after ion exchange.

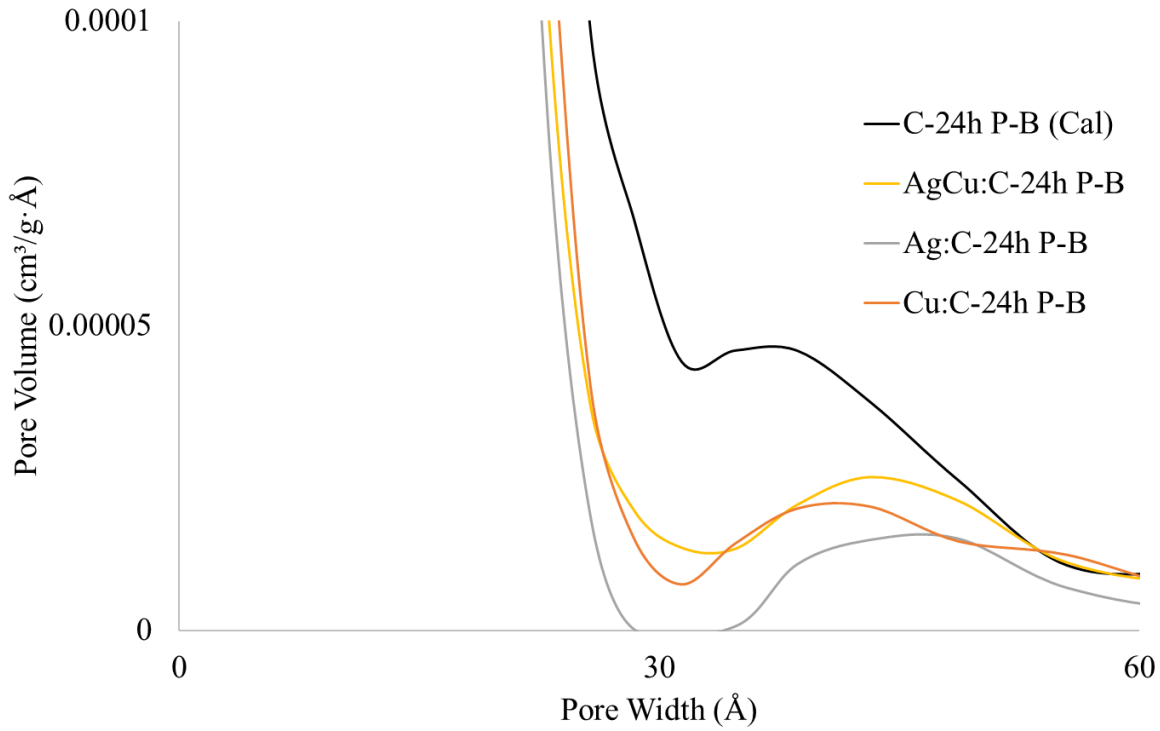

Figure B.14: Change in PSD in the micro and meso range for C-24h P-B before and after ion exchange.

R

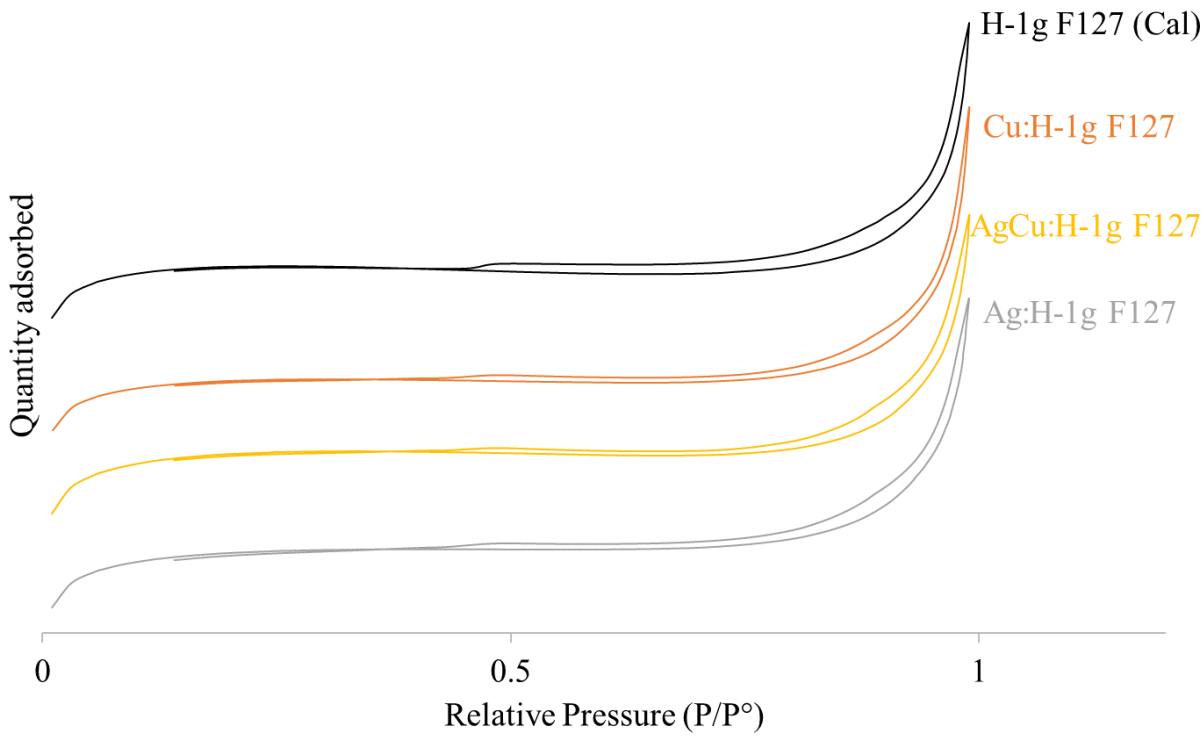

Figure B.15: Change in the isothermal hysteresis before and after ion exchange for H-1g F127. The curves are stacked.

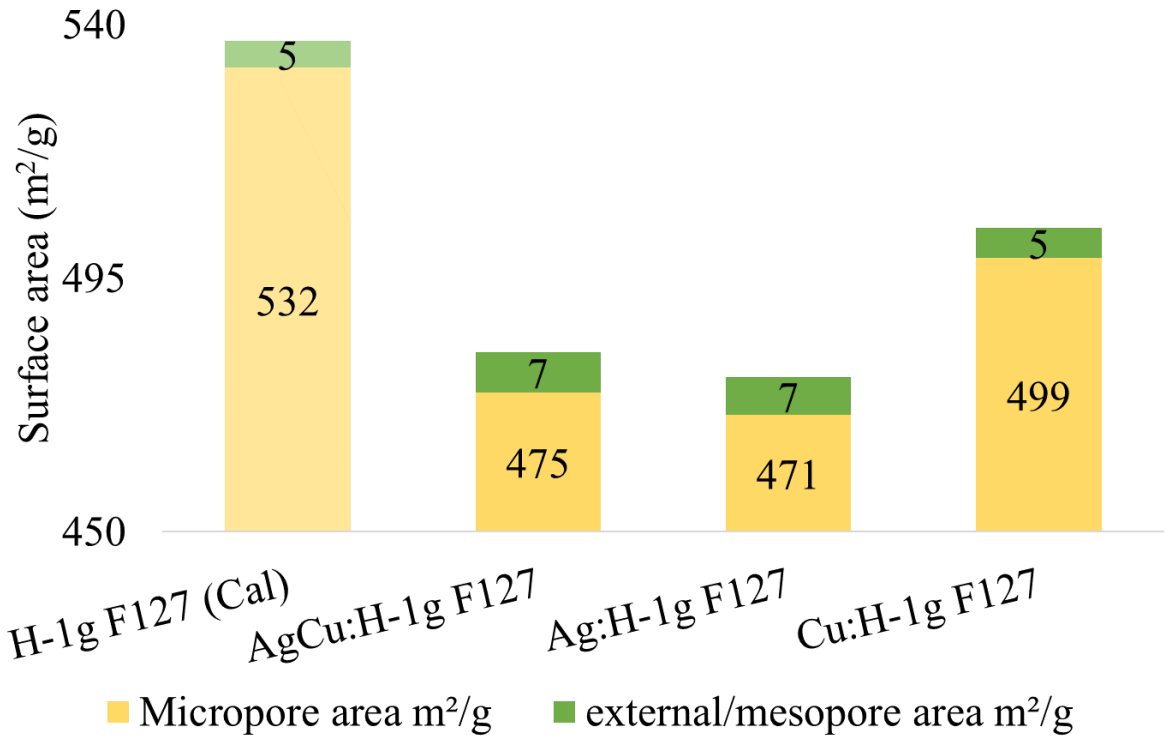

Figure B.16: Pore surface area belonging to the micro- and meso range of H-1g F127 before and after ion exchange.

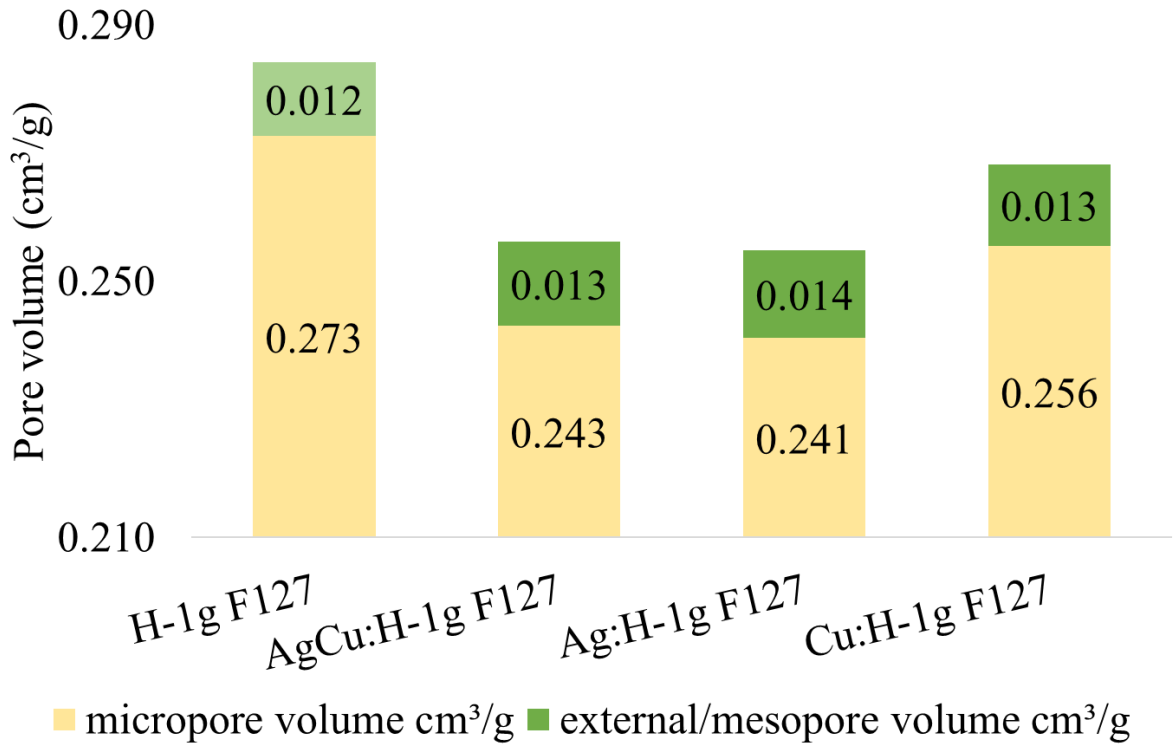

Figure B.17: Pore volume belonging to the micro- and meso range of H-1g F127 before and after ion exchange.

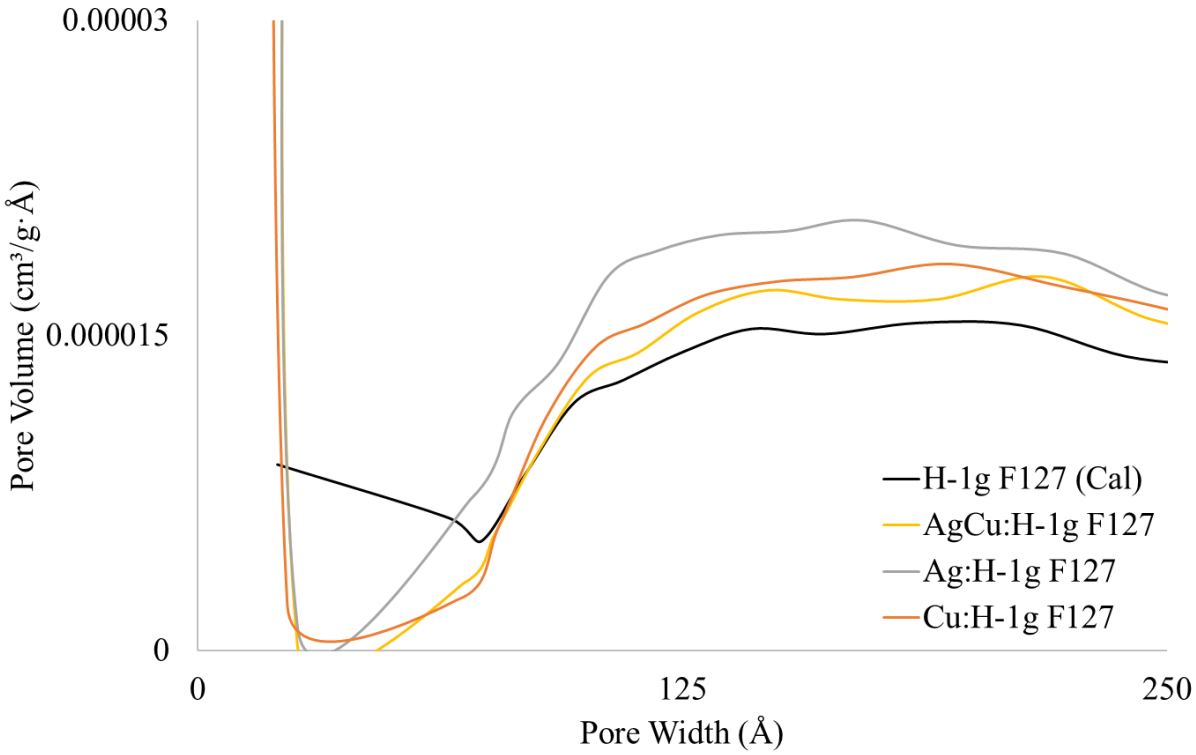

Figure B.18: Change in PSD in the micro and meso range for H-1g F127 before and after ion exchange.

T

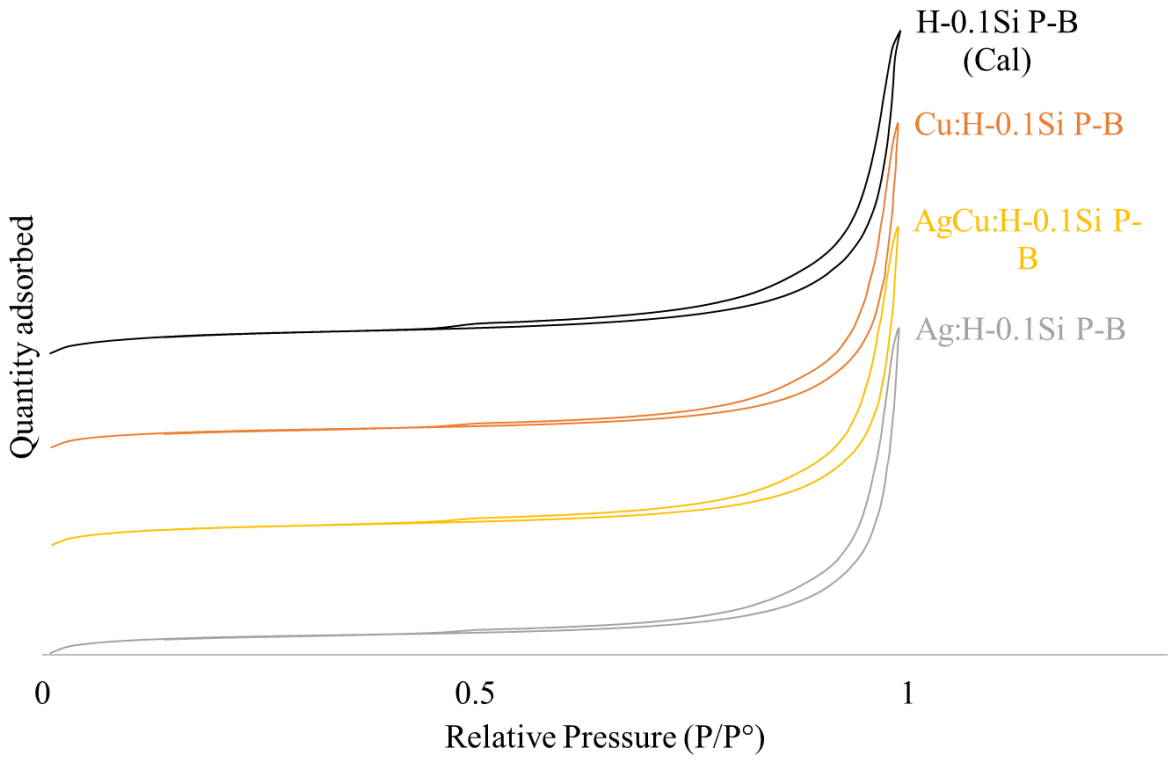

Figure B.19: Change in the isothermal hysteresis before and after ion exchange for H-0.1Si P-B. The curves are stacked.

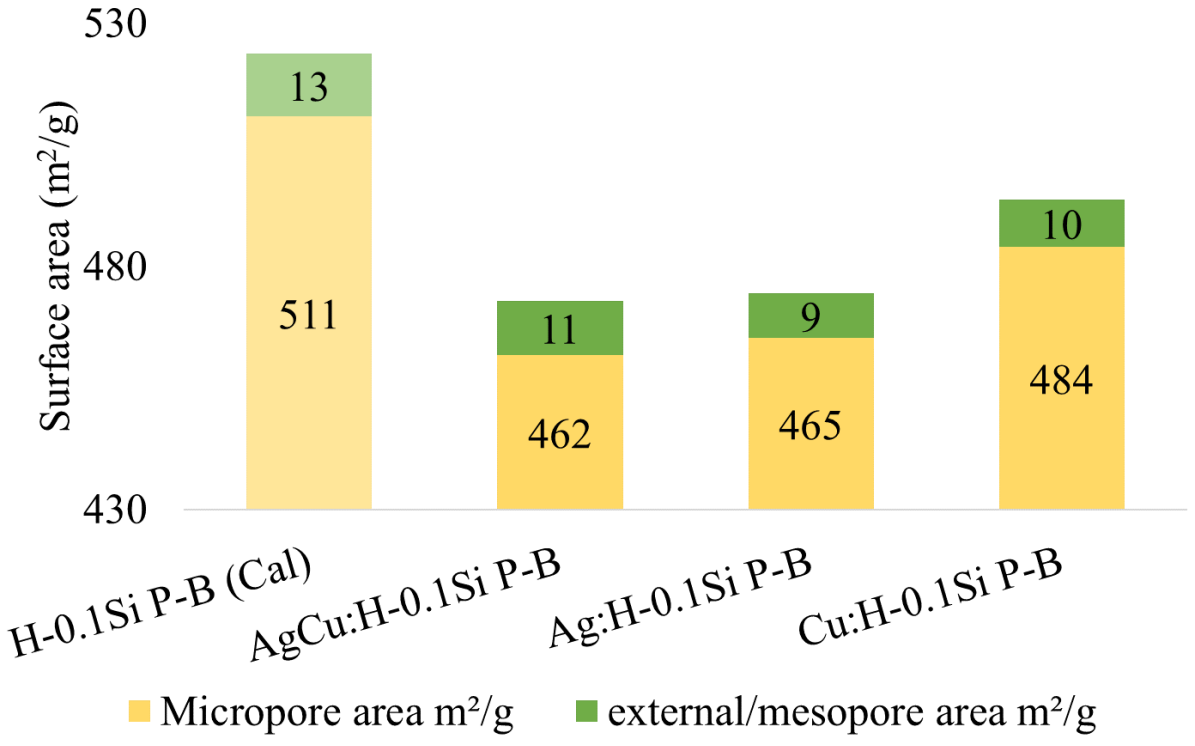

Figure B.20: Pore surface area belonging to the micro- and meso range of H-0.1Si P-B before and after ion exchange.

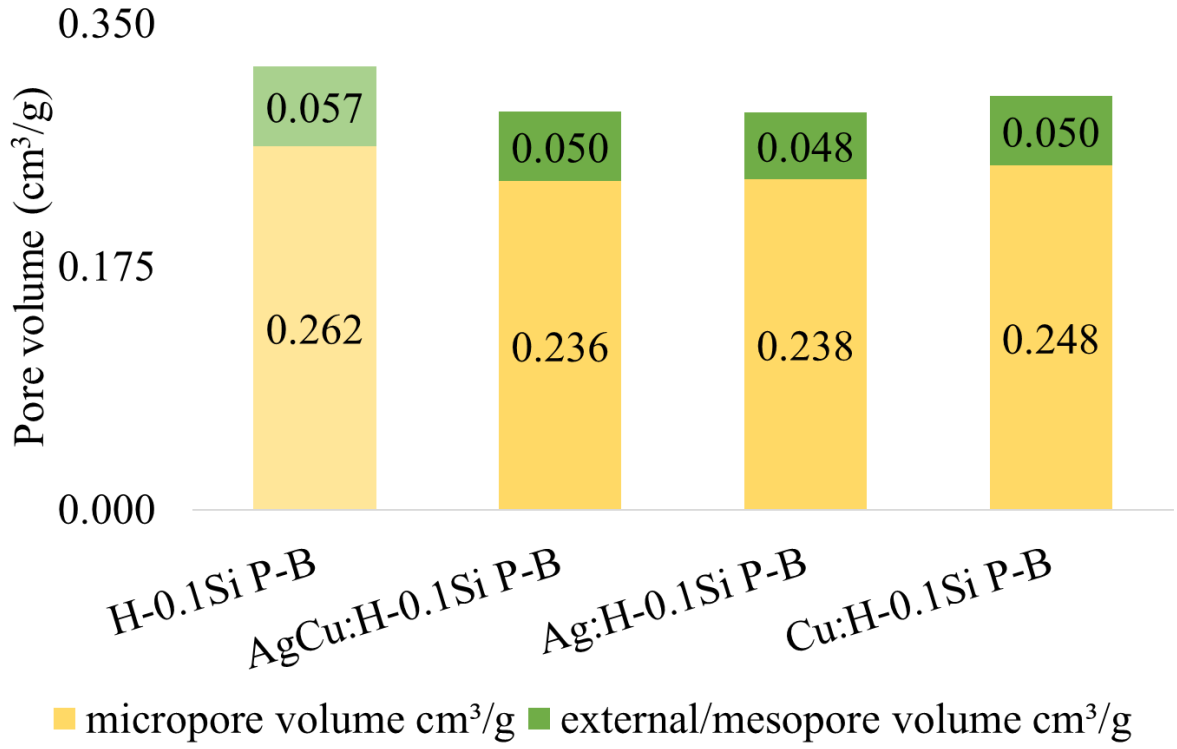

Figure B.21: Pore volume belonging to the micro and meso range of H-0.1Si P-B before and after ion exchange.

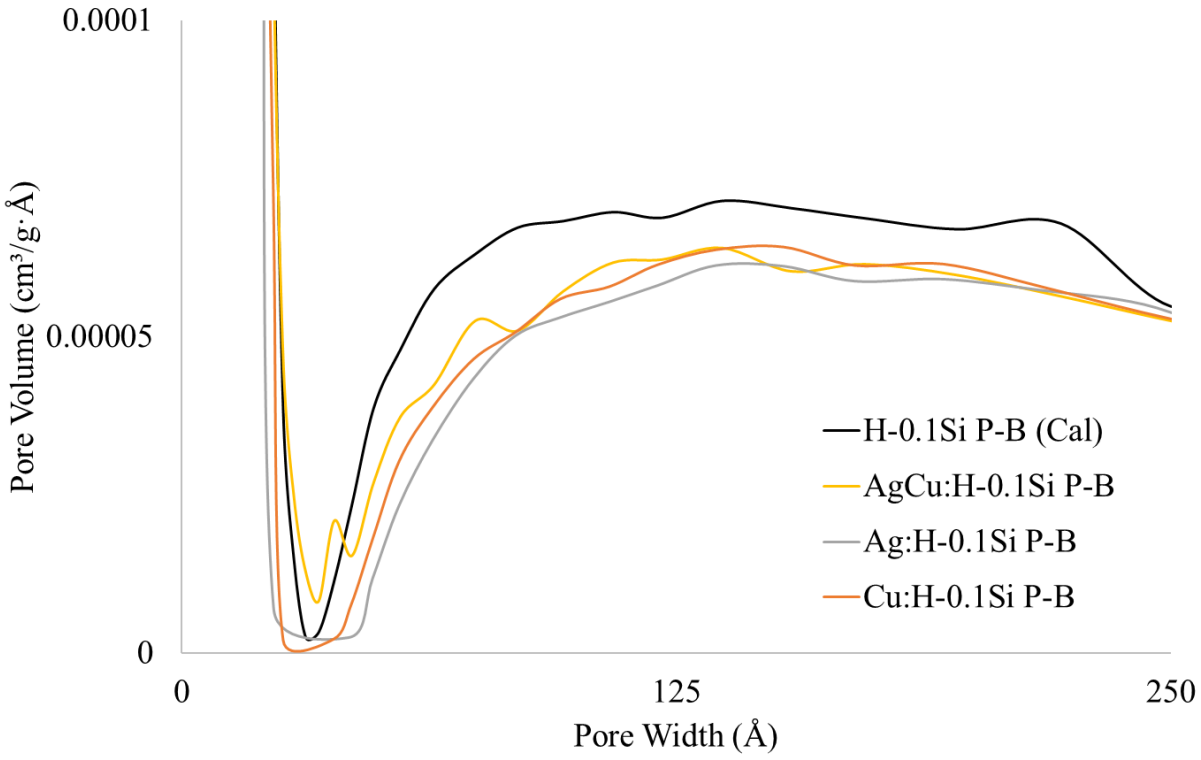

Figure B.22: Change in PSD in the micro and meso range for H-0.1Si P-B before and after ion exchange.

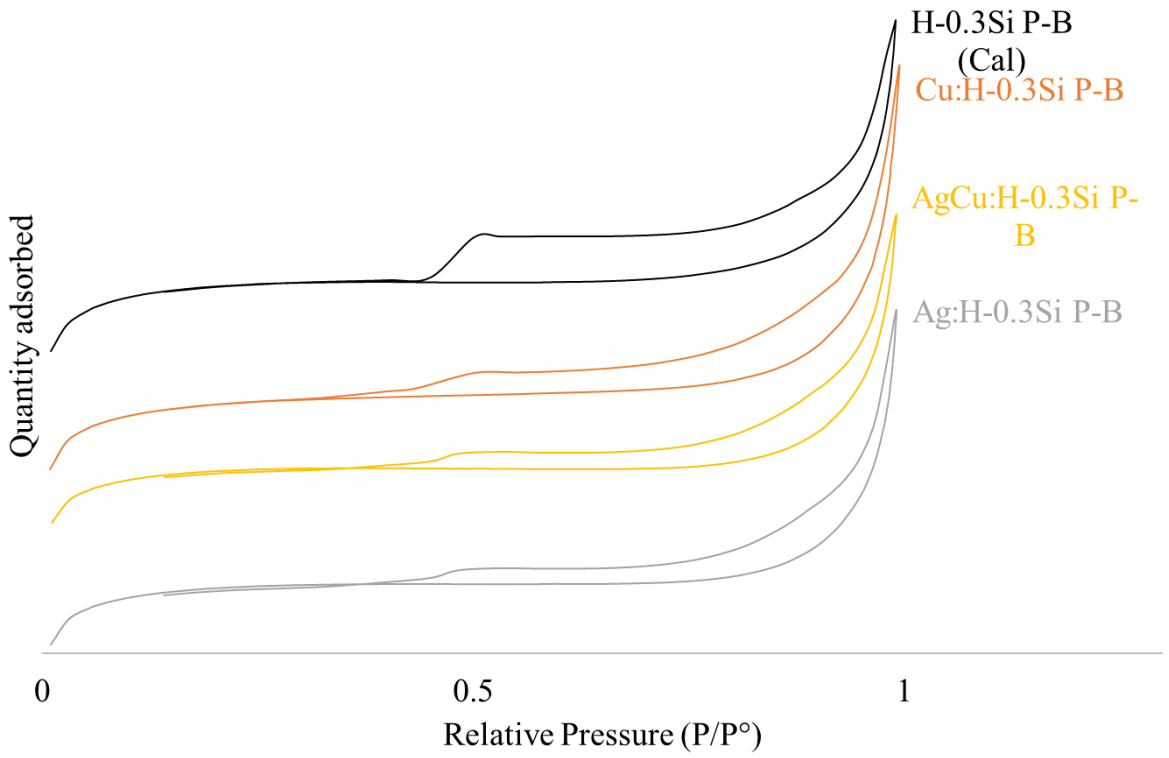

Figure B.23: Change in the isothermal hysteresis before and after ion exchange for H-0.3Si P-B. The curves are stacked.

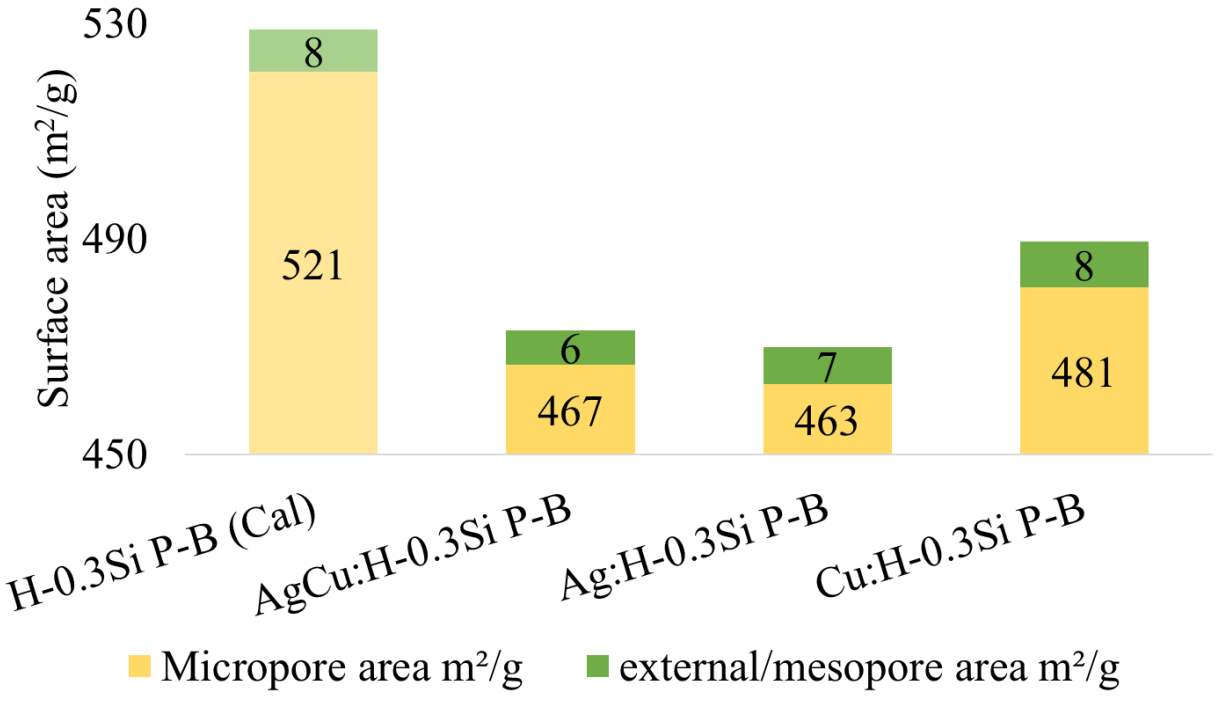

Figure B.24: Pore surface area belonging to the micro- and meso range of H-0.3Si P-B before and after ion exchange.

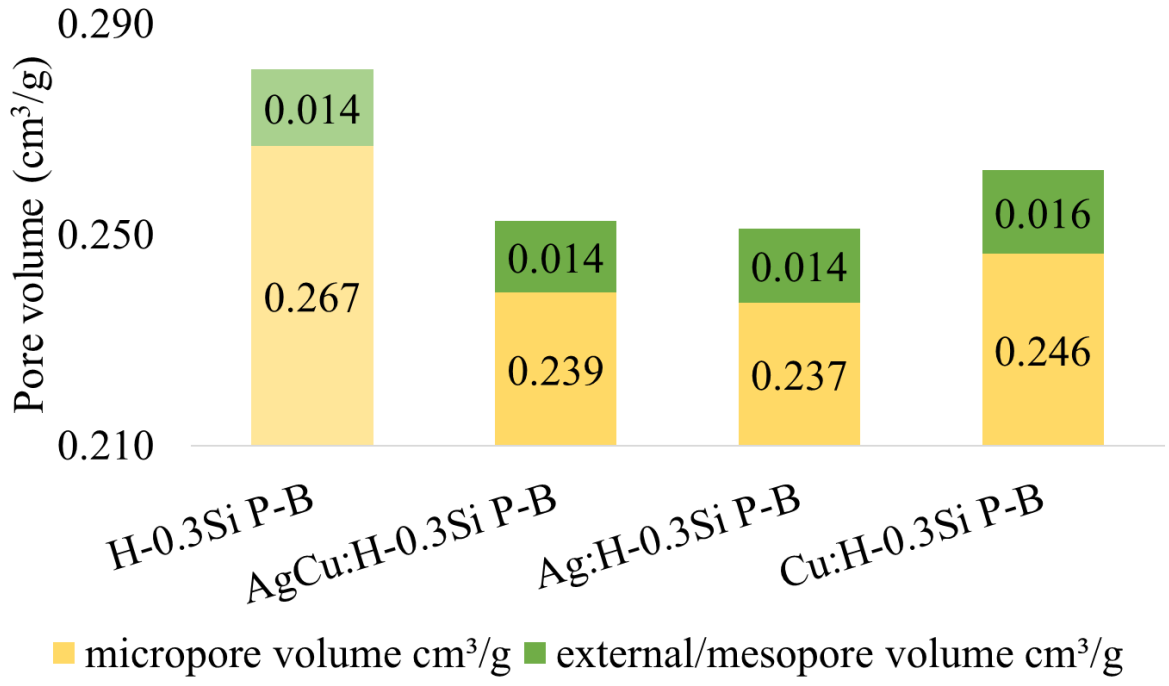

Figure B.25: Pore volume belonging to the micro- and meso range of H-0.3Si P-B before and after ion exchange.

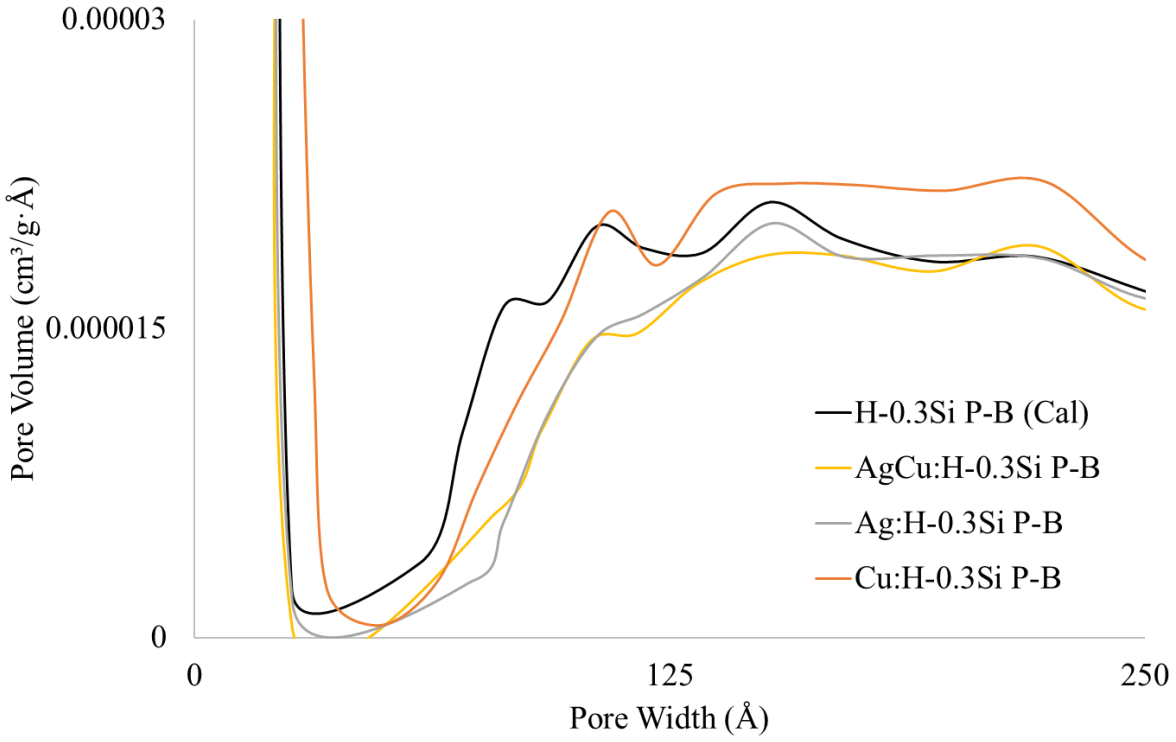

Figure B.26: Change in PSD in the micro and meso range for H-0.3Si P-B before and after ion exchange.

Appendix C: Additional ICP-MS results

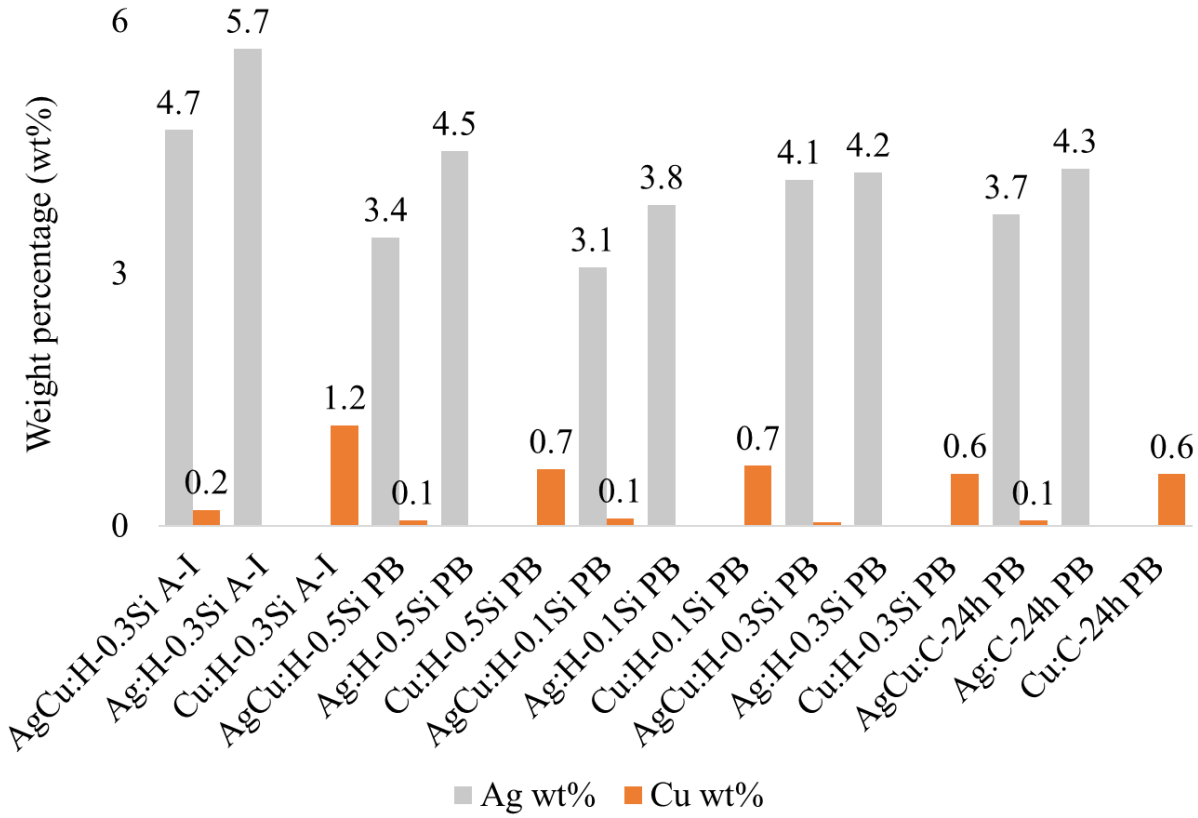

Figure C.1: Metal content present in the remaining phase pure samples not used for NO_x analysis after 1 round of ion exchange.

Appendix D: Additional NO_x analysis results

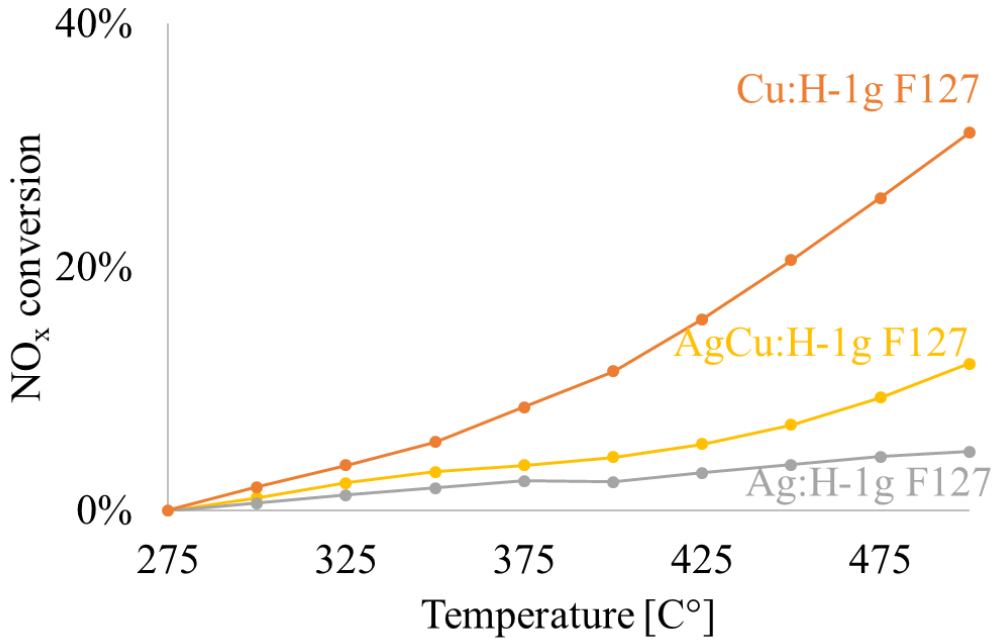

Figure D.1: NO_x conversion results for the H-1g F127 samples ion exchanged 1 round with AgCu, Ag^+ and Cu^{2+}. Metal content (wt%) in each sample: AgCu: (Ag: 3.4 wt%, Cu: 0.1 wt%), Ag: 4.5 wt%, Cu: 0.7 wt%, from Figure C.1.

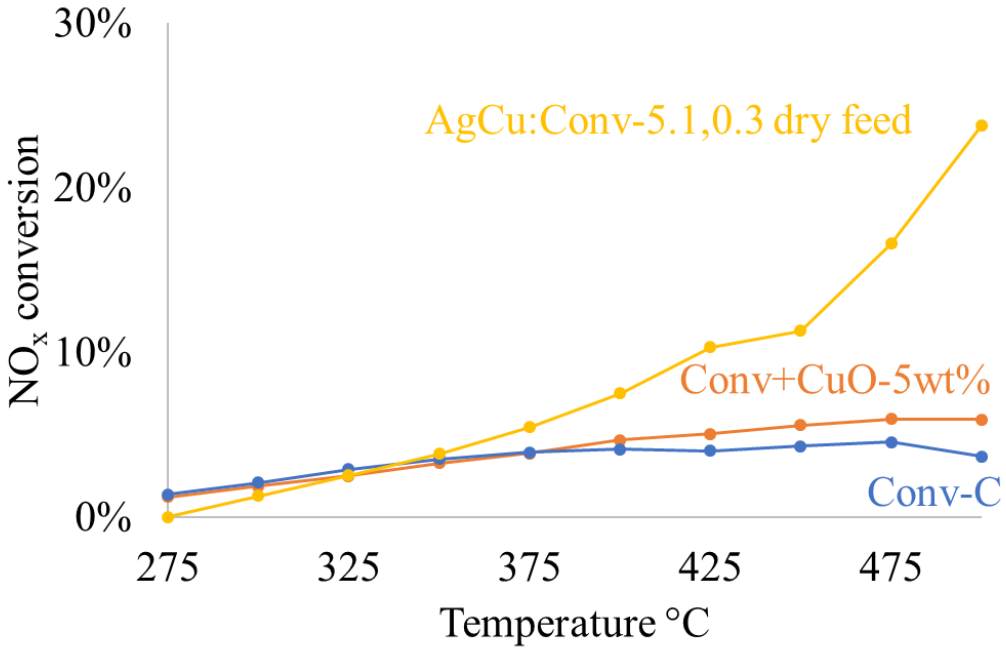

Figure D.2: NO_x conversion results of the plain C-0.5Si A-I calcined (Conv-C) sample without any metal content, and the same sample with 5 wt% copper(II)oxide mechanically mixed through it (Conv+CuO-5wt%). The last result is of AgCu:C-5.1,0.3 run in a dry reactor feed.

Z

Appendix E: Activity diagram of all reactions

Table E-1: Summary of all activity diagrams presented in section 4.3 and for diagrams presented in appendix D. All values are NO_x conversion percentages. Row 16 – 19 are the results obtained with isobutane as hydrocarbon source.

Temperature (°C)	275	300	325	350	375	400	425	450	475	500
Cu:H-1.4	0	3	8	14	21	32	43	51	53	51
Cu:C-1.4	0	4	9	15	25	36	46	50	50	47
Cu:H-0.33	6	11	19	31	41	48	52	54	54	55
Cu:C-0.33	5	12	22	36	46	52	56	57	57	57
[Ag+Cu]:H-1.24,0.33	0	3	7	12	18	24	31	39	48	53
[Ag+Cu]:C-1.13,0.33	3	6	11	16	23	30	40	51	58	60
AgCu:H-4.7,0.2	0	2	4	6	8	11	15	21	27	33
AgCu:C-5.1,0.3	0	2	4	6	9	13	17	23	30	37
AgCu:H-1.04,0.09	2	4	6	8	10	13	16	20	26	34
AgCu:C-0.1,0.01	2	5	7	10	12	16	19	24	31	40
Ag:H-6.7	0	1	2	3	3	4	4	5	6	6
Ag:C-6.4	0	1	1	2	2	2	3	4	5	6
Ag:H-1.24	0	1	1	2	3	3	4	5	6	8
Ag:C-1.13	1	1	2	3	4	5	5	6	8	11
AgCu:C-5.1,0.3	0	0	0	1	1	1	1	1	0	0
Ag:C-6.4	0	0	0	1	1	1	1	1	1	0
Cu:C-1.4	0	0	1	1	1	2	2	2	2	2
AgCu:H-4.7,0.2	0	1	1	2	2	3	3	3	3	3
AgCu:H-1g F127	0	1	2	3	4	4	5	7	9	12
Ag:H-1g F127	0	1	1	2	2	2	3	4	4	5
Cu:H-1g F127	0	2	4	6	9	11	16	21	26	31
Conv-C	1	2	3	4	4	4	4	4	5	4
Conv+CuO-5wt%	1	2	3	3	4	5	5	6	6	6
AgCu:Conv-5.1,0.3 dry feed	0	1	3	4	5	8	10	11	17	24

Appendix F: NO_x conversion calculation

In this appendix a comparison is done. The comparison is between two methods for modelling and returning the correct NO_x ppm bypass value of the system at each temperature interval. One of the methods is the one used by Botne[24], and the other is a logarithmic model that returns the theoretical NO_x ppm bypass value at any given time during the reaction, developed by Phd candidate Guro Sørli and Msc student Sigurd N Botten, both from IKJ. The latter method is for verifying the reliability of the method used by Botne for finding the NO_x bypass value.[24]

F.1 The "weighted bypass" model

The bypass concentration of NO at the beginning and end of each catalysis was different. This was also the case for Botne.[24] As a result, Botne calculated a weighted average for the NO ppm value at each temperature threshold in the temperature programme. The formula for the weighted average was also used in this project and is given in equation F-1 below.[24]

$$NO_{x_{\text{weighted bypass}}} = \left(\frac{500-T}{225}\right) * \text{BypassEnd} + \left(\frac{275-T}{225}\right) * \text{BypassStart} \qquad \text{(F-1)}$$

In the formula, T is one of the 10 temperature values between 500 °C and 275 °C, BypassEnd is the measured NO ppm value at 275 °C and BypassStart is the measured NO ppm value at 500 °C. How heavily either of these two measured NO ppm values are weighted for the NO_x weighted bypass value, is decided by the temperature T.[24] The NO_x conversion in percentage was then determined by the formula in equation F-2:

$$NO_{x_{\text{Conversion}}} = \frac{NO_{x_{\text{weighted bypass}}} - NO_{x_{\text{reactor}}}}{NO_{x_{\text{weighted bypass}}}} * 100\% \qquad \text{(F-2)}$$

The NO_x reactor value was the NO_x ppm value given in the last minute the furnace stays at one of the temperatures T. Like this, the NO_x value had 20 minutes at each temperature to stabilize its NO_x ppm value, providing the most correct value. As such, the NO_x concentration data over time was related to the temperature data over time, providing the NO_x concentration at each temperature T and hence the activity of the sample at each temperature T. Botne regarded samples with NO_x conversion values greater than or equal to 30 % as active samples at the temperatures for which the values counted, and the same was done in this project.[24]

F.2 Repetition of the logarithmic model for the bypass value

The registered bypass start value is always higher than the bypass end value. In order to model the change in the bypass value through the course of the temperature program, a blank test was done, by running the gas feed through an empty reactor tube. Through the duration of the temperature program, the gas feed is turned on the bypass tube 12 times including the bypass start value. The bypass value is for each time registered after stabilization. The CLD 62 Eco-Physics Chemiluminescence NO/NO_x registers the NO_x ppm value every third second. Figure F.1 presents the resulting bypass values at each bypass interval for the duration of the temperature program as blue points. By linear regression in excel, a logarithmic trendline gave a proper fit to the points where its formula is given in the top right of Figure F.1.

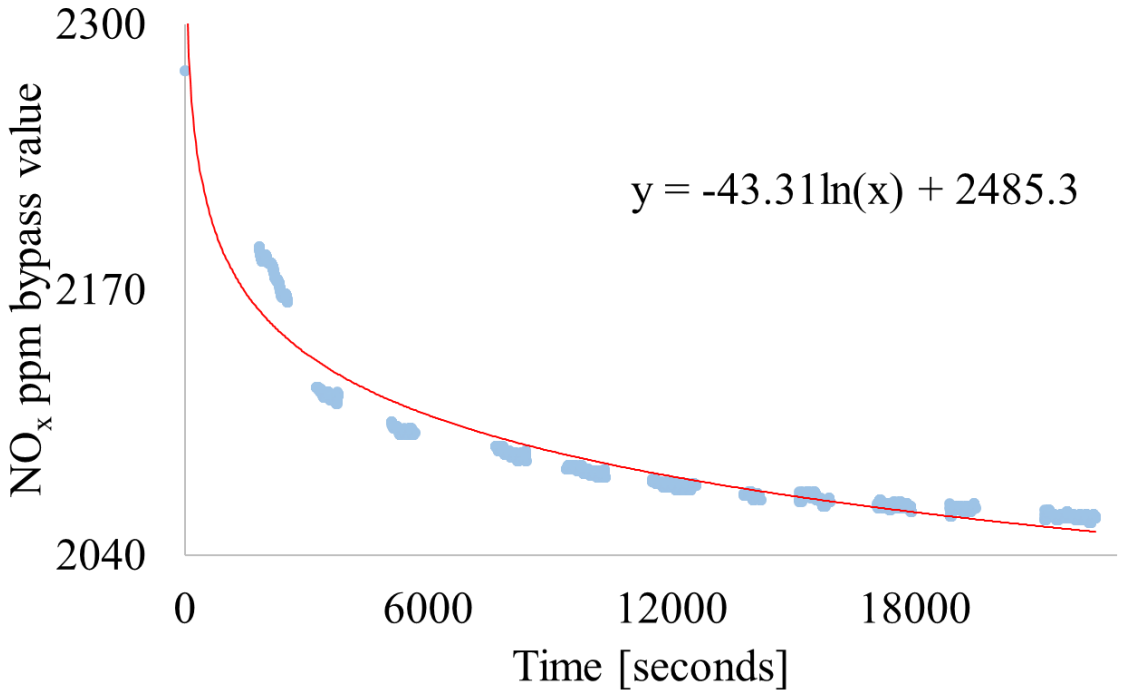

Figure F.1: Logarithmic trendline for the registered, stabilized NO_x ppm values through the temperature program.

From here, the stabilized bypass value was registered for ca. 10 minutes at 500 °C, 400 °C and 275 °C, for the tests run on the samples themselves presented in section 4.3. For 4 samples, these values were used to model the similar logarithmic functions for the bypass values belonging to each of these samples, by linear regression as described for the blank sample.

From here, the NO_x conversion values of these 4 samples were calculated by using both methods and are presented and compared in Table F-1 below. From the results, it is apparent that there

is good overlap between the obtained NO_x conversion values from using either method. As such, the "weighted bypass" method has good reliability and has been used for calculating all NO_x conversion values in this thesis, presented in section 4.3 and Appendix D: Additional NO_x conversion results, Figure D.1 and D.2.

Table F-1: Comparison of obtained NO_x conversion values for using the "weighted bypass" model, or the logarithmic model marked with [ln] in the sample column, for all temperatures (°C). All values are given in percentage (%).

Samples	275	300	325	350	375	400	425	450	475	500
Cu:C-0.33	5	12	22	36	46	52	56	57	57	57
Cu:C-0.33 [ln]	6	11	22	35	45	51	55	56	56	56
Ag:H-1.24	0	1	1	2	3	3	4	5	6	8
Ag:H-1.24 [ln]	0	0	0	0	1	1	1	2	3	5
AgCu:C-0.1,0.01	2	5	7	10	12	16	19	24	31	40
AgCu:C-0.1,0.01 [ln]	2	4	6	8	11	13	17	22	28	37
[Ag+Cu]:H-1.24,0.33	0	3	7	12	18	24	31	39	48	53
[Ag+Cu]:H-1.24,0.33 [ln]	3	5	8	12	16	22	28	37	45	51

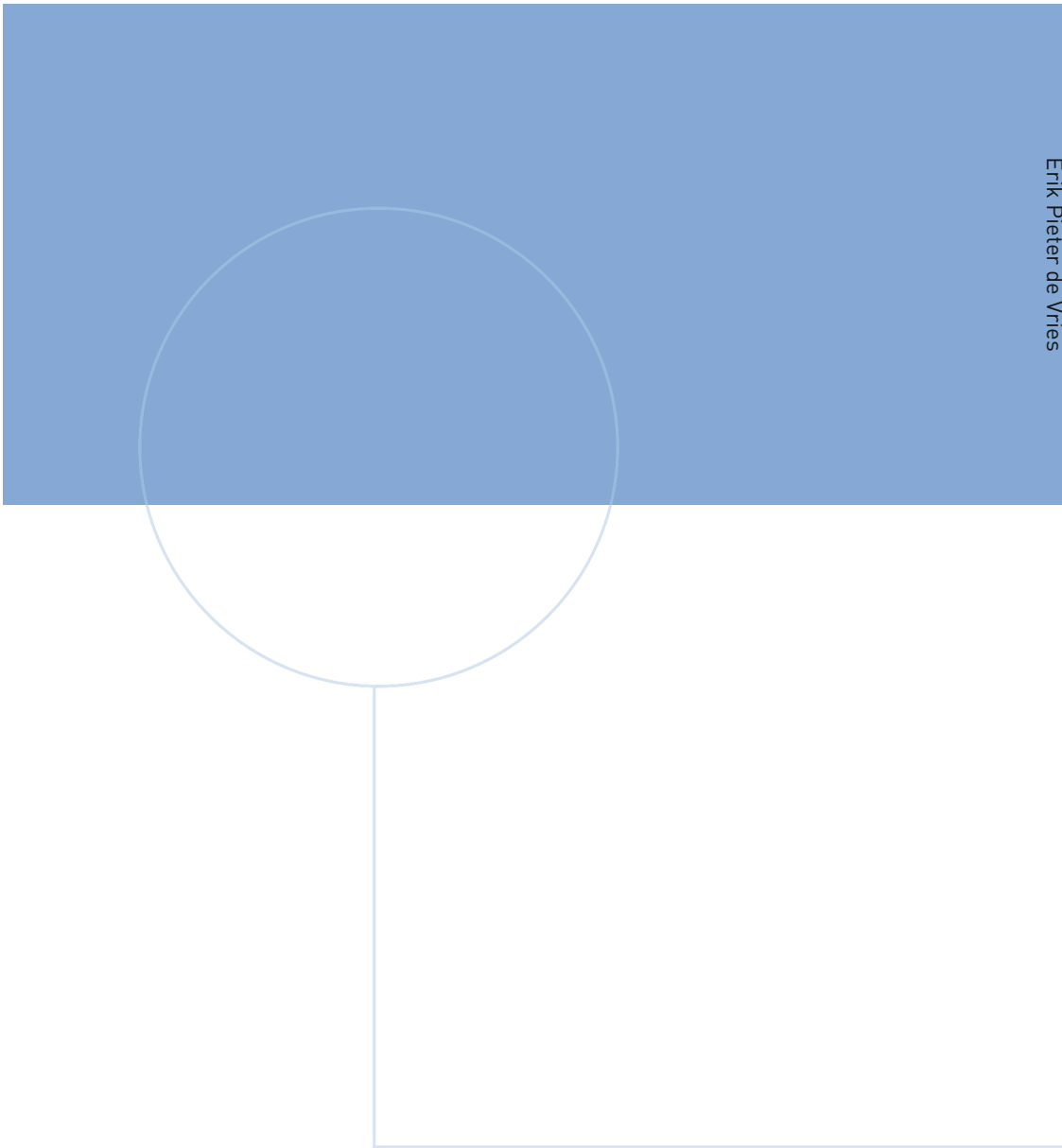

Erik Pieter de Vries

NTNU
Norwegian University of
Science and Technology